ANNUAL REPORT

FORUM FOR

EXPLORATION AND DEVELOPMENT

GEOPHYSICS

EDUCATION AND RESEARCH

AT THE

UNIVERSITY OF TEXAS AT AUSTIN

May 31, 2013
Annual Report for EDGER Year 13 (June 1, 2012 - May 31, 2013)

Robert H. Tatham, Principal Investigator
Mrinal K. Sen, Co-Principal Investigator
Kyle T. Spikes, Co-Principal Investigator
Margo C. Grace, Forum Coordinator

Department of Geological Sciences
The John A. and Katherine G. Jackson
School of Geosciences
The University of Texas at Austin
Austin, Texas 78712

UT-AUSTIN
EDGER
FORUM

Nurturing Education & Research
for Tomorrow's Technology Needs
at the Edge of Knowlege

Table of Contents

Executive Summary

We report the results of EDGER Year Twelve (June 1, 2012 - May 31, 2013) of the UT-Austin Forum for Exploration and Development Geophysics Education and Research (EDGER Forum). The industry supported 'Geophysical Forum' is part of an aggressive Exploration Geophysics Program within the Department of Geological Sciences, Jackson School of Geosciences, The University of Texas at Austin. The forum focuses on both the education and research aspects of developing tomorrow's leaders in the application of geophysical technologies to petroleum exploration and development activities. Furthermore, results of research undertaken by students and faculty are available for application by members of the Forum and eventually widely disseminated by publication in professional journals. In addition, databases supporting research and planning operations are being developed and maintained.

Benefits and Results of Participation

Research (Faculty & Student)

Benefits:

- ✓ Direct access to faculty, post-doc and MS & PhD student research results
- ✓ Establish directions for faculty, student, and post-doc research
- ✓ Develop cooperative projects between sponsors and EDGER researchers

Results for year Thirteen

- ✓ 3 PhD and 1 MS degrees completed during EDGER Year 13
- ✓ Over 35 publications in 2012-2013
- ✓ Six active and two evolving cooperative research projects with sponsors

Proposed for year Fourteen:

- ✓ Continue established research directions
- ✓ Continue development of Focus Areas of Application
- ✓ Expand cooperative projects with sponsors, especially in applications for shale resources

Forum sponsored activities

Benefits:

- ✓ Participation in multi-disciplinary workshops and symposia
- ✓ Exclusive access to broader elements of objective-oriented interpretative database
- ✓ Direction in proposing pertinent industry workshops

Results for year Thirteen

- ✓ ***Annual Research Symposium: Seismic Characterization of Shales, Mudrocks and Tight Formations***
- ✓ Development of eight cooperative research projects
- ✓ Objective-oriented database of case histories maintained and updated

Proposed for year Fourteen:

- ✓ Continue annual technical symposium and interactive industry workshops
- ✓ Continue development of content and expand usage of the MC data base
- ✓ Conduct user workshops in Focus Areas of Application

Educational Activities

Benefits

- ✓ Direct access to students
- ✓ Graduates employable by industry
- ✓ Cooperative student research projects

Results for year Thirteen

- ✓ Seven new graduate students (6 new MS and 1 new PhD student)
- ✓ 18 graduate students enrolled with focus on Exploration Geophysics in the Dept. of Geological Sciences
- ✓ 30 undergraduate students in Option II-Geophysics as of January 2013

Proposed for year Fourteen

- ✓ Three new grad students (PhD) accepted for graduate program in exploration geophysics in Fall 2013
- ✓ Recruit new graduate students for Fall 2014 admission
- ✓ Continue sponsors' direct and ongoing participation in setting educational and research directions

Although organized and administered similar to research consortia at various institutions, the EDGER Forum includes a focus on education as well as research. In this sense, accountability emphasizes both educational and specific research goals that create educational opportunities for the students. Opportunities, however, exist to conduct focused research projects, funded separately from the Forum.

With significant emphasis on education, participating companies may desire to consider funding at a broader level than an individual business unit that would benefit from the research effort. To that end, business units and corporate recruiting would benefit from increased availability of top-flight graduates in exploration geophysics.

The broad research direction of the EDGER Forum has historically been focused on imaging, inversion, interpretation and analysis of multi-component seismic reflection data. This encompasses AVO analysis of P-P and mode-converted P-SV data to estimate rock properties. These topics now include wave-propagation modeling, rock physics, and quantitative interpretation. A new effort includes microseismic data into the list of topics. A number of these topics have evolved into Focus Areas of Application. Our sponsors have embraced the current focus area on unconventional resources (including microseismic), and we intend to expand this subject through active cooperative projects.

Forum activities also include workshops focused on implementation of emerging technology within the industry. The UT-EDGER Forum is in a unique position to coordinate this type of activity between various aspects of the industry and the academic community. Members propose many of these workshops. On May 29th, 2013, the most recent workshop focused on identifying issues, problems, and limitations of microseismic data.

Integrated Research and Education

Overview

As part of the evolution of both industry and academic perspectives, more and more emphasis is focused on integrated research topics and education subjects. Accordingly, the need to link geophysics, geology, and engineering arises in many discussions within industry, within academia, and between the two.

Integrated Research

For integrated research to progress, a graduate student in geophysics must be able to speak at a minimum two "languages". Geophysics is the first, and the other typically is engineering or geology. The needs of an engineer differ from those of a geophysicist. Therefore, the student must be able to converse fluently with engineers to understand their needs. To complete the task, the student must convey to an engineer the capabilities and limitations of a particular geophysical technique or dataset. In addition, it is necessary to describe how to convert a geophysical data volume to an engineering data volume along with the associated uncertainty. If the second language is intended to be geology, the same rules hold, but the focal point becomes relating geophysical attributes to geological interpretations. This communication can be possible only if the researcher understands the scale, resolution, and underlying physical principles for all the data types and techniques. Moreover, the researcher must be aware that working in multiple disciplines requires expert knowledge in both fields to disseminate the results to a broader audience.

Integrated Education

Geoscience research to link multiple disciplines must begin with education along similar guidelines. At the school and university level, this responsibility belongs to the teaching faculty who must convey the importance of their primary specialties while simultaneously emphasizing the pertinence of a secondary area of expertise. This is a challenge in a structured course setting, but it can be done with the proper planning and support of several individuals. Ultimately, the goal is not to teach two or more topics but to teach the students the practice of working with individuals from any discipline that a particular research project might require.

Relevance to the EDGER Forum

Developing integrative research and education subjects falls within the goals of the Jackson School of Geosciences. Moreover, the petroleum industry appears to continually need new experts who are capable of leaving the confines of their own areas of expertise and reaching across barriers that are either artificial or in place for non-scientific reasons. The EDGER Forum is a location to provide the type of environment conducive to the integrated approaches necessary for cutting-edge geoscience research.

Student projects addressing problems defined with EDGER members and utilizing industry data have been quite successful in integrating geological and geophysical concepts for students and have significantly enhanced their education experiences.

Industry Relations

State of the Petroleum Industry

In the past few decades, the petroleum industry has experienced a gap in the age distribution of geoscientists in general and geophysicists in particular. This dearth of younger geophysicists is well known throughout industry, academic, geo-society, and government organizations.

A paper in the June 2012 issue of The Leading Edge points out that the majority of current earth scientists in the U.S. will retire within 15 years (30-40% are currently retirement-eligible) and about 40-50% of the current workforce has fewer than five years of industry experience. Obviously, this dramatic gap in the experience of geoscientists is a reminder that a critical need exists to educate new geoscientists at all levels. This impending need is already turning into reality. Across the United States, the older, more experienced generation is beginning to retire at an accelerating rate in all areas of employment common for geophysicists.

The EDGER Forum addresses the shorter term issues by supporting graduate education and research and supplying graduates in the time frame of 2–6 years and conducting research relevant to industry needs. Essential undergraduate education is focused on much longer time frames. For example, GeoFORCE is an experiential outreach program that prepares Texas high school students to become part of the geosciences workforce. The 'Earth is Calling' program has also been designed to engage students and raise awareness of career opportunities to college-bound high school students. Lastly, the NSF EarthCube Initiative aims to bring young students into the different areas of Earth Sciences as part of the U.S. government's goal of maintaining national prominence in STEM (Science, Technology, Engineering, Math) fields.

These initiatives underscore the critical need for trained geophysicists as more experienced personnel in the industry retire. The cyclic nature of commodity prices, which drive the business cycles of the industry, are often difficult to align with research and new graduates entering the industry. Future personnel accordingly needs must be addressed in the context of timeliness and need-based situations.

Industry Recruiting at UT-Austin

UT-Austin is on the recruiting list for most companies hiring geoscientists. Last year, over 40 companies representing a broad cross-section of the industry visited the department. One consistent question from the recruiters is, "Where are the geophysicists?" The Exploration Geophysics Program and the EDGER Forum in particular are designed to address this industry need. Members should note that although this industry recruiting effort is very much appreciated at UT, the direct access to students within EDGER is also a very valuable recruiting tool.

UT Geology Foundation Support

Beyond general endowments dedicated to Exploration Geophysics, the UT Geology Foundation permanently endows a major full-year graduate student fellowship since 1999 as part of the original 'Exploration Geophysics Initiative.'

This endowed fellowship, part of the proposed industry support of the Forum, is competitive with any other in the country and ensures the highest quality applicants are attracted to the Exploration Geophysics program at UT. Endowments totaling several million dollars, focused on aspects of Exploration Geophysics, reside in the Geology Foundation.

The overall support of the Exploration Geophysics program provides a sound base and offers significant leverage for the funding provided by the EDGER Forum.

**Fellowships and Awards
(UT and Industry)**

The 'Exploration Geophysics Fellowship' endowed by an anonymous donor, was created in order to encourage strong applicant to enter the Exploration Geophysics program. This fellowship is offered to an entering student each year.

Recipients of The 'Exploration Geophysics Fellowship' award are:

TBD	2013
Sarah Coyle	2012
Russell Carter	2011
Alexander Lamb	2010
Corey Joy	2009
Robert Brown	2008
Travis Richards	2007
Anisa Perez	2006
William Burnett	2005
Christopher Sine	2004
Sharon Goehring	2003
Patricia Yu	2002
Matthew Morris	2001
Jason Gumble	2000

Industry and philanthropic donors have also provided a number of other significant fellowships to graduate students since the start of the EDGER Forum over a decade ago, including: BP, Chevron, ConocoPhillips, Marathon, GXT, Hess, Saudi Aramco, Shell, Banks Memorial, Teagle, John Buck, Gale White, Fullbright, Ewing / Wurtzel, Cullinan, Questar and the Barrow Graduate Fellowship.

Industry Input and Direction

To ensure that the 'Exploration Geophysics Initiative' meets the needs of the Petroleum Industry, the Department of Geological Sciences hosted a symposium to assess the needs and expectations of potential industry participants. This 'Year Zero' symposium, held in December 1999, became the first in a series of technical symposia that form a central component of the EDGER Forum. Annual Symposia since that date have enhanced and greatly extended the research conducted by the EDGER Forum.

Overall, the Exploration Geophysics Program must maintain enough breadth to ensure proper education while simultaneously providing enough focus on meaningful research programs for graduate students, post-doctoral candidates and supporting faculty. This focused research will provide useful technology for application by sponsors.

Industry Internships

Summer 2000   **Year 1**
Fernando Cerda   Phillips

Summer 2001   **Year 2**
Jason Stine   BP
Jason Gumble   BP

Summer 2002   **Year 3**
Matt Morris   BP
Jason Stine   Conoco
Eric Lyons   Marathon

Summer of 2003   **Year 4**
Jason Gumble   WesternGeco
Patricia Yu   Marathon
Eric Lyons   Marathon
Eric Swanson   Dawson

Summer of 2004   **Year 5**
Eric Lyons   Marathon
Sharon Goehring   ConocoPhillips

Summer of 2005   **Year 6**
Chandan Kumar   BP
Samarjit Chakraborty   BP
Kimberly Kumar   BP
Matt McDonald   Shell
Christopher Sine   Anadarko
Jason Stephens   ConocoPhillips
Russell Young   ConocoPhillips

Summer of 2006   **Year 7**
Engin Alkan   Dawson
Reeshidev Bansal   Chevron
Will Burnett   BP
Samarjit Chakraborty   ExxonMobil
Thomas Lovitz   Marathon
Emily Pangborn   ConocoPhillips
Chris Sine   Chevron
Sanjay Sood   GXT

Summer of 2007   **Year 8**
Tiangcong Hong   BP
Chaoshun Hu   Chevron
Anisa Perez   ConocoPhillips
Samik Sil   GW Systems
Daniel Smith   ExxonMobil
Sanjay Sood   GXT

Summer 2008   **Year 9**
Adam Alan (Undergrad)   Kerogen Res
Vladimir Baskardin   GXT
William Burnett   ExxonMobil
Chunlei Chu   BP
Jeffrey Kao   Nexen
Travis Richards   Swift Energy
Alireza Shahin   Swift Energy
Samik Sil   Chevron
Sandy Suhardja   GXT
Fang Ye   Kerogen Res

Summer 2009   **Year 10**
Vladimir Baskardin   Chevron
Rob Brown   Marathon
William Burnett   ExxonMobil
Diego Valentin   Anadarko
Yang Wang   ExxonMobil
Fang Ye   BP

Summer 2010   **Year 11**
Terence Campbell   Hess
Na Shan   ION-GXT
Vladimir Bashkardin   Total E&P
Yu Xia   ION-GXT
Yi Tao   ConocoPhillips
Corey Joy   BP
William Burnett   ConocoPhillips

Summer 2011   **Year 12**
Alexander Lamb   Devon
Xiaolei Song   Chevron
Terence Campbell   ConocoPhillips
Yi Tao   ConocoPhillips
Yang Xue   Shell

Summer 2012   **Year 13**
Qi Ren   Chevron
Russell Carter   ConocoPhillips
Meijuan Jiang   Shell
Yang Xue   Shell
Kumar Das   NGRI, India

Summer 2013   **Year 13**
Qi Ren   Chevron
Russell Carter   ConocoPhillips
Meijuan Jiang   Shell
Lauren Becker   Marathon
Sarah Coyle   Exxonmobil
Jacqui Maleski   ConocoPhillips
Patrick Gustie   Halliburton/Landmark
Makoto Sadahiro   Halliburton/Landmark

Students in Exploration Geophysics

We are often asked how many students are in Geological Sciences at UT Austin and how many are on international visas. For the current term, the count is as follows:

	US	Visa	Total
Undergrad	273	18	291
Graduate	184	98	282
Total	457	116	573

For the upcoming academic year, including graduate students who have accepted offers, the current graduate student body with an interest in exploration geophysics is 27 for Fall 2013. We have also had a number of visiting graduate students from international universities, including one current visiting scholar who will be working with Dr. Tatham and Dr. Sen for the next year.

Academic Year	New Students Entered	MS	PhD Graduated
1996-99	3	1	0
2000/01	1	0	0
2001/02	2	1	1
2002/03	5	1	1
2003/04	3	1	0
2004/05	7	2	1
2005/06	8	3	2
2006/07	6	9	1
2007/08	2	5	2
2008/09	7	3	2
2009/10	7	4	3
2010/11	8	3	2
2011/12	3	2	1
2012/13	7	2	3
2013/14	3	TBD	TBD

We target on average six new graduate student admissions for each academic year. With the support provided by recent new sponsors, we exceeded this goal in Fall 2012. With increased industry support through the EDGER Forum, we are able to support more graduate students, with the potential of 8–10 graduates each year.

Many qualified students applied for graduate admission for Fall 2013. We are pleased that three new students accepted our offer of admission. With the present pool of applicants and current students, our industry partners have a great opportunity for recruitment from a strong and relatively large class graduating in the next year. This is a continuation of graduating MS students with a thesis, a practice highly encouraged by the industry.

There are presently 30 undergraduate students who have declared Geophysics (Option II) as their major as of the start of the 2013. This number has increased in the last several years, and we hope to see that trend continue. Our undergraduate geophysics curriculum is recognized as one of the few in the US with an emphasis in exploration geophysics, and we intend to maintain that effort. A significant number of these undergraduates are well qualified to attend graduate school in geophysics at UT-Austin as well as other notable institutions.

Positions for post-doctoral researchers are currently being considered to enhance further the research profile of the EDGER forum. We can envision one to two post-docs over the next several years to complement the MS and PhD student work and to provide additional links between student and faculty research topics of interest. At present, we are looking for potential candidates although no formal offers have been made at the time of writing.

Current Graduate Students
with a focus in Exploration Geophysics

31 May 2013

Student	Advisor	Degree Obj.	Research Comments
Elliot Dahl BS Physics, Royal Institute of Technology, Stockholm '12	Spikes Ent. Fall '13	Incoming PhD	*TBD*
Debanjan Datta BS Geophysics, Indian School of Mines University, '12	Sen Ent. Fall '13	Incoming PhD	*TBD*
Sarah Coyle BS Geosciences / eophysics University of Texas at Austin '12	Spikes Ent. Fall '12	Currently Enrolled MS Student	*Inversion of seismic data with and without rock typing*
Lauren Becker BS Geosciences / Geophysics University of Texas at Austin '12	Spikes Ent. Fall '12	Currently Enrolled MS Student	*Finite-element simulations of fracture networks*
Patrick Gustie BA Earth & Planetary Sci /Geophysics University of California, Berkley '12	Tatham Ent. Fall '12	Currently Enrolled MS Student	*Identifying seismic attributes to estimate vertical transverse isotropy*
Jacqueline Maleski BS Geology University of Georgia '12	Tatham Ent. Fall '12	Currently Enrolled MS Student	*Application of Alford rotation to multi offset data*
Makoto Sadahiro BA Computer Science University of Texas at Austin '02	Tatham/Stoffa Ent. Fall '12	Currently Enrolled MS Student	*Processing algorithm development (Reverse Time Migration)*
Han Liu BS Geololgy & Geophysics Missouri Univ of Sci. & Tech '12	Spikes Ent. Fall '12	Currently Enrolled PhD Student	*Numerical modeling of complex pore shapes*
Karl Stetten Visiting Student from Norway Norwegian University of Science and Technology (NTNU)	Tatham/Stoffa Ent. Fall '12	Visiting MS Student	*Time-lapse seismic characterization of reservoir production*

Current Graduate Students
with a focus in Exploration Geophysics

31 May 2013

Student	Advisor	Degree Obj.	Research Comments
Qi Ren BS Applied Physics University of Sci/ & Tech (USTC) '10	Spikes/Sen Ent. Spring '12	Currently Enrolled PhD Student	*Seismogram synthesis,imaging, and rock physics*
Jiao Xue MS Geophy Prospe & Inf. Tech China Univ of Geosciences, China '08	Tatham/Sen Ent. Fall '11	Visiting PhD (Candidate) Student	*Applications of AVO anisotropy to estimate fracture characteristics in subsurface reservoirs*
Zeyu Zhao BS Geophysics University of Petroleum, China '11	Sen Ent. Fall' 11	Currently Enrolled PhD Student	*Sub-basalt imaging with wide-aperture seismic data*
Yawen He BS Geophysics University of Petroleum, China '11	Hongliu Zeng/Sen Ent. Fall '11	Currently Enrolled PhD Student	*Reservoir monitoring of seismic facies*
Sharif Munjur Morshed MS Petroleum Geology Geophysics University of Dhaka '10	Tatham Ent. Fall '10	Currently Enrolled MS Student	*Seismic anisotropy of the Marcellus Shale*
Meijuan Jiang MS Statistics University of Illinois '10	Spikes Ent. Fall '10	Currently Enrolled PhD (Candidate) Student	*Rock physics and seismic characterization of the Haynesville Shale*
Russell W. Carter BS Geology Colgate University '07	Spikes Ent. Fall '10	Currently Enrolled PhD (Candidate) Student	*Reservoir chracterization for carbon sequestration*
Yang Xue MS Geophysics University of Stuttgart '07	Sen Ent. Fall '09	Currently Enrolled PhD (Candidate) Student	*Bayesian inversion of land multi-component data*
Terence A. Campbell MS Geology UT Austin '07	Tatham/Sen Ent. Fall '09	Currently Enrolled PhD (Candidate) Student	*Corrections for distortion polarization in reflected shearwave for isotrapic and anisotropic medium*

UT Alumni Graduates
of the EDGER Forum Program

August 2000 - May 2013

Student	Advisor	Current Position	Research Comments
Mohammed Alhussain MS Geophysics Curtain University '08	Sen Ent. Fall '08	PhD May 2013 Saudi Aramco (Dharan)	*Removing anisotropic overburden effect for reliable reservoir fractures characterization*
Kumar Sundaram Das MS Applied Geophysics Indian Institute of Technology '08	Sen Ent. Fall '10	MS May 2013 ? (?)	*Gas hydrates saturation estimation in Krishna-Godava*
Yi Tao MS Geophysics Chinese Academy of Science '08	Sen Ent. Fall '08	PhD Dec 2012 ConocoPhillips (Houston)	*Seismic inferometry and inversion*
Engin Alkan MS Geophysics UT Austin '07	Hardage Ent. Fall '10	PhD Dec 2012 Shell (Houston)	*Elastic seismic stratigraphy*
Alexander P. Lamb BS Physics / Info. & Comp. Sci. University of California, Irvine '08	Tatham Ent. Fall '10	MS May 2012 Devon (Oklahoma City)	*Characterization of Woodford Shale*
Kwon Taek Oh BS Chemical Engineering Chungnam National University '94	Spikes Ent. Fall '10	MS May 2012 Korea Gas Corporation	*Pore shape estimation from seismic velocity in the Haynesville Shale*
Corey Joy BS Engineering University of Texas at Austin '09	Sen Ent. Fall '06	MS August 2011 BP (Houston)	*Effective medium modeling of carbon sequestered reservoirs*
Son Phan BS Geophysics University of Tulsa, Oklahoma '09	Sen Ent. Fall '09	MS August 2011 BiendongPOC (Vietnam)	*Uncertainty in reservoir parameter estimation*
Alireza Shahin MS Petroleum Expl. & Engineering Univesity of Tehran '02	Stoffa/Tatham Ent. Spring '06	PhD May 2011 BP (Houston)	*Time lapse seismic response to production*
William Burnett MS Geophysics UT-Austin '07	Fomel/Stoffa Ent. Fall '05	PhD May 2011 ExxonMobil (Houston)	*Multi-azimuth velocity analysis using velocy-independent seismic imaging*
Tao Liu BS Geophysics/Economics Beijing University '06	Sen Ent. Fall '09	PhD (Candidate) Visiting PhD Student (2009-2010)	*Hybrid finite difference-finite element of seismic wave propagation*
Diego Valentin BS. Geology Univ. Nat Colombia. '08	Tatham Ent. Fall '08	MS Aug 2010 Gran Tierra Energy (Bogotá)	*Bossier Reservoir characterization with multicomponent VSP and surface seismic data*
Fang (Fiona) Ye ME Geophysics. Ocean Univ. (PRC) '03	Tatham Ent. Spring '08	MS May 2010 BP (Houston)	*Fracture estimation in the Bakken Shale from 3C-3D data.*
Jeffrey Chung-Chen Kao BS Geophysics University of Texas at Austin '05	Tatham Ent. Fall '01/Fall '07	MS December 2009 Nexen (Dallas)	*Deep water GOM - pore pressure estimation using P-SV Waves from multicomponent seismic in Atlantis Field*
Chunlei Chu ME Geophysics Ocean Univ of China '03	Stoffa Ent. Fall '05	PhD Dec. 2009 ConocoPhillips (Houston)	*Application of variable grid finite differences to seismic imaging and modeling*
Samik Sil MS Geophysics Univ of Alaska '06	Sen Ent. Fall '06	PhD May 2009 ConocoPhillips (Houston)	*Two-way travel time analysis for seismic reservoir characterization*

Student	Advisor	Current Position	Research Comments
Jonas De Dio De Basabe Delgad MS Computational & Applied Math UT-Austin '07	Sen / Wheeler Ent. Fall '07	PhD May 2009 Ctr for Sci Research & Higher Education (Ensenada, Baja CA)	*Numerical simulation of elastic wave propagation* *UTIG Fellow*
Anisa Perez BS Geophysics Rice Univ '06	Tatham / Ferguson-C.Mosher Ent. Fall '06	MS May 2009 ConocoPhillips (Houston)	*Azimuthal analysis of hybrid gatherers*
Chaoshun Hu MS Petroleum Engineering 2005 UT-Austin '05	Stoffa / McIntosh Ent. Fall '03 & '05	PhD Dec 2008 Chevron (San Ramon)	*OBS and MCS data analysis for TAIGER Project, offshore Japan*
Daniel Ryan Smith BS Geophysics Univ of Utah '06	Sen Ent. Fall '06	MS Aug. 2008 Hess (Houston)	*Seismic trace regularization and datuming*
Tiancong Hong BS Geoscience Penn State '04	Sen Ent. Fall '04	PhD Aug. 2008 ExxonMobil (Houston)	*MCMC algorithm, integrated 4D seismic res. char. and uncertainty analysis in a Bayesian framework*
Ali Al-Jadhar MS Geophysics King Fahd University of Petroleum	Stoffa Ent. Fall '06	MS Aug 2008 SaudiAramco (Dharan)	*Prestack modeling of carbonate reservoirs* *Saudi Aramco Scholar*
Abdulaziz Al-Muhadib BS Geology Univ of Tulsa	Sen / Tatham Ent. Fall '06	MS Aug. 2008 PhD Student MIT	*Post-stack inversion for porosity estimation of carbonate reservoirs* *Saudi Aramco Scholar*
Sanjay Sood MS Geophysics Punjab Univ India	Sen / van Avendonk Ent. Fall '04	MS Dec 2007 ConocoPhillips (Houston)	*Estimation of Q from seismic refractions data*
Patricia Yu BS EPS, Berkeley '02	Ferguson Ent. Fall '02	MS Dec 2007 Shell (Houston)	*Amplitude preservation in processing and imaging of seismic data*
Emily Marleah Pangborn BS Industrial Engineering Cornell University '05	Bangs / Tatham Ent. Fall '05	MS Dec 2007 Chevron (Houston)	*Thrust fault from 3D seismic: Nankai Subduction Zone, Japan.*
Nedra Bonal BS Geophysics New Mexico Tech. '00	Wilson Ent. Sp. '02	PhD Dec 2007 Sandia Nat Lb (Albuquerque)	*Fracture characterization: studies of seismic anisotropy and trace imaging with GPR.*
Engin Alkan BS Geological Eng. Ankara University	Hardage Ent. Fall '05	MS Aug 2007 PhD Student (UT-Austin)	*Acquisition design of 3D multicomponent surveys on land* *Turkish Nat. Oil Co. Scholar*
William Burnett BS Geophysical Eng. Colo. Sch. Mines 05	Ferguson Ent. Fall '05	MS May 07/ PhD 2011 ExxonMobil (Houston)	*A general transform for reversible seismic data processing* *Exploration Geophysics Fellowship ('05)*
Reeshidev Bansal MS Geophyics Virginia Tech . '03	Sen Ent. Fall '03	PhD May 2007 ExxonMobil (Houston)	*Seismic characterization of naturally fractured reservoirs*
Samarjit Chakraborty MS, Geophysics Indian Inst of Technology (IIT) '02	Ferguson Ent. Fall '02	MS May 2007 BP (Houston)	*An int. geologic model of the Valhall Oil Field for simulation of fluid flow and seismic response*
Christopher Robert Sine BS Geology Northern Arizona University '04	Grand Ent. Fall '04	MS May 2007 Occidental (Bakersfield)	*Tomographic velocity interpretation of the Upper Mantle, Colo Plateau*
Kevin Alan Bain BS, Physics UT-Austin, '01	Tatham Ent. Fall '01 & '05	MS May 2007 UT-PhD Stud. (Physics)	*Sensitivity of AVA reflectivity to fluid hydrocarbon properties in Porous Media*
Gregory Russell Young BS Geology & Math Centenary College of Louisiana '04	Sen Ent. Fall '04	MS May 2007 ExxonMobil (Houston)	*Effective porosity estimation from 3D seismic: Marco Polo Fld.* *ConocoPhillips Fellowship ('04)*

Student	Advisor	Current Position	Research Comments
Kathryn Teresa Young BS Electrical Engineering Universtiy of West Indies '04	Tatham Ent. Fall '04	MS Dec. 2006 BP (Houston)	*False 'bright spots' and discriminating gas and brine using AVO Fullbright Scholar*
Matt McDonald BS Physics Brigham Young University '03	Tatham / Gulick (UTIG) Ent. Fall '04	MS Dec. 2006 Shell (Houston)	*The Chicxulub impact crater and oblique impact*
Eric Lyons BS Geophysics UT-Austin '02	Tatham Ent. Fall '98 & '02	MS Dec. 2006 ConocoPhillips (Houston)	*Polarization distortion of shear waves in isotropic media*
Jason Gumble BS Geophysics Colorado School of Mines '00	Tatham Ent. Fall '00	PhD Dec. 2006 Cimarex (Denver)	*Anisotropic analysis of 3C data for OBC and comparison to 9C. / ACS-PRF Funded Dissertation / Expl.Geophysics Fellowship ('00)*
Chandan Kumar BS Geophysics Indian Inst. of Technology (IIT) '02	Ferguson / Sen Ent. Fall '02	PhD Dec. 2006 BP (Houston)	*Parameter inversion for seismic anisotropy*
Kimberly Melissa Kumar BS Geophysics, University of Western Ontario '04	Ferguson Ent. Fall '04	MS May 2006 BP (Trinidad)	*Pore pressure prediction offshore Trinidad. BP Scholar*
Patricia Montoya BS, Geophysical Eng. Simon Bolivar, '95	Fisher/ Tatham Ent. Fall '00	MS '03/PhD May '06 ExxonMobil (Houston)	*Salt tectonics and Sequence-stratigraphic history of mini-basins near the Sigsbee Escarpment, Gulf of Mexico*
Sharon Goehring BS Geology & Computer Science Elizabeth City State University '02	Tatham Ent. Fall '03	MS Dec 2005 ConocoPhillips (Houston)	*Seismic AVO response to variations in SS reservoir properties Exploration Geophysics Fellowship ('03)*
Dhananjay Kumar MS Exploration Geophysics Indian Inst. of Technology (IIT) '00	Sen/ Stoffa Ent. Fall '01	PhD May 2005 Chevron (Houston)	*Analysis of multicomponent seismic data from the Hydrate Ridge, offshore Oregon*
Carmen Teresa Gomez BS Geophysical Engineering Simon Bolivar University '02	Tatham Ent. Sp. '03	MS May 2005 PhD Stanford Shell (Houston)	*Sensitivity of P-P, SH-SH and P-SV seismic reflectivity to partial gas saturation.*
Jason Andrew Stine BS, Physics Franklin & Marshall '00	Tatham Ent. Fall '00	MS May 2004 Teaching in (Baltimore)	*Sensitivity of AVO reflectivity to fluid properties in porous media*
Matthew Graham Morris BS, Geophysics U. Missouri (Rolla,) '01	Tatham Ent. Fall '01	MS Dec. 2003 Anadarko (Houston)	*Analysis on P-P and P-SV AVO response*
Chengshu Wang MS, Geology Chinese Acad. of Geol. Sci. '87	Sen/ Tatham Ent. Fall '96	PhD Aug 2003 Returned to China (PRC)	*Inversion of P-P and P-SV data, separate density effect gas hydrates. (BSR)*
Chau Ao Undergraduate NTNU (Tjåland Norway)	Tatham Ent. Fall '00	MS-NTNU May 2001 Statoil (Stavanger)	*Compare Vp/Vs interpretation between SH-SH and P-SV data.*
Fernando Cerda BS Geophysical Engineering Colorado School of Mines '96	Fisher/ Tatham Ent. Fall 'Sp. '99	MS Dec 2001 WesternGeco (Houston)	*Teal South project: Compare Vp/Vs from shear (P-SV) and interpretation with AVO results.*
Helena Zirczy BS Geophysical Engineering Simon Bolivar University '95	Tatham Ent Fall'98	MS Aug 2000 Shell (Houston)	*Multicomponent Seismic Interpretation of the Second Wind Field, Kiowa and Cheyenne Counties, Colorado*

Faculty, Facilities and Infrastructure

Faculty and Facilities

Eight individuals work on geophysical research within the Department of Geological Sciences. Specific to the EDGER Forum are Dr. Robert H. Tatham, Dr. Mrinal Sen who also has a 50% appointment at UTIG, and Dr. Kyle T. Spikes who is full time in the department. Dr. Paul L. Stoffa also advises graduate students with a focus in Exploration Geophysics, as does Dr. Clark Wilson in the Dept. of Geological Sciences. Dr. Sergey Fomel, with the Bureau of Economic Geology, is a professor of the faculty of the Department of Geological Sciences, and he also advises students focused on Exploration Geophysics. Sean Gulick and Nathan Bangs focus on marine geophysics for crustal scale and exploration topics.

Facilities

Much of the infrastructure for Exploration Geophysics is housed in the L. Decker Dawson Exploration Geophysics Training Center in the Jackson Geological Sciences building. Students and also have offices at the UT Institute for Geophysics on the J. J. Pickle Research Campus.

3D Seismic Interpretation Lab

The 3D seismic interpretation laboratory is routinely refreshed with upgraded software and hardware made possible through endowments specifically formed to provide students with state-of-the art computational abilities. Regularly scheduled courses utilize this facility. In addition graduate students in soft rock and petroleum geology also conduct thesis research on 3D data sets in the lab. Thus, the laboratory supports a wide cross- section of students and provides a place for interaction among students in many petroleum-related disciplines. We anticipate that over time additional students from all the above areas will enroll in courses involving the lab. We believe a synergistic interaction between these students will evolve as a result.

Geophysical Analysis and Interpretation Capability

In addition to the 3D seismic interpretation lab, computationally intensive work- stations have been installed for use by graduate students in geosciences, particularly for the Exploration Geophysics program. These workstations, tied to the high-speed storage area network shared by the 3D seismic interpretation lab, have computational and storage capability to accommodate pre-stack multicomponent 3D datasets. In the last year, this laboratory was completely refurnished with new Linux and PC workstations capable of handling most industry-scale datasets. Additional workstations will be added as more graduate students join the Exploration Geophysics program.

Software and Data Support Manager

We have added an Applications Software Manager to the staff to support the wide variety of programs available to the Forum as well as to maintain the seismic data sets available. Initial funding came from a grant made by the UT Geology Foundation to the EDGER Forum to provide leveraged financial support to initiate this infrastructure. The position is now partially funded by the EDGER Forum. Presently the Exploration Geophysics Program and UTIG also support the position. This capability is crucial to the success of cooperative projects applying industry data, especially with MS students who are here for only a few semesters.

3D Seismic data sets available

Several 3D seismic data sets are available for research and educational use. Some of these data sets include nearly complete subsurface log and production data. These data sets are an important industry contribution to the education and research programs in the Jackson School of Geosciences.

<u>Chevron:</u>
>> East Texas data set
>> Louisiana State lease 30 and OCS 310, including complete log data. (Used for both education and research purposes).
>> Garden Island Bay Field
>> Port Neches Field

<u>ExxonMobil:</u>
>> South Timbalier area, offshore Louisiana.

<u>BP:</u>
>> East Texas data set
>> Gulf of Mexico 3-D data set
>> Forties Field (North Sea)
>> Atlantis 3D-4C ocean-bottom (Nodes) data set.

<u>PGS:</u>
>> West Africa, 3-D data set.
>> West Cameron 3D 4C volume.
>> Gulf of Mexico 4C pre-stack vol.

<u>WesternGeco:</u>
>> Matagorda Bay 3D shoot

<u>ERCH:</u>
>> Teal South 3D-4C time lapse data set The EDGER Forum is the repository for the Teal South Data.

<u>Colo. School of Mines:</u>
>> Use of the Joffre 3D-9C data set.
>> Weyburn Field P-SV Data set.

<u>Anadarko</u>
>> Maro Polo 3D pre-stack data
>> Donotello 3D-3C and VSP data set

<u>Kerogen Resouces</u>
>> Bakken Shale Dipole Logs & 3C Surface Seismic data

<u>CGGVeritas</u>
>> 3C-3D data set - Anadarko Basin

Data Base of Multicomponent Seismic Interpretation Successes

The entry point of the data base is located within the EDGER website at the following URL:
http://edger.jsg.utexas.edu/edger_db

One of the common problems in implementing new technology is the education of the end user on actually applying the technology. This is particularly true for multicomponent seismic methods. Often technology developers understand the new application, but fail to fully educate the implementers on its ultimate implementation. This database is an attempt to assist in the technology transfer and education process.

The database allows potential users to search for actual examples of applications that are similar to their own problem. To this end, the database is organized with the intention of addressing specific exploration or development objectives and problems by providing a value-added database that catalogues successful shear wave interpretations from published sources. Work on this project has been conducted over many summers with undergraduate work-study students and graduate students supported by the Forum. To date, about 500 published real-data examples are included—with about a thousand examples anticipated. These examples are organized to allow searches based on survey objectives, and thus are 'problem oriented.' At the present time, the data base is being maintained, but new entries are at a reduced level.

The purpose of the database is to provide EDGER Forum members, and UT-Austin students and researchers, exclusive access to details of results from existing work in the interpretation and analysis of multicomponent seismic data. This has proven invaluable in planning multicomponent seismic projects, particularly 4C marine projects.

Guest ID's and passwords are available for temporary examination of the entire database by prospective members.

Objective oriented browser:

The primary user access to the database is through the Objective oriented browser. The entries can be sorted on a number of variables, including: project name, exploration or development objective (including two sub-objectives), the interpretative method applied and the actual multicomponent data type. The browser includes a comprehensive project listing in the left frame, and an interpretive summary on a selected entry in the right frame.

The objective oriented browser has recently been completely updated and additional content for the database is continuously being added.

An example of an entry is illustrated on the previous page. By default, the Project List is sorted by Project Name, however users can also click the heading to toggle the order. To sort on more than one field, the user holds down the Shift key on the keyboard and clicks on the appropriate heading to filter the results. There is also an internal search engine for filtering the data.

UT-AUSTIN
EDGER
FORUM

Keyword ▼ | | Search

← Return to EDGER Site | Objective View | Project View | Logout | Home | Contact

PROJECT NAME	OBJECTIVE	SUB-OBJECTIVE 1
Valhall 21	Anisotropy	Structural Imaging
Alba 16	Improved Structural Imaging	
Bluebell-Altamont 1	Fracture	Parameter Estimation
West Cameron 5	Gas Cloud Imaging	
Teal South 9	Acquisition Evaluation	
Sorrento 2a	Lithology	Discrimination
North Slope 1	Gas Hydrate	
Pinedale 1	Anisotropy	Fracturing
Midland Basin 5	Shear wave Reflectivity	
Oseberg 5	Lithology	Discrimination
Green Canyon 2	Gas Hydrate	
Guillemot 1	Processing	
Mahogany 3	Improved Structural Imaging	
Nowa Deba 1	HCI	
Teal South 3	Fracture	Parameter Estimation
Vinton Dome 1	Improved Structural Imaging	
Eastern Goldfields 1	Improved Structural Imaging	
Bluebell-Altamont 4	Fracture	Parameter Estimation
Ekofisk 1	Anisotropy	Structural Imaging
Rulison 2	Lithology	Estimation
Cave West 1a	Lithology	Discrimination

PROJECT VIEWER — Print Project 🖨

PROJECT NAME		OBJECTIVE	
Bluebell-Altamont 1		**Fracture**	
AREA	TARGET AGE	SUB-OBJECTIVE 1	SUB-OBJECTIVE 2
NE Utah	Tertiary	Parameter Estimation	
TYPE OF INTERPERATION	AREA COMMENT	COUNTRY	METHOD NAME
S1/S2	Uinta Basin	USA	

FIG. 8. S1 polarized (N30W) reflection data and S2 polarized (N60E) at well D on Line 2. Amplitude dimming on S2 relative to S1 is observed in the T/GR-Z interval that is characterized by very low S-wave anisotropy. The Z-TN1 interval is characterized by high S-wave anisotropy, but no significant differences in amplitude between S1 and S2 are noted.

RESOLUTION		DATA TYPE	DATE OF ACQUISITION
Interval		3D-9C	1994
INTERVAL THICKNESS	OBJECTIVE THICKNESS	SOURCE	RECEIVER
80ft		Vibroseis	3C
REF TITLE		REF JOURNAL/PAGES	
P-wave and S-wave azimuthal anisotropy at a naturally fracturred gas reservoir, Bluebell-		Geophysics, Vol. 64. No. 4: p. 1312-1328	

Technical Symposia and Workshops

One of the major benefits of EDGER Forum membership is, perhaps, the "community activities" coordinated and sponsored by the Forum. Overall, symposia and workshops have provided a platform for the exchange of ideas between industry members (contractors, equipment manufacturers and producers), academics and the graduate students. Further, the objective-oriented multicomponent seismic database is now being used by the entire technical community. Discussions of research directions by industry and academic participants have led to student and faculty research projects. The UT-Austin EDGER Forum is in an excellent position to facilitate communication between the various elements and encourage participation of the overall exploration and development geophysics community.

User Workshops

The objective of these workshops is to share common problems with seismic data sets, consider what kind of problems can be addressed and define focus areas among explorers, producers, contractors and manufacturers. The first workshop, held in 2003 at the Shell facility in Houston, focused on 'Current Problems in Acquisition, Processing and Interpretation of Multicomponent Seismic Data'. Based upon this, a second follow-up workshop, hosted by ConocoPhillips in Houston, was held a year later. Follow-up to these workshops was realized in an EAGE/SEG sponsored workshop in Pau, France, in 2005.

Industry Workshop on Shales

On December 16th, 2009, BP hosted a well-attended one day informal workshop on Shale Plays and Unconventional Resources – one of the "Focus Areas of Application" for the EDGER Forum. The Objective of this Workshop was to share insights into geophysical observations of shales, in particular which geophysical properties of shales may differentiate between good and poor producing wells. Using borehole data, several students are currently investigating the seismic response to variation in physical properties of Bakken, Bossier, Marcellus and Woodford Shales.

Industry Workshop on Microseismic data

As a foray into issues with microseismic data issues and limitations, BP hosted a one-day workshop on microseismic data for the EDGER forum sponsors on the 29 May, 2013. A total of 45 attendees from 10 sponsor companies attended. The emphasis was to understand the current practices for locating microseismic events along with uncertainty and associated geomechanical approaches to understand the fracturing process and the implications for production curves. We anticipate that this valuable information will help provide additional and pertinent future research projects for faculty, post-docs, and students.

Short Courses

As part of technology sharing between the UT-Austin and sponsors of the EDGER Forum, faculty involved with the Forum are available for short courses. This type of contact between university and industry personnel enhances the purpose and effectiveness to the Forum.

Technical Symposia

As an element of the annual meeting, typically held on the UT-Austin campus in late February, the EDGER Forum hosts the annual technical symposium. Current Focus Areas of Application include unconventional resources, but the range of topics has expanded considerably in the last several years. These symposia allow for an exchange of new ideas and provide direction for student research projects that either ongoing or just beginning. The students find this interaction most useful in terms of providing a real-world application for their research topics.

With the enthusiastic industry interest, the annual events held on campus in 2013 were very well attended, and there has been a significant increase in sponsorship.

YEAR 13
The Annual Meeting & Technical Symposium took place March 4–6, 2013.

Description
Problems in unconventional resources and resource plays are often considered completion issues until drillers find that one well comes in with a two-month payout and the next well, in a nearby location, results in a two-year payout. The question is, can geophysics help us focus on the two-month payout wells?
Several students are working on cooperative projects with industry sponsors addressing seismic issues with unconventional resources. Current projects in progress are outlined on page 28, and further opportunities are available with students interested in projects in other areas, including the Barnett, Marcellus, and Woodford Shales.

The meeting and symposium continued the cooperative discussion on direct research in shale plays providing possibilities for future working groups among sponsors and the EDGER Forum. Further, developments in application methods crucial for geophysical evolution of shales were presented.

A summary of all past symposia of the EDGER Forum is given on the following three pages.

Technical Symposia sponsored by the EDGER Forum

	Year 13	Year 12	Year 11	Year 10
Academic Year	2012-2013 March 4-March 6, 2013	2011-2012 Feb 27-Feb 28, 2012	2010-2011 Feb 28-Mar 1, 2011	2009-2010 Feb 22-23, 2010
Topic	**Seismic Characterization of Shales, Mudrocks and Tight Formations**	**Seismic Characterization of Producing Shales**	**Seismic Characterization of Resource Shales**	**Unconventional Resources and Shale Production**
Description	The concentration of research activities on the characterization of shales, mudrocks and tight formations continues. With a focus on rock physics, seismic characterization and inversion for rock and fluid properties and numerical simulation of seismic wave propagation, potential applications address and expand on our understanding of the subsurface properties and production of hydrocarbons from shales, mudrocks and tight formations. This includes subsurface properties that may be observable in surface seismic data.	In characterizing shale resources using surface seismic data, we must concentrate on the physical properties that affect seismic wave propagation. This requires an understanding of how seismically observable quantities, such as the Vp/Vs of HTI & VTI anisotropy may be related to properties, such as fracturing of kerogen content, and which quantities may effect production. Presentations and discussions include development of these relations.	Problems in shale plays are often considered completion issues until drillers find that one well came in with a two month payout and an adjacent well results in a two-year payout. Can Seismic help? Presentations examined seismic responses to variations in shale characteristics extrapolated from bore-hole log data, which was then used to test sensitivity to shale characteristics & direct analysis of shale from surface seismic.	Addressed Unconventional Resources in terms of Focus Areas of Application, including Shale Production, Time Lapse Seismic and Reservoir Characterization and Numerical Simulation and Modeling. Many of the subject numerical discussions focused on applications to shale resource plays and anisotropy effects.
Comment	A Keynote presentation "The Next Evolution: where are we in Unconventional Geophysical Applications" by Eric von Lunen of Nexen, sets the context for presentations and discussion on seismic characterization of shales, mudrocks and tight formations.	Faculty and student research utilizes borehole data, such as dipole logs and core information, to predict the seismic response to reservoir properties. This should lead to the evolution of analysis schemes to predict actual reservoir properties.	Several Students are working on cooperative projects addressing seismic issues with shale plays as very little is known about shales, and seismic response being tested from synthesis based on actual bore-hold data.	Problems are being addressed in the context of Focused Areas of Application, and this problem-orientation has been very well received by sponsors.

Technical Symposia sponsored by the EDGER Forum

UT-AUSTIN EDGER FORUM	Year 9	Year 8	Year 7	Year 6	Year 5
Academic Year	2008-2009 Feb 23-24, 2009	2007-2008 Feb 25-26, 2008	2006-2007 Feb 26-27, 2007	2005-2006 Feb 27-28, 2006	2004-2005 Feb 14-15, 2005
Topic	**How canGeophysics enhance our Search for and Definition of Unconventional Resources?**	**Seismic Methods to Address Unconventional Resources**	**Applications of P- and S-wave Methods to Land Assets**	**Seismic Response to Pore Fluid Properties**	**Seismic Response to Partial Gas Saturation**
Description	Presentations defined issues and problems associated with successful development & exploitation of Unconventional Resources. Problems discussed included silica content and Anisotropy that may be observed seismically, and the relation to productivity.	Presentations addressed issues commonly associated with exploration for and development of unconventional producing assets on land, including: tight gas sands, shale and fractured reservoirs, including the Bossier, Barnett and Bakken plays.	Presentations addressed issues commonly associated with exploration for and development of producing assets on land. This included defining strategies using the information in both P and S wave data. Interactive discussion sessions led to potential cooperative research projects.	Fluid properties considered included partial gas saturation, saturation distribution (homogenous or 'patchy'), over-pressure, and fluid viscosity. Both P- and S- wave observations will be required to fully address partial saturation issues. The program was dominated by student research results.	The program addressed defining Partial Gas Saturation and its impact on applying seismic methods to exploration and production problems. Many of the results evolved from research directions defined in the AVO symposium of 2003.
Comment	Larry Lunardi, VP Geophysics at Chesapeake Energy, presented the keynote address. Focus Areas of Application enthusiastically supported by sponsors.	Several cooperative projects with industry sponsors and UT for MS research projects.	Direct industry participation led to potential joint industry – student thesis research topics.	As with the 2005 symposium, significant student research results evolved from 2003 AVO symposium directions.	Included significant student research results evolving from directions defined in the 2003 symposium.

Technical Symposia sponsored by the EDGER Forum

	Year 4	Year 3	Year 2	Year 1	Year Zero
Academic Year	2003-2004 Feb 16-17, 2004	2002-2003 Jan 27-28, 2003	2001-2002 Jan 28-29, 2002	2000-2001 Dec 11-12, 2000	1999-2000 Dec 6-7, 1999
Topic	**Successful Applications of Multicomponent Seismic Data**	**Seismic Attributes: Deterministic and Statistical**	**New Directions in AVO**	**Geophysical Assessment of Fault and Stratagraphic Hydrocarbon Seals**	**The Future of Exploration Geophysics: Meeting the needs of Industry and Academia**
Description	Included Industry participation from a wide variety of organizations. The program focused on documented successful application of Multicomponent seismic methods in actual exploration settings.	The two-day workshop was split into one day addressing statistical attributes and one day focused on deterministic attributes. Considerable discussion centered on comparisons between the two classes of attributes, as well as specific methods of each.	Included large industry participation with a focus on New Directions in AVO applications (as opposed to improvements in AVO applications.) Provided clear research directions for student projects, including P-P and P-SV, as well as effects of fluids on seismic response.	Outlined potential research directions (identified in the 1999 symposium) for future research directions for seismically defining potential hydrocarbon seals and potential for seals. Included industry and other (outside UT-Austin) academic participation.	Program addressed what industry required from academia. Results included desire for a thesis-based MS and inclusion of seismic acquisition in the geophysical curriculum. A research focus on analysis and interpretation of multicomponent seismic data was defined.
Comment	Dr. Robert Peebler delivered the keynote address.	Topic suggested by Anadarko, one of the EDGER sponsors.	Dr. Fred Hilterman delivered the keynote address.	Dr. Peter Orteva, Indiana University, delivered the keynote address.	Dr. Tom Barron, delivered the keynote address which led to the proposal to form the EDGER FORUM at UT-Austin.

25

Research Activities & Cooperative Projects

The status of student and faculty research for the current year was presented as a part of the 12th Annual Meeting of the EDGER Forum in February. Papers and presentations of these results are posted on the EDGER Forum web page and are available upon request to sponsors. Expanded Abstracts submitted by EDGER students and faculty to the SEG for consideration in Volume 32 of the 83rd Annual International Meeting in Houston in 2013 are included in the Appendix on page 43 of this report, providing our sponsors full access to these abstracts before publication in the Fall of 2013. Current theses, dissertations and publications are available online and upon request.

Graduate students with a focus on Exploration Geophysics are included in the student summary table on pages 12 – 13. Brief comments on the research project of each student or alumnus are included. Faculty and post-doctoral research topics are included in the personnel section on page 41. At the present time, five masters students are working on thesis topics coordinated with industry sponsors, including internships and data sets from the partners. The EDGER Forum is a crucial aspect of our graduate student support, as well as the overall research program. For year thirteen, EDGER Forum graduates and faculty have completed over 35 publications (June 2012-May 2013).

Faculty Expertise

Research projects are organized into broad subject areas and championed by the Co-PI's as follows:

◊ Interpretation of Multicomponent Seismic Data (Tatham)
◊ Imaging Seismic Data in Complex Media (Sen/ Stoffa)
◊ Modeling / Inversion of Seismic Data including Anisotropy (Sen)
◊ Numerical Simulation of Geophysical Processes (Stoffa)
◊ Statistical and Computational Rock Physics (Spikes)
◊ Quantitative seismic interpretation for rock rock properties (Spikes/Sen)

Research Directions

To summarize current research aspects of our objectives, the research focus of the EDGER Forum has been analysis, imaging and interpretation of multicomponent seismic data. This includes development of seismic inversion algorithms and rock-physics analyses to provide an integrated suite of seismic data analysis tools. These three related aspects are being applied to shale characterization as well as to geophysical descriptions of conventional reservoirs for both fluid extraction and fluid storage.

Professor Tatham and his students are currently working on seismic analyses of the Woodford and Marcellus Shales, specifically variation in Poisson's ratio and anisotropy parameters within the shales. Additional projects include polarization corrections for SV- and SH-waves in isotropic and anisotropic media.

Professor Spikes and his students continue to link quantitatively pore-scale reservoir characteristics to larger scale geophysical measurements. The emphasis is primarily on unconventional reservoirs, and the Bakken and Haynesville Shale in particular. Additional work is being

done to understand the effects of CO_2 on seismic responses for EOR and CCUS technologies. Finally, comparisons are being made between numerical wave propagation and effective medium models to assess the viability of both for use in quantitative interpretation.

Professor Sen and his students and post docs continue to work on a wide range of topics. These include wave-propagation modeling, inversion-based reservoir characterization for conventional and fractured reservoirs, and rock models for various reservoir types.

Professor Stoffa will be working more closely with the EDGER Forum and will be advising students in the area of numerical simulation of seismic wave propagation in elastic media. Several projects with students in both the Computational and Applied Math and Post-Doc researchers were included in the annual meeting presentations. The opportunity to interact with the Texas Advanced Computing Center (TACC), located in a building shared by the UT Institute for Geophysics on the J. J. Pickle Research campus, enhances likelihood of success in this endeavor. Both the Lone Star and Ranger 'supercomputers' are part of TACC.

The emphasis in recent years, both within the EDGER forum and in the industry as a whole, suggests potential partnerships between UT and interested parties from the Forum. This would provide opportunities to transfer and share technological advancements between industry and academia.

For the past several years, our annual technical symposium has focused on land assets and unconventional resources, whereas the earlier symposia of the EDGER forum focused on seismic

characterization of seals. We envision a trend emerging of using seismic methods to look at shales, which can be a source, seal and/or reservoir. Several students are focusing on the seismic response to resource shales. Modeling parameters are derived from borehole log data, including dipole sonic or sonic scanner log data, and relation to actual productivity are largely hypothesized from anecdotal information. As available productivity information independent of completion techniques applied and the strategies of drilling programs are realized, seismic observations are expected to play a more significant role in defining drilling and completion decisions. Faculty, student and post-doctoral research will likely continue in this area for the foreseeable future. The 2013 Technical Symposium included specific topics in how comprehensive analysis of seismic data may improve commercial success in unconventional resources and is leading to several new cooperative projects.

Progress reports of current cooperative projects were discussed at the 2013 Annual Meeting & Technical Symposium. Faculty, PhD and MS students and post-doctoral researchers at the annual meeting made presentations, and we expect to see additional applications of seismic-based analysis to active reservoir monitoring and perhaps to microseismic monitoring.

This unconventional reservoir application area also dominated the topics of recent annual technical symposia. It has led to several cooperative UT / industry projects with student research theses and dissertations addressing particular issues associated with resources plays. Working collaboratively with our industry partners, cooperative projects, along with industry internships (over 50 to date) are instrumental in developing graduate students thesis topics.

Cooperative Projects

Focus Area of Application	Project	Student/Faculty	Partner
Unconventional Resources	Woodford Shale	Alexander Lamb (MS 2012)	Devon / Cimarex
	Haynesville	Kwon Taek Oh (MS 2012)	BP
		Meijuan Jiang	
		Qi Ren	Chevron
		Sarah Coyle	
	Marcellus Shale	Sharif Morshed	Anadarko
	Fracture Modeling	Lauren Becker	Evolving
	Elastic Deformation	Han Liu	Evolving
Time Lapse Seismic and Reservoir Monitoring	Cranfield Carbon Sequestration Project	Russell Carter	Gulf Coast Carbon Center (BEG)
		Rui Zhang	Evolving with support from DOE & the Center for Subsurface Energy Security
Inversion of Seismic	Stochastic Inversion	Yang Xue	Shell

Topic—Interpretation of Multicomponent Data

Understanding fracture orientation by removing polarization distortion for direct shear waves
Terence Campbell, PhD Candidate
Supervisor: Robert H. Tatham

The progressive growth of onshore shale production (gas and liquids) to replace the increasing number of aging oil fields may necessitate the use of seismic shear wave data for full characterization of shale reservoir properties for defining and developing these resources. This includes descriptions of anisotropy for characterization of fractures (HTI) as well as the internal nature of the shales (VTI). Seismic shear-wave data may play an important role in characterizing anisotropy in shales. This includes the polarization information inherently contained in shear-wave data.

The objectives of this study are to 1) document the distortion in polarization of seismic shear waves upon reflection; and 2) address a correction, based on an understanding of shear amplitude versus incidence angle behavior, that corrects for the distortion, especially at mid- and far-offset angles. This includes demonstration of the efficacy of the proposed correction by applying it to real shear wave source data. This should result in a minimized distorted amplitude response that arises from polarization distortion upon reflection. This correction is supported by apparent consistency of the zero crossing of the SV-SV reflectivity near 20-24 degrees for common impedance contrasts and the remarkably regular behavior of the SV-SV reflectivity curve following an A+BSin2 Θ relation. This observation may offer the opportunity for a stable correction with minimal sensitivity to detailed knowledge of contrasts in velocity and density. Some key questions must be addressed to gain a full understanding of shear wave distortion upon reflection for varying model data: 1) How do we address reflected polarization distortion for isotropic media for varying incidence angles? And 2) How d we apply this correction for an isotropic medium overlying a HTI medium, which can be used to simulate real data. 3) Applications to real data and how distorted amplitudes can be corrected to identify real HTI anisotropy not observed in polarization distortion reflections. One significant result of this research is a proposed extension of the Alford rotation method of shear-wave data to include all offset data, and not just the normal incidence data.

AVO attributes (P-P and P-SV)
Patrick Gustie, M.S. Student
Supervisor: Robert H. Tatham

Patrick Gustie will be addressing amplitude variation with offset analysis (AVO) for his MS thesis research. He is particularly interested in exploring ways to better illustrate AVO information, particularly that which is related to the characterization of fracture orientation and pore aspect ratio. He has been exploring the many variations of AVO analysis, especially in defining useful attributes using both P-P and P-SV reflectivity. AVO crossplots involving color-coding have encouraged Patrick to explore new attributes that can be used in AVO crossplots that he hopes will improve lithology discrimination. One possible hypothesis is to plot the coefficient of the Poisson's ratio (PR) term

in Shuey's AVO equation, except instead using several powers of the sine term for P-P and P-SV reflectivity. A subsequent color-coded crossplot may lead to a greater separator between different characteristics and may translate into an improved color background reflectivity section. Additionally, Patrick intends to experiment with crossplot axis rotation to allow for a NI*PR product section with improved discriminatory capability. The use of color in reflectivity sections adds an additional dimension to the images and greatly assists geophysics in presenting and interpreting lithological information which ultimately leads to improved decision making such as well location. The benefits of the NI-PR crossplots may be built upon to not only delineate lithologies but could also help delineate other rock characteristics such as pore aspect ratio, fracture density, fracture intensity, and fracture orientation, as long as multi-azimuthal information is incorporated.

Multi-offset Alford rotation on direct shear-wave data
Jacqui Maleski, M.S. Student
Supervisor: Robert H. Tatham

The reflection process distorts shear wave polarizations and, therefore, hampers travel-time based analysis. For my thesis, I plan to use methods developed by previous students to correct for polarization distortion of direct shear reflections in 3D nine-component (9C) seismic land data acquired at the Vacuum Field in Lea County, New Mexico. Travel-time analysis of split shear waves provides valuable information regarding subsurface anisotropy. Aligned fractures, which largely control the transport of fluids, are a major cause of

anisotropy. However, it is imperative the that effects of polarization distortion are first removed if subsurface anisotropy is to be properly characterized and interpreted in terms of shear wave travel-times. Previous geophysical studies performed at Vacuum Field indicate that the magnitude and direction of anisotropy varies with depth. This condition requires the use of layer stripping, in which the effects of each anisotropic layer are sequentially removed, beginning at the surface and continuing down to the target layer, from the entire data record. The effectiveness of the proposed methods will advance the broad goal to increase the utility and understanding of shear waves in exploration seismology. Current progress includes producing synthetic seismograms to model the seismic response in a controlled environment and test the effectiveness of the methods under simple conditions. I am currently waiting for the Vacuum Field data to be transferred from the Colorado School of Mines, but will begin analysis upon its arrival.

Topic—Direct Inversion of P-P and Data

Gas-hydrates saturation estimation in Krishna-Godavari basin, India
Kumar Sundaram Das, M.S. Geo. Sci.
Supervisor: Mrinal K. Sen

Gas hydrates are an unconventional energy resource. They may become an important source of energy for India in the future. They occur offshore along the continental margin. They are currently in exploratory and evaluation stages and their quantification is an important task. The goal of this thesis is to demonstrate

a new technique for the estimation of gas hydrates volumes. The region of study is the Krishna-Godavari basin. It is located on the eastern offshore areas of India. The presence of gas hydrates has been proven by drilling into marine sediments as a part of the Indian National Gas Hydrates Program. Borehole subsurface and surface seismic data were collected during this expedition. I use a 2D seismic reflection line and borehole log data for my study. The method I use for estimation of gas hydrates saturation uses a combination of inversion of seismic reflection data and development of seismic attributes.

My approach can be broadly described by following steps. 1) Process the seismic data to remove noise. Use stacked and migrated data along with well logs to perform poststack seismic inversion to obtain impedance information in volumetric portions of the subsurface. 2) Use NMO corrected CDP gather records of the seismic reflection data along with subsurface well logs to perform prestack seismic inversion to obtain impedance volumes. 3) Compare the results from step1 and step 2 and use the best results to perform multi-attribute analysis using a neural network method to predict resistivity and porosity logs at the well location. Use the transform equations obtained at the well location to predict the well logs throughout the seismic section in the desired zone of interest. 4) Use an anisotropic equivalent of Archie's law that relates resistivity and porosity to saturation to predict saturation throughout the seismic reflection section.

The majority of the previous work done in the region is limited to gas hydrates quantification only at the well location. By using neural networks for multi-

attribute analysis, I have demonstrated a statistical based method for the prediction of log properties away from well location. My results suggest gas hydrates saturation in the range of 50-80% in the zone of interest. The estimated saturation of gas hydrates matches up very closely with the saturation estimates obtained from the cores recovered during coring of the boreholes. Hence my method provides reliable methods of quantification of gas hydrates by making best possible use of seismic and well log data. The unique combination of impedance derived attributes and neural-network includes the non-linear behavior in the predictive transform relationships. The use of an anisotropic formulation of Archie's law to estimate saturation also produces accurate results confirmed with the observed gas-hydrates saturation.

A Plane-Wave based Seismic Interferometry for Controlled Source Data
Yi Tao, PhD Fall 2012
Supervisor: Mrinal K. Sen

We propose a new approach to retrieve virtual seismic responses to subsurface variation by cross correlating controlled-source seismic data sets in the plane wave domain. This method is based on slant stacking over shot or receiver locations of observed seismic data to produce plane-wave transforms of data gather. Cross-correlation is then performed by selecting the same ray parameters from different shot or receiver locations. Unlike a traditional approach where the correlogram is obtained from cross correlating recorded data that contains the full range of ray parameters, this method directly selects common ray parameters to address unique ray paths. Thus, it can

sometimes avoid spurious arrivals when the acquisition requirement of seismic interferometry is not strictly met. In addition, in the plane-wave domain we can choose certain ranges of ray parameters and can focus on energy from limited directions. This method can also help reduce computation time because plane-wave transformed data usually results in a reduction of the original data volume.

Application of New Monte Carlo Method for Inversion of Prestack Seismic Data
Yang Xue, PhD Candidate
Supervisor: Mrinal K. Sen

Yang Xue is working on novel stochastic inversion methods for reservoir characterization and reservoir monitoring. She has developed a new stochastic inversion method, called Greedy Annealed Importance Sampling (GAIS), for an efficient and accurate estimation of both elastic properties and their uncertainties. She applied this method to both trace-by-trace seismic inversion of post- and pre-stack data and simultaneous inversion along 2D lines. The results indicate that GAIS can estimate both the expectation value and the uncertainties more accurately than using VFSA alone. Furthermore, principal component analysis (PCA) as an efficient parameterization method is employed together with GAIS to improve lateral continuity by simultaneous inversion of all traces. The second part of her research involves estimation of reservoir permeability models and their uncertainties using quantitative joint inversion of dynamic measurements,

including synthetic production data and time-lapse seismic related data. Impact from different objective functions or different data sets on the model uncertainty and model predictability is investigated as well. The results demonstrate that joint inversion of production data and time-lapse seismic related data reduces model uncertainty, improves model predictability and shows superior performance than inversion using one type of data alone.

Basis Pursuit Inversion (BPI) for pre- stack and post-stack data
Rui Zhang, Postdoctoral Fellow
UT Institute of Geophysics (UTIG)

Rui Zhang's primary research interest focuses on reservoir characterization using high-resolution seismic inversion techniques. This research results in a Basis Pursuit Inversion (BPI) to derive high-resolution reflectivity and impedance estimates. This technique has been extended to seismic data int eh prestack domain.
He is also interested in the time-lapse seismic technique and working on CO_2 sequestration projects for enhanced oil recovery. The BPI method has been applied on the time-lapse seismic to monitor the CO_2 plume.

A prestack Basis Pursuit Inversion (BPI) of Seismic Data

Resolving thin layers and clearly delineating impedance layer boundaries in inverted seismic data are important for exploration and production of hydrocarbons. Many seismic inversion methods based on a least-squares optimization approach with Tikhonov-type regularization can lead to unfocused transitions between adjacent layers. A Basis Pursuit Inversion (BPI) algorithm based on a L1 norm optimization method can, however, resolve sharp boundaries between layers. Here we formulate a BPI algorithm for amplitude-versus-angle (AVA) inversion and investigate its potential to improve definition of contrasts between layers. Like the BPI for post-stack case (Zhang and Castagna, 2011), the sparse layer constraint rather than sparse spike constraint is utilized to construct the model space as a wedge dictionary. All the examples in the dictionary are beds reflectivities, which include solutions consisting of thin beds as well as thicker units. Based on this dictionary, we also use an L1 norm optimization framework to derive two reflectivities, namely, R_p, R_s and contrasts in ρ. Although BPI does not require an initial model, high resolution velocities (V_p, V_s) and density (ρ) can be obtained by incorporating initial models in the BPI derived reflectivity. Tests on synthetic and field data show that the BPI algorithm can indeed detect and enhance layer boundaries by effectively removing the wavelet interference.

Time-lapse thin- bed seismic inversion for CO_2 sequestration: A case study from Cranfield, Mississippi
(published in the International Journal of Greenhouse Gas Control)

A carbon dioxide sequestration study has been carried out at Cranfield, Mississippi by injecting a million tons of CO_2 into the lower Tuscaloosa sandstone formation over two years from 2008 to 2010. Time-lapse seismic surveys were recorded at pre- (2007) and post- (2010) injection to monitor movement of the subsurface fluid plume. The injection interval in the well, appearing as a thin layer defined by the well-log data, shows very weak signature of CO_2 injection in the time-lapse seismic amplitude over the two year monitoring interval. To address this, we applied a Basis Pursuit Inversion (BPI) method on the seismic datasets, which was developed by incorporating a priori information as a wedge dictionary with a L1-norm optimization solution for improved resolution. The inverted acoustic impedance with improved resolution shows a strong decrease in acoustic impedance mostly at the top of the injection interval from the time-lapse seismic data. Thus the inverted time-lapse acoustic impedances can be used to detect CO_2 movements, which demonstrates an effective way to monitor the subsurface CO_2 plume.

Topic—Imaging, with a focus on Anisotropy

Removing anisotropic overburden effect for reliable reservoir fractures characterization

Mohammed Alhussain, PhD Spring 2013
Supervisor: Mrinal K. Sen

Mohammed Alhussain completed his PhD in May 2013. His research title is Fracture Characterization of a Carbonate Reservoir in Saudi Arabia. The objective is to develop newly hypothesized techniques for seismic characterization of fractured reservoirs with the goal of investigating their applicability to description of a carbonate reservoir in Saudi Arabia. His work includes integration of well logs and 3D seismic data provided by the field operation.

We have developed an amplitude ratio method that can be used for direct quantitative estimation of fracture parameters, including normal and tangential weaknesses, ΔN and ΔT, respectively. We employ a least-squares fit of the amplitude variation with offset (angle or ray parameter) and azimuth (AVOA). The model for the least-squares fit is a linearized reflection coefficient for anisotropic media that is a function of the two fracture compliances. Inversion of synthetic P-P AVOA data for ΔN and ΔT parameters reveals that the ΔN parameter is reliably estimated given accurate background isotropic parameters. While ΔN estimation is successful, inversion for ΔT parameter from Rpp information is not, presumably due to the dependence of ΔT on medium parameters that are not constrained by the PP data. We further modified the AVOA inversion approach to be applied to amplitude ratio data and demonstrate that the ΔN parameter is successfully recovered. High ΔN values can be attributed to high crack density values and vice versa. The ΔN parameter inversion is also applied to the amplitude ratios derived from real seismic data acquired on the Arabian Peninsula. Inversion results indicate greater concentration of fractures located at the hinge of an anticline structure. Spatial variability in fracture parameters has proven valuable in locating "sweet spots" or highly fractured zones within the reservoir interval.

Sub-salt imaging with wide-aperture seismic data

Zeyu Zhao, PhD Candidate
Supervisor: Mrinal K. Sen

Since sub-basalt regions have become targets of hydrocarbon exploration, great effort has been put on seismically imaging the relatively low velocity sediments, which are often overlain by very high velocity layers such as basalt. Compared with commonly used seismic acquisition geometry, the acquisition system applied in the sub-basalt investigation is usually composed of long-offset multichannel streamers, and the acquired data is often called long-offset or wide-aperture seismic data. The wide-aperture seismic data generally contains not only sub – critical reflections, but also large offset refraction and post-critical reflections, which may be crucial to successful sub-basalt imaging. However, conventional seismic reflection processing methods, mainly manipulating the data in the traveltime-offset (T-X) domain, are not fully applicable to the large offset data because the data violates the assumption

within the root-mean-square (rms) approximation that the propagation angles of seismic wave should be small. Further, common processing practice would treat reflection and refraction observations independently, even if they are somewhat related and need to be addressed simultaneously.

These difficulties can be overcome by means of transforming the seismic data from T-X domain to the tau-p (delay time and ray parameter) domain using slant stacking. In the tau-p domain, these three types of seismic events can be reorganized into a single elliptical trajectory and can be treated simultaneously. By taking advantages of a different domain, the analysis will be generally more physically meaningful conducted in both the T-X domain and the tau-p domain.

Topic—Reservoir Monitoring and Shale Characterization

Reservoir characterization for the Haynesville Shale
Meijuan Jiang, PhD Candidate
Supervisor: Kyle T. Spikes

Meijuan Jiang is a Ph.D. candidate in geophysics. She entered the University of Texas at Austin in 2010. She characterizes the reservoir properties of the Haynesville Shale by integrating rock physics modeling and seismic inversion. The reservoir properties she is interested in include porosity, lithology and pore shape, which provide very useful information in determining locations with relatively high porosities and relatively large fractions of brittle components

favorable for hydraulic fracturing. She built a workflow that combines an isotropic and an anisotropic effective medium model with a grid-search method to invert for these reservoir properties. The isotropic effective medium model represents a complex medium as a single homogeneous medium by including grains and pores of different shapes and sizes. The anisotropic effective medium model introduces vertical transversely isotropic media through aligned fractures. After building the relationships between the reservoir properties and P- and S-wave velocities, she uses grid searching to obtain porosity, composition and pore shape distributions conditioned by the rock-physics models. The modeled seismic velocities that satisfy criteria from objective functions provide reservoir property estimations. So far, the porosity and composition estimations at the well location matched the observations from log and core data quite well, and the pore shape estimation suggested that the pores, cracks, and fractures within the Haynesville Shale have elongated shapes. In addition, Meijuan is also working on pre-stack seismic inversion to obtain P- and S-impedances, and she will apply the workflow at the seismic scale and estimate the continuous distributions of the reservoir properties for the Haynesville Shale, along with an assessment of the uncertainty. These continuous reservoir property distributions will help her to understand which rock properties or combination of properties cause the spatial variations in seismic attributes.

Characterization of Seismic Anisotropy of the Marcellus Shale from Borehole Data
Sharif Morshed, M.S. Student
Supervisor: Robert H. Tatham

Sharif Morshed's research is focused on quantitative seismic interpretation of resource shale. He uses both rock physics modeling and petrophysical analysis, together with seismic modeling for the purpose of quantitative seismic interpretation. In his MS thesis, he worked on rock physics modeling analysis and surface seismic modeling analysis for understanding the seismic signature of the Marcellus Shale formation. For the rock physics side, he used DEM (Differential Effective Medium) model to explore the relationships between elastic parameters with reservoir petrophysical properties. Sharif found that the elastic properties are controlled by the interplay of clay content, kerogen content and the geometric aspect ratio of non-spherical pores. Following the rock physics modeling, he worked on surface seismic modeling for isotropic and VTI (Transversely Isotropic with Vertical symmetry axis) anisotropic 1D earth model. From the seismic modeling I analyzed the P-P and P-SV reflection amplitude variations with offset. He found that seismic reflections are most sensitive to kerogen content but also sensitive to anisotropic parameters and the aspect ratio of kerogen inclusions. Additionally, three different types of elastic wave reflections i.e. P-P, P-SV and SV-SV respond differently to anisotropic parameters. Therefore, multicomponent seismic reflection data is inherently useful for the seismic characterization of the organic shale. Before his MS study at UT Austin, Sharif worked on seismic interpretation of Rashidpur Gas field (Bangladesh) to better understand the reservoir structure and depositional environment.

Examination of Haynesville Rock Properties
Qi Ren, PhD Student
Supervisors: Kyle T. Spikes and Mrinal K. Sen

Qi Ren currently works on two projects. One is Haynesville Shale Modeling as her Ph.D program, using both seismic and well log data supplied by EDGER Forum members from the Haynesville Shale in Panola, Texas. The first step of this project is rock physics modeling, stepping from isotropic models to anisotropic models. This modeling will cover scenarios with different composition, fluid type and pore aspect ratios. The isotropic modeling will use self-consistent model and differential effective model (DEM), and the anisotropic modeling will start with anisotropic DEM model. The Haynesville Shale is highly anisotropic. Thus the anisotropic modeling is very important. After the rock physics effort, she will do forward seismic modeling and AVO inversion. With long-offset pre-stack seismic data, she can do the three-term AVO waveform inversion. The resulting density reflectivity could say something about kerogen content. In addition, the density contrast is the best indicator for Haynesville, separating from the Bossier above.

The other project is a joint one with petrophysics and geostatistics for the Eagle Ford Shale. Qi's work aims at rock properties modeling with well log data. She has already done the isotropic

modeling. Also, the sensitivity of composition, especially kerogen, and pore aspect ratio to velocity and Young's modulus has been analyzed by isotropic DEM model. Next, she will move on to anisotropy modeling, starting with the anisotropic DEM model.

Inversion of Seismic Data with and without rock-typing
Sarah Coyle, M.S. Student
Supervisor: Kyle T. Spikes

Sarah Coyle is working on rock physics modeling of the Haynesville Shale both with and without rock-typing in order to evaluate its effectiveness in constraining seismic inversion. She is developing two workflows using a combination of the Self Consistent Approximation and Differential Effective Medium Model for modeling the vertical heterogeneity in the Haynesville. The first workflow accounts for vertical heterogeneity in elastic properties in the Haynesville using a single 'rock type' model with varying pore shape distribution and mineral composition. The second workflow takes advantage of rock-typing by dividing the Haynesville into different rock sections and assigning different models that best characterize the individual intervals. In this way, change in rock fabric can also be accounted for in the model. After evaluating the ability of both model types to replicate sonic logs in wells from the Haynesville, she will invert the seismic volume for useful rock properties and identify intervals ideal for horizontal drilling and hydraulic fracture within the Haynesville Shale.

Rock physics and seismic characterization of the Cranfield CO_2 injection site
Russell Carter, PhD Candidate
Supervisor: Kyle T. Spikes

Russell Carter will be entering his fourth year as a PhD student. His work involves characterizing and monitoring of injected CO2 in the Cranfield reservoir. His research involves integration of rock physics, well-logs, 3D and time-lapse vertical seismic profiles, and time-lapse surface seismic data. The project goal is to use statistical rock physics and seismic data to characterize the lateral extent and spread of injected CO2. Recent developments have included a probabilistic joint inversion of the contact cement model for porosity and fluid saturation at monitoring well at the project site. Future work will involve expanding the joint inversion so that the input data comes from surface seismic data and the 3D vertical seismic profile to help generate probabilistic porosity and fluid saturation volumes for the entire reservoir.

Time-lapse seismic analysis of the Norne Field, Norway
Karl Sletten
Visiting M.S. Student
Supervisors: R. H. Tatham and P. Stoffa

Karl Sletten is currently working on both prestack and poststack time-lapse seismic from the Norne field, the Norwegian Sea. He is working on interpretation of a new method for 4D seismic imaging, which is patented by professor Paul Stoffa. In order to quantify the value of adding the effects of this method, he is planning to compare the results with both reservoir

simulation and more traditional methods for 4D seismic interpretation. This is the first time this method has been used for 4D seismic imaging has been tried out on real 3D time-lapse seismic data, so many sources of uncertainty are involved. Other aspects of Karl's present and possible future work involves velocity model building, migration, and prestack inversion. So far he has made an initial velocity model by using manual picks and constrained velocity inversion.

Characterization of a saturated, fractured porous rock and estimation of its fracture-fluid factors
Jiao Xue, Visiting Student
Supervisors: Robert H. Tatham
and Mrinal K.Sen

Jiao Xue's current research is about characterization of saturated porous reservoirs with dipping/vertical fractures. For the simplest case of hydraulically isolated and rotationally symmetric fractured reservoirs, the fractures can be characterized by two parameters, normal and tangential excess fracture compliances. Jiao Xue is interested in the characterization of fractures both in the hydraulic isolated case and hydraulic connected case. Her research is not only about the low frequency limit condition but also the intermediate to high frequency condition. As mentioned, the hydraulic isolated fractured reservoir can be characterized by normal and tangential fracture compliance, which is related to fracture density and physical properties of the host rock. The hydraulic connected fractures with equant pores are more interesting and meaningful, as the equant pores have enough volume to hold the hydrocarbons and the fractures, as the volume of them is very small, act

as conduits. In the low frequency limit, we may consider the fractured reservoirs as a combination of linear-slip model and Gassmann's theory. At intermediate frequency, the fluid flow between the fractures and pores causes attenuation and dispersion, which are related to the frequency. Similar to Gassmann's theory, Biot's poroelasticity theory is about the substitution not only for the low frequency limit. Using the linear-slip model and Biot's poroelasticity theory, we can study the characteristics of the fractures, attenuation and dispersion at intermediate frequency, without considering the geometry of the fractures and pores. For penny shaped cracks, the attenuation and dispersion will also be investigated and compared with the above model with Biot's theory. In the end, Jiao intends to compare the above models, optimize and combine them for the seismic exploration.

Topic—Numerical simulations

GPU acceleration implementation for simulation of microseismic events
Makoto Sadahiro, M.S. Student
Supervisors: Paul Stoffa
and Robert H. Tatham

Makoto Sadahiro works under the tutorage of Dr. Paul Stoffa and Dr. Robert Tatham. He will look into the simulation/visualization work environment for the wave propagation of micro-seismic events. One immediate outcome of his work is the implementation of accelerated micro-seismic wave propagation modeler/simulator that is based on the GPU. The tool is intended to help better understand micro-seismic events during hydraulic fracturing. The GPU-accelerated

implementation of wave propagation modeler/simulator at the small scale allows us to test our hypothesis of wave source locations quickly and repeatedly on single GPU-equipped laptop computers. A motivation of developing this acoustic wave propagation modeler/simulator is to eventually apply this facility to more complex wave types, such as elastic, anisotropic, and poro elastic.

Analysis of Fracture-Related Sesimic Attenuation and Scattering: Insights Gained Through Numerical Modeling
Lauren Becker, M.S. Student
Supervisor: Kyle T. Spikes

Lauren Becker is continuing her research on the characterization of subsurface fracture network orientation, geometry, and fill attributes through the study of seismic energy attenuation, wavefield scattering, and directional phase velocities. By implementing finite element modeling and wave propagation methods, Lauren is able to model two dimensional fracture networks and the propagation of seismic waves through this medium. With a controlled model, it is possible to vary individual fracture attributes and predict the seismic signature of each attribute. For example, scattering in the P-wave wavefield with the addition of fractures is known to be the result of reverberations between the fractures. Studies have shown that the spacing of these reverberations, or seismic coda, decreases as the fracture spacing decreases. Studies have also indicated that the strength of the seismic coda can be related to the attenuation properties of the fracture fill. To begin this fracture attribute study, Lauren populated the finite element model with a range of simple geometries. Those geometries include evenly spaced, parallel, vertical, and gas filled fractures with variable but uniform spacing from infinite (isotropic medium) to zero (approximately horizontal transversely isotropic medium). The results of this experiment are currently being compared with the studies alluded to above to validate the finite element model and to further develop the modeling code in areas where short coming were noted. After the model has been validated, Lauren will focus this study on characterizing the seismic response of more complex fracture networks, namely fracture clusters, orthorhombic media, and addition of heterogeneities along with the fractures.

Finite element wave propagation through microstructural images
Han Liu, PhD Student
Supervisor: Kyle T. Spikes

Han Liu's research topic is finite element simulation of wave propagation in complex media. The aim of this research is to provide improved estimation of elastic properties of rocks having complex geometrical shape distribution and types of fluid fills. Compared with homogeneous fractured media, which predicts the overall elastic parameters of an isotropic medium embedded with scattered isolated aligned cracks, the simulation of discrete fracture media calculates the elastic parameters in the neighboring region of the host medium where individual fractures exist and the seismic responses of individual fractures can be examined. Therefore, Han will build several digital rock models of fractured medium with different shapes and then more accurate velocity can be estimated under hydraulic fluid pressure.

Nowadays, both geoscientists and drilling engineers expect to know the mechanism for hydraulic fractures. One assumption is that the highly pressurized hydraulic fluid induced and connected the existing small natural fractures. The other assumption is that the new fracture was induced to grow gradually along the fracture orientation. The velocities obtained from simulations of wave propagation before and after hydraulic fracture are able to differentiate two assumptions and tell which assumption is correct in reference to time-lapse seismic data. Currently, Han is working on the finite element program to implement the Discontinuous Galerkin method on shale with complex fracture shape with help of scanning electron microscope (SEM) images. The SEM images come from a shale formation. The finite element program is not restricted to obtain velocity for small-scale fracture, and it will be able to solve large-scale fractured medium problems as well and obtain synthetic seismograms. Eventually this study will reveal characteristics of the seismic response in various fractured medium and validate existing fracture inversion schemes.

Relevant Publications (2012 - 2013)

Alhussain, M., and M. K. Sen, 2012, Removing anisotropic overburden effect for reliable reservoir fracture characterization, 82nd Annual International Meeting, SEG, Expanded Abstracts, 1-5.

AlMuhaidib, Abdulaziz, M. K. Sen, and M. Nafi Toksoz, 2012, Integration of geology, rock physics, logs and pre-stack seismic for reservoir porosity estimation, AAPG Bulletin, 96, 1235-1251

Campbell, T. & Tatham, R. H., 2013, Rotation of Shear-Wave Components at Non-Normal Angles of Incidence, Accepted for the 75th EAGE Conference & Exhibition incorporating SPE EUROPEC, London June 2013

Campbell, T. & Tatham, R. H., 2012, Corrections for polarization distortion in reflected shear waves and possible extensions to the Alford rotation at non-normal incidence angles and applications, Expanded Abstracts, Vol. 31, 82nd Annual International Meeting, Society of Exploration Geophysicists, 31, MS E-P1-1.8

Carter, R. W., and K. T. Spikes, 2013, Sensitivity analysis of Tuscaloosa Sandstones to CO_2 saturation, Cranfield Field, Cranfield, MS: International Journal of Greenhouse Gas Control, in press

Carter, R. and K. T. Spikes, 2012, Modeling fluid composition in CO_2-saturated sandstone using a statistical rock physics approach, Cranfield Field, Cranfield, MS, Abstract MR33A-2429 presented at 2012 Fall Meeting, AGU, San Francisco, Calif., 3-7 Dec.

Ghosh, R., and M. K. Sen, 2012 Predicting subsurface CO_2 movement: from laboratory to field scale, Geophysics,77(3), M27–M37

Jiang, M. and K. T. Spikes, 2012, Characterizing the reservoir properties of the Haynesville Shale using rock-physics modeling and a grid search method: Geophysical Journal International, in review.

Jiang, M. and K. T. Spikes, 2012, Estimation of the porosity an pore aspect ratio of the Haynesville Shale using the self-consistent model and a grid search method, Expanded Abstracts of the 82nd Annual Meeting of the SEG, 31, http://dx.doi.org/10.1190/segam2012-0134.1

Kongrath, S., R. H. Tatham, & K. T. Spikes, 2012, Comparison of Fluid Prediction Success between AVO and Bright Spot Techniques in the Marco Polo Field, The Gulf of Mexico, International Petroleum Technology Conference, Bangkok, Feb. 2012. IPTC 14573

Liu, T., M. K. Sen, T. Hu, and J. D. DeBasabe, 2012, Dispersion analysis of the spectral element method using a triangular mesh, Wave Motion, Wave Motion, Volume 49, Issue 4, June 2012, Pages 474-483

Liu, Y. and M. K. Sen, 2012, Time-space domain dispersion relation based finite-difference method with arbitrary even-order accuracy for the 2D acoustic wave equation, Journal of Computational Physics, http://dx.doi.org/j.jcp.2012.08.025.

Liu, Yang and M. K. Sen, 2012, A hybrid absorbing boundary condition for elastic staggered grid modeling, Geophysical Prospecting, DOI: 10.1111/j.1365-2478.2011.01051.x.

Martinsen, O. J., M. Talwani, C. Dengo, B. Barkhouse, J.F. Dunn, A. Levander, C. Link, S. Mosher, J. Orcutt, D. Paul, R. Talley, R. H. Tatham, 2012, A U.S. human resource challenge for Earth science education and energy exploration and exploitation, The Leading Edge, v31, no6, June 2012

Moyano, B., K. T. Spikes, T. A. Johansen, N. H. Mondol, 2012, Modeling compaction effects on the elastic properties of clay-water composites: Geophysics, 77, 5, 1–13, DOI: 10.1190/GEO2011-0426.1

Oh, K. T. and K. T. Spikes, 2012, Velocity modeling to determine pore aspect ratios of the Haynesville Shale, Expanded Abstracts of the 82nd Annual Meeting of the SEG, 31, http://dx.doi.org/10.1190/segam2012-0508.1

Relevant Publications (2012 - 2013)

Saraswat, P. and M. K. Sen, 2012, Artifical neural systems based self organizing maps for seismic facies analysis, Geophysics July 2012 v. 77 no. 4 p. O45-O53

Saraswat, P. and M. K. Sen, 2012, Pre-stack inversion of angle gathers using hybrid evolutionary algorithm, Journal of Seismic Exploration, Vol 21, No. 2, May 2012

Sen, M. K., and P. L. Stoffa, 2013, Global Optimization Methods is Geophysical Inversion, Second Edition, Cambridge University Press, In Press

Shahin, A. and K. Kerry, P. L. Stoffa, R. H. Tatham, 2012, Petro-electric modeling for CSEM reservoir characterization and monitoring, Geophysics, January 2012, v. 77, p. E9-E20, doi:10.1190/geo2010-0329.1

Shahin, A., P. L. Stoffa, R. H. Tatham, R. K. Seif, 2012, Time-lapse seismic modelling: Accuracy required to detect signals from a water flooded reservoir, J. Seismic Explor., 21, 49-82, 2012

Spikes, K. T., 2012, Overview of rock property relationships and characterization methods for selected oil and gas shales in North America: Geohorizons, January Issue

Spikes, K. T. and Jiang, M., 2013, Rock physics relationships between elastic and reservoir properties in the Haynesville Shale: AAPG Memoir, in press.

Spikes, K. T., 2013, Error estimation of VTI behavior in shale, in review.

Stewart, R., K. T. Spikes, J. Sisson, S. Hall, J. Huang, and S. Danbom, 2012, Outstanding in the field: Hands-on geophysical education: The Leading Edge, 31, 3, 278–284

Tao, Y., and M. K. Sen, 2013, Frequency domain full waveform inversion with plane wave data, Geophysics, VOL. 78, NO. 1 (JANUARY-FEBRUARY 2013); P. R13–R23.

Tao, Y., M. K. Sen, R. Zhang, and K. T. Spikes, 2013, A robust stochastic inversion workflow for time-lapse data: hybrid starting model and double-difference inversion, in review

Tao, Y., and M. K. Sen, 2012, Subtracting non-Gaussian noise in reverse time migration, Geophysical Prospecting, In Press.

Tao, L., T. Hu, M. K. Sen, J. Yang, R. Wang, J. Wei, 2012. A hybrid scheme for seismic modeling based on Galerkin method, Geophysical Journal International, doi: 10.1111/j.1365-246X.2011.05094.x

Tatham, R. H. and A. M. Perez, 2012, Azimuthal effects of structural dip and CMP bin size on reflection travel times, EAGE 74th Annual Conference and Exhibition, Copenhagen (X032)

Tatham, R. H. and P. M. Krail, 2012, Physical Insight into the Elastic Brewster's Angle, EAGE 74th Annual Conference and Exhibition, Copenhagen (CO17)

Tatham, R. H. and P. M. Krail, 2012, Zero crossings, the elastic Brewster's angle and physical insight into shear-wave reflections, Vol. 31, 82nd Annual International Meeting, Society of Exploration Geophysicists, 31, MS E-P1.7,

Tatham, R. H., 2012, Invited paper-Seismic Applications in the Exploration for and Development and Production of Unconventional Hydrocarbon Resources (An overview), Geohorizons, 17, 1 5-17.

Zhang, R., M. K. Sen, and S. Srinivasan, 2013, Pre-stack basis pursuit inversion, Geophysics, VOL. 78, NO. 1 (JANUARY-FEBRUARY 2013); P. R1–R11.

Zhang, R., M. K. Sen, S.Phan, and S. Srinivasan, 2012, Stochastic and deterministic seismic inversion methods for thin-bed resolution, Journal of Geophysics and Engineering, October 2012, v. 9, p. 611-618, doi:10.1088/1742-2132/9/5/61

Personnel

Robert H. Tatham

Dr. Tatham is a Professor in the Department of Geological Sciences and holds the Shell Companies Foundation Centennial Chair in Geophysics. He joined the faculty in 1999 and has more than 30 years experience both in the contracting and major production segments of the industry. He is Principal Investigator for the EDGER Forum.

Mrinal K. Sen

Dr. Sen is a Professor for the Department of Geological Sciences and UTIG. He holds the Jackson Chair in Applied Seismology and is the current Director of the National Geophysical Research Institute (NGRI). He advises graduate students in all areas of Geophysics and applied mathematics at UTIG, where he has been a researcher since 1989. He is Co-Principal Investigator for the EDGER Forum.

Kyle T. Spikes

Dr. Spikes joined the Faculty in 2009 as an Assistant Professor with a focus in rock physics. He completed his PhD at Stanford University in 2008. Before arriving at UT-Austin, Dr. Spikes was a Post-Doctoral Fellow at the University of Bergen in Norway. He is Co- Principal Investigator for the EDGER Forum.

Paul L. Stoffa

Dr. Stoffa is a Professor for the Department of Geological Sciences and holds the UTIG Shell Distinguished Chair in Geophysics. He was Director of UTIG from 1994-2008. He actively advises graduate students supported by the EDGER Forum and working on sponsored research.

Margo C. Grace

Ms. Grace is the Project Coordinator for the EDGER Forum and is responsible for organizing, developing and promoting events including workshops, symposia and meetings. She maintains websites and databases and develops member services as well as overseeing the budget, sponsor contracts and the financial status of EDGER Forum funds.

Thomas E. Hess

Mr. Hess provides crucial technical support for the EDGER Forum's research efforts as Seismic Applications Software Manager. He oversees seismic data sets from our sponsors and supports graduate students, faculty and researchers for the Exploration Geophysics program in the Dept. of Geological Sciences as well as for the UT Institute for Geophysics.

Jiancong Xiong

Jiancong Xiong, Senior Engineer at Sinopec, will be working with the EDGER team in 2013-2014 as a visiting scientist. Xiong will conduct research into seismic anisotropic properties pertaining to the characterization of shale resources. Results of this research will lead to methodologies, which will provide guidance to the both exploration and production of shale resources.

Other faculty and researchers

Faculty and research scientists from all three branches of the Jackson School of Geosciences, the Dept. of Petroleum & Geosystems Engineering, and the Texas Institute for Computational and Applied Mathematics continue to participate in various activities of the EDGER Forum and support graduate students with a focus in exploration geophysics

Special Thanks to All our Sponsors!

Appendix

Quantitative estimation of fracture parameters after removing anisotropic overburden effect

Mohammed Alhussain* and Mrinal K. Sen[1], The University of Texas at Austin, [1] UT Austin and NGRI Hyderabad, India

Summary

We have developed an amplitude ratio method that can be used for direct quantitative estimation of fracture parameters, including normal and tangential weaknesses, ΔN and ΔT, respectively. We employ a least-squares fit of the amplitude variation with offset (angle or ray parameter) and azimuth (AVOA). The model for the least-squares fit is a linearized reflection coefficient for anisotropic media that is a function of the two fracture compliances. Inversion of synthetic P-P AVOA data for ΔN and ΔT parameters reveals that the ΔN parameter is reliably estimated given accurate background isotropic parameters. While ΔN estimation is successful, inversion for ΔT parameter from Rpp information is not, presumably due to the dependence of ΔT on medium parameters that are not constrained by the PP data. We further modified the AVOA inversion approach to be applied to amplitude ratio data and demonstrate that the ΔN parameter is successfully recovered. High ΔN values can be attributed to high crack density values and vice versa. The ΔN parameter inversion is also applied to the amplitude ratios derived from real seismic data acquired on the Arabian Peninsula. Inversion results indicate greater concentration of fractures located at the hinge of an anticline structure. Spatial variability in fracture parameters has proven valuable in locating "sweet spots" or highly fractured zones within the reservoir interval.

Introduction

All amplitude variation with offset (AVO) inversion methods assume that amplitude variation is caused by reflections from a well isolated reflector. Cumulative effects of seismic waves propagating in the overburden can distort the amplitudes of seismic reflections from a target reservoir. Such effects can be even more significant in anisotropic media. Many factors can distort amplitudes, including shallow sediments such as sand dunes, regional and local structural variations, sinkholes, shallow channels, and anisotropy in shallow layers.

The need to account for such effects has been recognized by Luo et al. (2005, 2007), Liu et al. (2011), and others. Transmission effects caused by the presence of anisotropic layers in the overburden, for example, can easily hinder the AVOA analysis, which can lead to unreliable estimates of anisotropic reservoir parameters (Sen et al., 2007). Therefore, erroneous amplitude analysis of the reservoir may result if overburden effects are ignored.

Alhussain and Sen (2012) presented a method to remove the effect of an anisotropic overburden to recover reservoir fracture parameters. It involves analyzing AVOA for a reservoir pick and for a reflector below the reservoir. Seismic gathers are transformed to delay time slowness domain and the ratio of reservoir pick to the layer below the reservoir is taken to remove transmission effect from the overburden. As an example, a four layer model is shown in Figure 1. The corresponding ratio equation is

$$Ratio = \frac{T_{1\rightarrow2}^{down}T_{2\rightarrow3}^{down}R_3 T_{3\rightarrow2}^{up}T_{2\rightarrow1}^{up}}{T_{1\rightarrow2}^{down}R_2 T_{2\rightarrow1}^{up}} = T_{2\rightarrow3}^{down}\left(\frac{R_3}{R_2}\right)T_{3\rightarrow2}^{up}, \quad (1)$$

where $T_{1\rightarrow2}^{down}, T_{2\rightarrow1}^{up}, T_{2\rightarrow3}^{down}, T_{3\rightarrow2}^{up}$ are upward and downward transmission coefficients between layers 1, 2 and 3. R_3 and R_2 are reflection amplitudes for layer interface. Figure 1 also shows the model used for equation 1.

In this paper we extend the idea of Alhussain and Sen (2012) further and devise a technique to directly estimate two fracture parameters ΔN and ΔT.
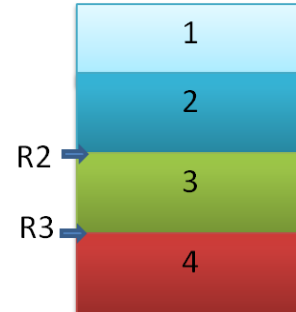
Figure 1: A four-layer model where R2 and R3 are defined in equation 1 to demonstrate the removal of the transmitted ray paths.

Forward synthetic models

To investigate the effect of an anisotropic overburden on AVOA analysis, Alhussain and Sen (2012) introduced two models. The first one consists of an anhydrite cap rock, a vertically fractured carbonate reservoir and an isotropic overburden. The second model is the same but with an added anisotropic section in the overburden that includes a layer with vertical fractures. Both models are shown in Figures 2a and 2b.

Quantitative estimation of fracture parameters

Well log interpretation shows that the reservoir has a coarsening upward sequence where the quality of the reservoir gradually improves upward. This is clearly indicated by lower P- and S-wave velocities, and lower density values at the top of the reservoir. To depict reservoir parameters closely, the reservoir is divided into 14 layers each with different Vp, Vs, density and prorosity values. Figure 3 shows how these four parameters gradually vary across different depths of the reservoir in a manner simillar to the logs. Crack density and orientations are set to be constant in all layers.
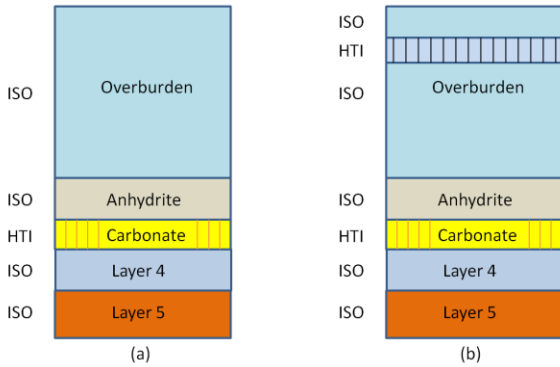
Figure 2: (a) Forward model including anhydrite cap rock and vertically fractured carbonate reservoir and isotropic overburden. (b) Same model with added anisotropic section in the overburden.
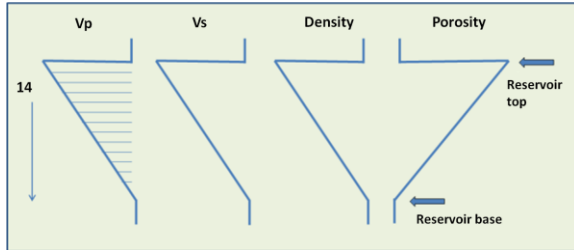
Figure 3: Reservoir interval is divided into 14 different horizontal layers. Each layer has a different set of reservoir property values.

For each of the 14 reservoir layers, five independent effective medium parameters that represent a horizontal transverse isotropic medium (HTI) are derived for a saturated porous fractured reservoir using the Gurevich (2003) model. Then, a full-waveform numerical simulation (Mallick and Frazer, 1991) is performed on both models for several source-receiver offsets and azimuths. Offset values are from zero to 3,200 m in increments of 80 m. The dominant frequency of the wavelet used is 35 Hz, and the target horizon is at a depth of 1,500 m. The resultant

gathers, the zero azimuth direction for each model, are shown in Figures 4a and 4b.
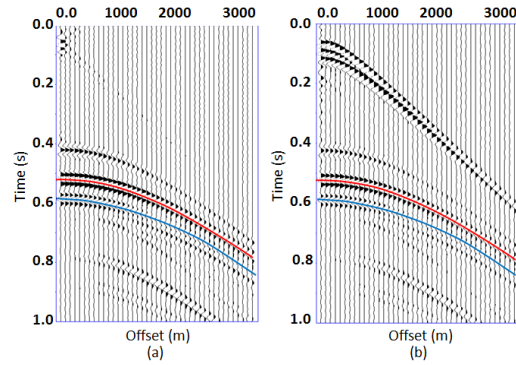
Figure 4: Full-waveform synthetic CMP gathers for two models. One with an isotropic overburden (a) and the other is with anisotropic overburden (b). Red and blue picks denote reservoir top and a layer below reservoir respectively.

Estimating ΔN and ΔT from a fractured synthetic model

Synthetic azimuthal CMP gathers generated from the model in Figure 2a are used to invert for ΔN and ΔT. The ΔN and ΔT values for each reservoir layer are calculated directly from elastic coefficients of the HTI medium using the equations (Bakulin et al., 2000):

$$\epsilon^{(v)} = \frac{C_{11} - C_{33}}{2C_{33}}, \tag{2}$$

$$\delta^{(v)} = \frac{(C_{13} + C_{55})^2 - (C_{13} - C_{55})^2}{2C_{33}(C_{33} - C_{55})}, \tag{3}$$

$$\Delta N = -\frac{\epsilon^{(v)}}{2g(1-g)}, \tag{4}$$

$$\Delta T = \frac{1}{2g}\left[\frac{1-2g}{1-g}\epsilon^{(v)} - \delta^{(v)}\right], \tag{5}$$

$$g = \frac{V_s^2}{V_p^2}. \tag{6}$$

The ΔN and ΔT values are shown in Figure 5.
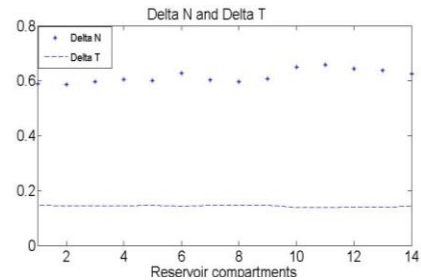
Figure 5: ΔN and ΔT computed values for 14 reservoir layers.

Quantitative estimation of fracture parameters

Both parameters are almost constant in all reservoir units, and the average values are 0.62 and 0.14 for ΔN and ΔT, respectively. This is extremely helpful because we can invert for one value for each parameter that represents the entire reservoir unit.

AVOA inversion for ΔN and ΔT parameters

Shaw and Sen (2006) derived linearized reflection coefficients directly as a function of fracture weaknesses by presenting a weak anisotropic medium as a volume of scatterers embedded in a background isotopic medium:

$$\delta R = R_{pp}^{obs}(i,\emptyset) - R_{pp}^{iso}(i) = A_{sens}\Delta, \qquad (7)$$

$$A_{sens} = \frac{1}{4}[a_N, a_V, a_H, a_{NV}, a_{NH}, a_{VH}]. \qquad (8)$$

Here R_{pp}^{obs} is the observed reflection coefficient, and R_{pp}^{iso} is the reflection coefficient of the isotopic background. A_{sens} is the sensitivity matrix which is a function of incidence angle, azimuth and background isotropic medium parameters. The elements of the matrix are defined by Shaw and Sen (2006).

Equation 7 is used to invert for ΔN and ΔT. To perform the inversion, knowledge of the orientation of the vertical fractures as well as information about the physical parameters of the isotropic background (Vp/Vs) are required. For the synthetic example both parameters are available. In equation 7, the term $R_{pp}^{iso}(i)$ is the reflection coefficient for the interface separating the overlying medium from the isotropic medium in which fractures are embedded. $R_{pp}^{iso}(i)$ is set to be equal to $R_{pp}^{fracture\ parallel}(i)$ where seismic waves do not see fractures as they travel parallel to them. The isotropic reflection coefficient term is subtracted from the observed amplitude data to isolate the effect of fractures on the AVOA.

A linear least-squares inversion is performed to estimate the fracture weaknesses ΔN and ΔT:

$$\Delta = [A_{sens}{}^T A_{sens}]^{-1} A_{sens}{}^T \delta R, \qquad (9)$$

where $\Delta^T = [\Delta N\ \Delta T]$ and we set $a^T = (a^V + a^H)/2$.

Inverted ΔN and ΔT are equal to 0.64 and -0.048, respectively, and the average values calculated directly from input parameters are 0.62 and 0.14. This demonstrates that ΔN is successfully inverted for, but ΔT is not. We attribute this difficulty in the parameter estimation to the complexity of equations 3 and 5 where ΔT depends on many medium parameters for accurate prediction. It

depends on $C_{11}, C_{33}, C_{13}, C_{55}, and\ V_p/V_s$. The effect of ΔT on PP-reflection coefficients is prominent at large angles of incidence only (Shaw and Sen, 2006). This behavior is similar to the effect of S-wave velocity on PP-reflection coefficient from an interface separating two isotropic media. On the other hand, ΔN depends only on $C_{11}, C_{33},$ and V_p/V_s and the effect of ΔN on the reflection coefficients occurs at most incidence angles.

It is important to understand the significance of ΔN and how it is related to fracture parameter prediction. Note that ΔN can be related to crack density by the following equation (Schoenberg and Douma, 1988):

$$\Delta N = \frac{4e}{3g(1-g)}, \qquad (10)$$

where e is crack density and $g = \frac{V_s^2}{V_p^2}$.

Assuming that we have an accurate value of Vp/Vs, we can have a good idea about crack density, and ΔN can then be used to invert for fracture density parameter.

Proposed ΔN and ΔT inversion method

The ratio attribute that corresponds to two models, one has an isotropic overburden (Figure 2a) and the other has anisotropic overburden (Figure 2b), are used here to invert for both ΔN and ΔT parameters. Equation 7 is modified to use ratio amplitudes instead of conventional AVOA as follows:

$$\delta R = Rratio_{pp}^{obs}(i,\emptyset) - Rratio_{pp}^{iso}(i) = \frac{A_{sens}}{R_{pp}^{top}(i,\emptyset)*\propto}, \quad (11)$$

where $Rratio_{pp}^{obs}$ is the ratio amplitudes of the observed data and is a function of angle and azimuth. $Rratio_{pp}^{iso}$ is the ratio amplitude for isotropic background and is a function of angle. A_{sens} is the sensitivity matrix normalized by R_{pp}^{top}, which is the reflection amplitudes of top reservoir as a function of angle and azimuth. $\propto$ is a scalar.

Inversion results of both models (Isotropic and anisotropic overburden) are 0.551 and 0.546 for ΔN and -5.94 and -8.6 for ΔT. It can be concluded that ΔN is reasonably estimated (with 11% and 12% error) when compared to the derived value (0.62) from HTI elastic coefficients. We believe that this discrepancy in ΔN is related to the composite effect of the term: $T_{2\rightarrow3}^{down}(R_3/R_2)T_{3\rightarrow2}^{up}$ of equation 1. The ratio of the reflection coefficient of a reflector below the reservoir R_3 and reservoir top R_2 at a different angle of incidence and azimuth could be the cause of the deviation of ΔN estimation.

Quantitative estimation of fracture parameters

Overall, we demonstrate that the ΔN parameter can be successfully inverted for using the ratio method. On the other hand, the inversion of ΔT parameters is unstable for the same reasons mentioned in the previous section.

Inversion of ΔN from real data

The inversion of the ratio attribute from synthetic data for ΔN parameter is stable. This motivated us to apply the method to real data despite the fact that quantitative analysis of real data is challenging. A real surface PP seismic data acquired on the Arabian Peninsula is used here. The target formation is an Upper Jurassic carbonate reservoir, composed primarily of limestone with associated traces of dolomite. The structure is defined by a NW-SE oriented, elongate-asymmetric, anticline that is doubly plunging. The anticline is controlled by a deep seated fault that cuts the section below the reservoir formation and ceases to cut the reservoir. The reservoir is overlain by an anhydrite layer.

Equation 11 is used for our inversion. The observed ratio attribute, which is a function of angle and azimuth represents the term $Rratio_{pp}^{obs}$. The isotropic part the ratio attribute or $Rratio_{pp}^{iso}$ is taken to be the ratio attribute for fracture strike azimuth direction. This means that the inversion requires knowledge about fracture direction. Another important parameter needed for the inversion is Vp/Vs ratio, which is estimated from the well logs in the area. This parameter is assumed to be a constant.

Inversion results for ΔN can be seen in Figure 6. Crack density are calculated directly from ΔN parameter using equation 9 (Figure 7). Hot colors correspond to high and can be interpreted as high crack density. On the other hand, cold colors indicate low crack density areas. The inversion result indicates that more fractures are located at the anticline structure hinge.

Conclusion

In this paper we demonstrated the applicability of AVOA inversion for direct estimation of fracture compliances. AVOA inversion results for a synthetic model show that ΔN is reliably estimated as long as the background isotropic parameter is estimated with good accuracy. This information is usually taken from well log information. On the other hand, inversion for ΔT from Rpp information is not successful and we attribute that to the dependence of ΔT on many medium parameters, namely, $C_{11}, C_{33}, C_{13}, C_{55},$ and v_p/v_s. Another reason is that the effect of ΔT on PP-reflection coefficients is prominent at large angles of incidence only. The best solution to the problem is to acquire a multicomponent survey where converted waves can help to estimate ΔT (Shaw et al., 2007).

The inversion is also done to the amplitude ratio attribute. ΔN is also reliably inverted for with some discrepancy, which we believe is related to the composite effect of the term: $T_{2\rightarrow3}^{down}(R_3/R_2)T_{3\rightarrow2}^{up}$ of equation 1. The ratio of reflection coefficient of a reflector below the reservoir R_3 and reservoir top R_2 at different angles of incidence and azimuth could be the cause of the deviation of ΔN estimation. An important parameter needed for the inversion is Vp/Vs ratio, which is estimated from well logs in the area. Inversion of real data from Arabian Peninsula indicates that more fractures are located at the hinge of the anticline structure.
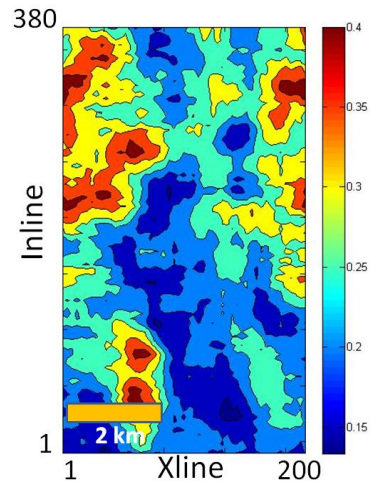
Figure 6: Inverted ΔN parameter from real data. Hot colors indicate high values which correspond to high fracture zones.
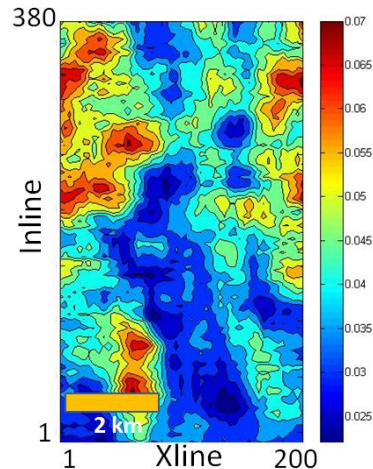
Figure 7: Inverted fracture density from ΔN parameter. Hot colors indicate high fracture zones.

Rotation of Shear-Wave Components at Non-Normal Angles of Incidence

T.A. Campbell (Univ of Texas at Austin, Currently ConocoPhillips)
& R.H. Tatham* (University of Texas at Austin)

Introduction

Analysis of propagating seismic shear waves, with their transverse polarization, is potentially quite useful in characterizing internal properties of the media they travel through. This is particularly true for anisotropic properties associated with cracks, fractures and the presence of clay minerals in shales. This usefulness is simplified by utilizing a single S-wave propagation path and analysis of variations in shear-wave polarization directions. Alford (1986) introduced a method of rotating combinations of observed seismic traces from orthogonal pairs of horizontal shear-source and shear-receiver components to identify the azimuthal orientations of symmetry axes of birefringence. Typically they

are associated with a simplified anisotropy symmetry commonly defined as azimuthal anisotropy with a horizontal axis of symmetry (HTI). This method has been widely applied to interpretation of subsurface fracture properties by assuming HTI anisotropy results from aligned fractures. Numerous studies (e.g., Lynn et al., 1999; Hitchings and Potters, 2000) illustrate the efficacy of polarization analysis for estimating anisotropy as a proxy for fracture properties..

Figure 1: Reflection coefficients for SV-SV and SH-SH waves showing that the reflection coefficients vanish at some angles of incidence for typical velocity and density contrasts. The positions of three critical angles are shown. The zero crossing is at 20° for SV and 40° for SH polarizations.(Campbell and Tatham, 2012).

Alford rotation analysis, as currently applied, is limited to zero-offset (normal incident) reflection paths. This results because the normal incidence reflection response is identical for SV and SH reflectivity relative to a common Cartesian coordinate system. For non-normal incidence angles, however, there is a pronounced difference in SV and SH reflectivity as source-receiver offsets increase, leading to significant distortion in the polarity of the reflected shear wave relative to the source polarization, Figure 1. Typically, reflection of an arbitrarily polarized shear wave is described in terms of SH and SV components relative to the vertical plane connecting the source and receiver positions. For acquisition of 3D seismic data with fixed orientations of horizontal sources and receivers in a planar distribution of source and receiver positions over Earth's surface, the vertical plane connecting individual source and receiver orientations does not, in general, align solely with the SV or SH orientations associated with vertical profile connecting the source and receiver locations. In Figure 2, we note that for a shear source located at the origin in the diagram, with a polarization in the east direction ($\Psi = 0$), a source-receiver azimuth at Θ, and a pair of shear-receiver components oriented in the X-Y, or east and north, directions will record a shear-wave, reflected at the mid-point, with a polarization oriented an angle L; this differs notably from the original source polarization. This polarization distortion results from the large differences in the SH and SV reflectivity. As seen in Figure 1, at incidence angles beyond about 15°, these differences distort the resultant polarization of the reflected wave—even in this purely isotropic setting.

Method and Theory

Corrections to this polarization distortion may be realized by correcting for the Amplitude Variations with Angles of incidence (or Offset) AVO observed in the separate SV-SV and SH-SH reflection curves observed in Figure 1. The polarization of a single shear source can then be projected to SV and SH components for the vertical plane defined by the source and receiver positions. The corrections for the different amplitudes for the SV and SH components can be applied by normalization to zero offset, and then the polarization of the reflected shear wave determined by the orthogonal horizontal receiver components at the receiver position. Of course, this correction requires some knowledge of the AVO behavior at the individual SV and SH reflection relations for each source-receiver azimuth.
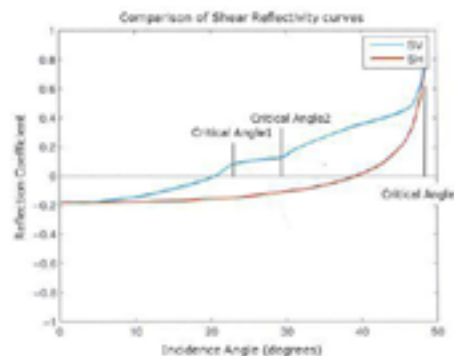
Figure 2. Acquisition configuration of source (center) a receiver (triangles) positions for a 3D direct horizontal shear-source survey.

Figure 3: Upper panel: Observed polarizations (map view) in a simulated 3D source record (source at center) for an isotropic media with a reflector at 2.0 km. The base of each arrow is the location of the two components of the shear receiver, and the length of the arrows is the amplitude. Their orientations show the observed reflection polarization (source polarization is due east). The dashed red circle is the offset for ___ = 20°, the zero-crossing for the SV-SV reflectivity. The SH-SH zero crossing is at 40°. *Lower panel:* Results of the corrections, using the simplified reflectivity equations. Note the consistency of the corrected polarization to offsets beyond the 20° zero crossing. Also note the limits of the correction near the 20° zero crossings (Campbell and Tatham, 2011).

To implement such corrections, we apply simplifying assumptions for the Zoeppritz equation proposed by Spratt et al. (1993) and Lyons (2006). Spratt et al. (1993) proposed using typical assumptions of small incidence angles and small contrasts in velocities and density to give the following forms for the reflectivity relations:

$$R_{sv-sv} = A + B_{sv} \sin^2 \boxtimes \qquad (1)$$

and

$$R_{sh-sh} = A + B_{sh} \sin^2 \boxtimes \boxtimes \qquad (2)$$

where R is the angle-dependent reflectivity and A and B are the intercept and slope of a linear relation to $\sin^2 \boxtimes$. Lyons (2006), based similar simplifying assumptions, modified the SH reflectivity to:

$$R_{sh-sh} = A + B_{sh} \tan^2 \boxtimes . \qquad (3)$$

Because both the SV-SV and SH-SH reflectivity curves do have zero crossing at relatively modest angles of incidence for typical values of velocities and densities encountered in sedimentary rocks (near 20° for SV and 40° for SV), we can use these simplified $\sin^2$ and $\tan^2$ relations to estimate the actual Zoeppritz equations to select the values of the zero crossing angles. Because we are correcting to zero offset, A is set to unity. B is estimated from knowledge of A (unity) and the value of the amplitude (zero) at the zero crossing estimated from the simplified Zoeppritz′ equations. Significantly, the only parameters required for the calculation of the correction are the angles of the zero crossings. (Spratt et al. 1993 Gumble, 2006, Lyons, 2006)

A numerical example of this polarization distortion and correction for a single shear source polarization in an isotropic medium is illustrated in Figure 3. The uncorrected data (upper panel) show significant polarization distortion at offsets near the SV zero-crossing. The corrected (lower panel) data show a quite consistent conformity to the observed reflection polarizations relative to source polarization at angles approaching the SH zero crossing. A singularity in the correction occurs at the SV zero crossing, and erratic results are deleted.

Extension of Alford′s Rotation to non -Normal Incidence Angles.

Expanding this single-source polarization correction to include two orthogonal source orientations and two orthogonal receiver orientations is straightforward. Thus, we propose to extend the Alford (1986) rotation to non-normal angles of incidence by minimizing the polarization distortion upon reflection for each source component for all the receiver locations associated with this single source position. This leads to four traces associated with a given pair of source and receiver positions in the survey. These sets of traces can then be sorted into other configurations, such as source (shot) or CMP gathers.

In the presence of HTI anisotropy, cross-term energy in the four-trace sets is produced when wave source polarizations are at an arbitrary angle relative to the principal axes of symmetry of the HTI anisotropy. Applying the rotation analysis as proposed by Alford (1986) is valid only for normal angles of incidence. Hence, we hypothesize that by applying the proposed polarization correction to the original multi-offset data prior to applying Alford's rotation should extend rotation analysis to include non-normal angles of incidence. This is illustrated with an example applied to synthesized data generated by a method of Mallick and Frazer (1987). The parameters for this single reflector between an isotropic and anisotropic layer are given in Table I. The anisotropy of the lower layer does impose a polarity modification upon reflection (Campbell and Tatham, 2012), which is preserved during propagation through the isotropic upper layer to the surface.

Example

Figure 4 shows the simulated data using the isotropic over anisotropic model (Table I) for a 2D shot record oriented at 30° to the fracture direction. The fracture orientation is in the X direction of an X-Y survey grid, with both the source and receiver orientations in the X and Y directions. Note that offsets are represented by angles of incidence from 0 to 45 degrees. The four panels are for traces from the X-oriented source into the X oriented receivers (X-X) in the survey grid, Y-oriented source recorded by X oriented receivers (Y-X), X oriented source and Y oriented receivers (X-Y) and Y oriented source and Y oriented receivers (Y-Y). In the zero-offset analysis using current Alford rotation methods, the applicable data would be limited to only four traces, X-X, Y-X, X-Y and Y-Y for the zero offset values. From the Zoeprittz equations, the zero crossings for the SV-SV and SH-SH reflectivity are near 20° and 40°, respectively. Because none of the four shot records is purely SH-SH or SV-SV, we fail to fully isolate the zero-crossings. Do note, however, that the energy is concentrated in the X-X and Y-Y quadrants. At angles of incidence beyond about 25°, there is energy in both the diagonal and off-diagonal quadrants.

Figure 5 shows the same data with the appropriate polarization corrections applied to all offsets to compensate for the SV and SH effects. The subsequently applied rotation accounts for a fracture direction at 30° to the source-receiver azimuth. Note the minimal energy in the off-diagonal Y-X and X-Y cross-terms, especially at larger angles of incidence beyond the 20° SV-SV zero crossing. Also note the isolation of energy to the SV-SV and SH-SH polarizations when the proper rotation correction is reached.

A preliminary scan of rotations shows total energy in the X-X and Y-Y (diagonal) quadrants and the Y-X and X-Y off-diagonal quadrants is summarized in Figure 6. This result is simply the sum of all angles of incidenc for the entire range

Model Parameters	
Layer 1 (Isotropic)	Vp=3.0km/sec Vs=1.5km/sec ρ=2.00g/cm^3 h=2.00 km
Layer 2 (Anisotropic, HTI)	Vp(0)=4.0km/sec Vs(0)=2.0km/sec =0.30 δ=0.10 γ=0.02 ρ=2.2g/cm^3

Table I. *Properties of an anisotropic media, V_P is the P-wave velocity, V_S is the shear wave velocity. $V_P(0)$ and $V_S(0)$ are the vertical P- and S- velocities in the* HTI medium, and ε, δ, and γ are *the Thomsen(1986) parameters.*

Figure 4: *Simulated source record for an X and Y oriented source and multiple off-set X and Y receivers. Offsets are noted in angles of incidence. (Campbell & Tatham, 2012)*

Figure 5: *4-C source record from Fig. 4, rotated to align with known HTI symmetry (Campbell and Tatham, 2012).*
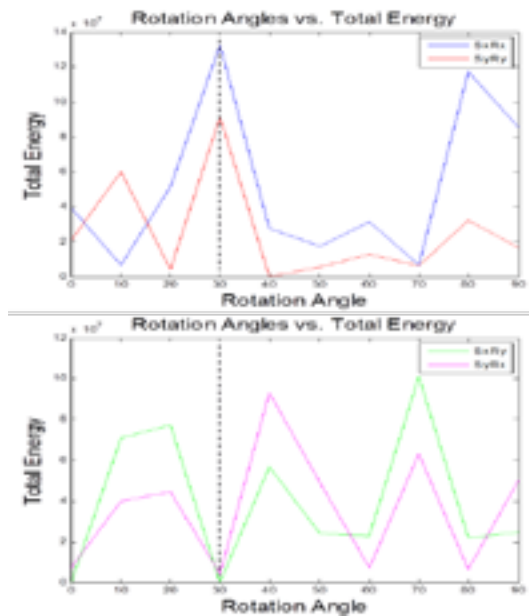
Figure 6: *Rotation scans on the data of Fig. 4 for angles from 0° to 90°. Note the min. in the X-X and Y-Y terms at 30°, as seen in Fig. 5.*

of incidence angles in the shot record for each of the quadrant pairs, after corrections for each rotation angle. Note the maximum in energy at the 30° rotation angle (and the minimum in energy for the off-diagonal terms), consistent with the expected polarization for the model.

Conclusions and Discussion

Polarization distortion due to the effects of the reflection process on shear-to-shear reflectivity for shear-source orientation in typical 3D acquisition geometry is demonstrated, and a correction to the polarization distortion is proposed. For modest angles of incidence and small contrasts in acoustic and shear impedance, the only information required for the correction are the angles of SV-SV and SH-SH zero crossings—which tend to occur in a small range of angles, near 20° for SV and 40° for SH for most sedimentary rocks. This correction can be applied to four-component direct shear data at non-zero source-receiver offsets, leading to an extension of the widely applied Alford rotation to non-zero angles of incidence. Such corrections may lead to improved capability of polarization information for analysis of anisotropic properties in the subsurface.

Limitations of shear-wave rotation analyses include the impact of transmission through shallow anisotropic media, which impose polarities on the recorded shear data—masking further polarization analysis. Layer stripping schemes have been implemented to current Alford rotation analyses to overcome this effect. Adaption of such layer-stripping to the non-zero offset case is the next logical step in the extension of Alford rotation methods to non-normal angles of incidence.

References

Alford, R. M., (1986) Shear data in the presence of azimuthal anisotropy, Dilley Texas— Expanded Abstracts, 56th Annual International Mtg, Soc. of Exploration Geophysicists, 476-479.

Campbell, T., and Tatham, R. H. (2011) Correction for distortion in polarization of reflected shear-waves in isotropic and anisotropic media**,** Exp. Abstr., 81st Ann. Intl. Mtg, Soc. of Explor. Geophy., **30**, 1333-1337

Campbell, T. and Tatham, R. H. (2012) Corrections for polarization distortion in reflected shear Waves and possible extensions to the Alford rotation at non-normal incidence angles & applications—Expanded Abst., Vol. 31, 82nd Ann. Intl. Mtg, Soc. of Explor. Geophy. **31**, MS E-P1-1.8

Gumble, J. E. (2006) Complete anisotropic analysis of three component seismic data related to the Marine environment and comparison to nine component land seismic data: Ph.D. diss. Univ. of Texas-Austin.

Hitchings, V.H., and Potters, H. 2000, Production and geologic implications of the Natih 9-C, 3-D Seismic survey, **GeoArabia**, v. **5**, no. 4, p. 511-524.

Lynn, H.B., Beckham, W.E., Simon, K.M., Bates, C.R., Layman, M., and Jones, M., 1999, P- & S-Wave azimuthal anisotropy at a naturally fractured gas reservoir, Bluebell-Altamont Field, Utah, **Geophysics**, v. **64**. No. 4: p. 1312-1328

Lyons, E. S. (2006) Polarization rotation upon reflection of direct shear waves in purely isotropic media: M.S. thesis, University of Texas at Austin.

Mallick, S., and L. N. Frazer (1987) Practical aspects of reflectivity modeling,: **Geophysics**, **52**, 1355–1364.

Spratt, R. S., N. R. Goins, & T. J. Fitch (1993) Pseudo-shear—The analysis of AVO, *in* M. M. Backus, ed., Offset-dependent reflectivity—Theory & Practice of AVO analysis: SEG

Thomsen, L. (1986) Weak elastic anisotropy: Geophysics, **51**, 1954–1966.

Joint rock physics inversion of well log and 3D VSP data to model CO_2 saturation and porosity at Cranfield Field, Cranfield, MS.

Russell W. Carter* and Kyle T. Spikes, The University of Texas at Austin, Jackson School of Geoscience

Summary

Analysis of the effects of injected CO_2 on the seismic response of reservoirs is important because it can provide improved characterization and monitoring of sites undergoing CO_2 injection. We completed a joint inversion of the contact cement model to better understand the effect of CO_2 saturation on the relationship between elastic parameters and reservoir properties of the Cranfield reservoir. We used p-impedance and Vp/Vs from well logs and 3D VSP data to invert jointly for porosity and fluid saturation. We calibrated a rock physics model to different depth intervals in well data from the Cranfield reservoir interval. In the two reservoir intervals Vp coefficients of 1.14 and 1.08 were for the shallow and deep portion, respectively. Vs coefficients used to correctly model the two intervals were 1.04 and .93. These coefficients correct for pressure and grain shape. We then performed fluid substitution to model density and velocity logs for different in situ CO_2 saturations. The logs, calculated to have a uniform pore fluid composition for all depth points, were input into the inverted model to generate modeled logs of saturation and porosity. Results indicated that the model was relatively accurate for porosity and fluid saturation when upscaled to represent seismic resolution. Lastly, a crossline from a 3D VSP was inverted for Ip, and a synthetic Is volume was generated. Results from the crossline at the well locations showed a relatively accurate porosity estimation. Inverting for pore fluid did not return the same degree of accuracy at this time.

Introduction

The Cranfield reservoir consists of sandstones of the Lower Tuscaloosa Formation, which has been dated regionally to be Upper Cretaceous in age. The reservoir sands of the Cranfield study area have porosities that range from 0 to 37% with an average value of 20% (Lu, et al., 2012). Permeabilities in the reservoir range from 0.1–1000 millidarcies (Lu et al., 2012). The Late Cretaceous Tuscaloosa group contains alternating sequences of sands and shales that comprise the reservoir and the reservoir seals, respectively, in the study area. An extensive regional scale marine shale is present in the Middle Tuscaloosa Formation that acts as a regional seal to the reservoir sands. The Cranfield study area is near the apex of a local anticline, which is being forced upward through the buoyant rising of a salt body (Lu et al., 2012).

The Cranfield reservoir was under production from discovery in 1943 until its initial abandonment in 1966. The site has recently been revived as a location for enhanced oil recovery and CO_2 injection and sequestration. The Gulf Coast Carbon Center at the University of Texas at Austin Bureau of Economic Geology is working with the Southeast Regional Carbon Sequestration Partnership as well as the local field operator to conduct the CO_2 sequestration study at the Cranfield site (Lu et al., 2012). The study area is located with in the 1 km^2 Detail Area Study (DAS), contained with in the red box on Figure 1. The DAS consists of three wells, one injection well, CFU-31F-1 (F-1) and two monitoring wells, CFU-31F-2 (F-2) and CFU-31F-3 (F-3), which are located down structural dip from the injection well. During CO_2 injection, injection rates into well F-1 ranged between 200 and 500 tons per day. Over the entire Cranfield area more than 3.4 million tons of CO_2 have been injected since the start of injection.
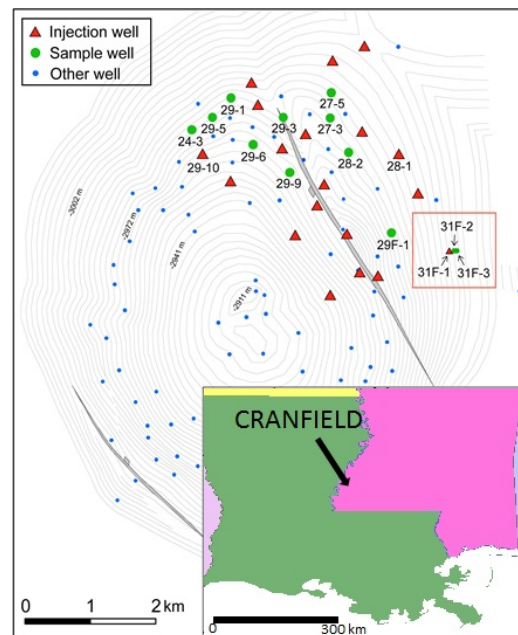
Figure 1. The entire Cranfield site. Data for this project came from the DAS (red box). The DAS contains one injection well, 31F-1 (F-1), and two monitoring wells, 31F-2 (F-2) and 31F-3 (F-3). Modified from Lu et al. (2012).

Joint inversion for porosity and pore fluid

This study integrates probabilistic joint inversion of rock physics models, fluid substitution, and 3D VSP data to help differentiate between brine and injected CO_2 in the reservoir. Data for this work consist of well logs from both injection and monitoring wells and 3-D VSP data. Carter and Spikes (2013) examined well logs from the Cranfield to determine which combinations of parameters gave the highest probability to differentiate between CO_2 and brine in the pore space. A combination of Ip and Vp/Vs were the best performing elastic properties. The work presented here uses that combination as a starting point to invert jointly porosity and fluid saturation using the contact cement model.

Theory and Methods

The contact cement model (Dvorkin and Nur, 1996) was used to link reservoir properties to the elastic parameters of the reservoir. Elastic parameters calculated from measured well logs and from well logs modified by fluid substitution were then used to invert the rock physics model to generate probabilistic logs of porosity and fluid saturation in the reservoir. Once calibrated, the models and the inversion scheme were applied to a crossline from the 3D VSP, which had been inverted for Ip and from which a synthetic Is volume was generated. The synthetic Is volume was generated by dividing the Ip volume by the average Vp/Vs in the reservoir zone from the well logs. We generated a synthetic Is volume to enable testing the model and algorithm while the mode converted s-wave volume from the 3D VSP data was still undergoing processessing.

Kordi et al. (2010) determined primary compositions at the F-2 well of 60-80% quartz, 10-20% clay, and 10-20% feldspar, with the remainder composed of small percentages of muscovite, calcite, and other minerals. Given the natural heterogeneity present in the reservoir, the rock physics model was expanded to cover a wider range of mineral compositions. The contact cement model was then run 50 times for a range of mineral compositions, ranging from 40% quartz and 60% clay to 100% quartz. Intermediate composition also contained fractions of feldspar, and calcite.

During the derivation of the contact cement model the pressure term is dropped. However, modeling the Cranfield reservoir with the contact cement model in a way that is consistent with known geology resulted in a mismatch between the measured porosity at the well location and the model porosity. To accommodate this the reservoir interval was modeled as two separate intervals, each with its own set of p- and s-wave velocity coefficients. These coefficients were 1.14 and 1.04 for the shallower interval for p- and s-waves, respectively. For the deeper interval, values of 1.08 and .93 were used. These

coefficients are interpreted to be proxies for pressure and grain shape. Velocity coefficients are consistent with the increase in velocity measured by Joy (2011) on core plugs from the Cranfield reservoir under pressure.

For this reservoir p-impedance and Vp/Vs best discriminated between different fluid compositions (Carter and Spikes, 2013). By modeling the contact cement model for all porosity and pore fluid combinations, the response of the model to fluid variations over the range of expected porosities can be examined. Model trends with the pressure corrections are shown in Figure 2. Figure 2a and b show the contact cement model for the 50 different lithologies and for pure brine in the pore space for the shallow (a) and deeper (b) portions of the reservoir. Colors in panels a and b indicate porosity, and the black data points shown are the measured well log data fluid substituted to brine. Panels c and d of Figure 2 show the same information as panels a and b with the measured data colored by porosity, and the model shown in black. The color scales for all panels are the same with red and other warm colors indicating high porosity and blue and other cool colors indicating relatively low porosity. This figure shows that for a given Vp/Vs and Ip value the modeled porosity matches closely with the measured porosity.
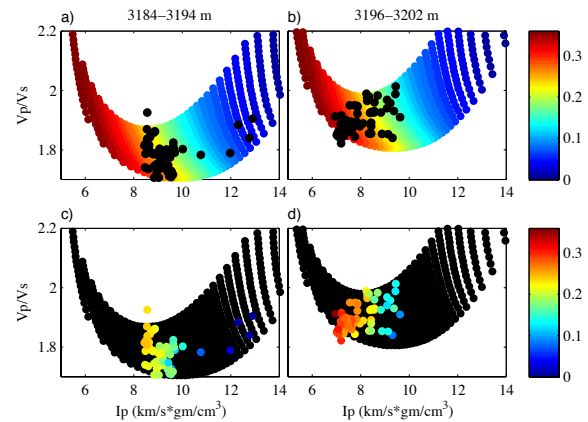
Figure 2: Modeled Vp/Vs vs p–impedance (Ip) with well log measurements color coded to porosity. All panels show Vp/Vs on the y-axis and the p-impedance (Ip) on the x-axis. In panel a the colored data points show the results of the contact cement model for 50 different lithologies each modeled for a pore fluid of pure brine. The scattered black data points are measured log data, fluid substituted to pure brine. Shading in panels a and b shows porosity of the contact cement model results. For panels c and d, the measured data points are shaded by porosity, and the model is shown in black.

After generating the models for the shallow and deep portions of the reservoir, the models were divided into bins.

The best results were obtained when the model for the shallow zone was partitioned into a relatively fine bin structure, and the deeper reservoir interval was divided by a relatively coarse bin structure. Each binned model was used to generate a Gaussian bivariate probability density function. These probability density functions provide a statistical relationship between porosity and fluid saturation for each bin. These relationships can then be used to generate inverted data with the same statistical distributions as the model.

The measured well log data, modified to represent a uniform fluid composition, were also binned according to the same Ip and Vp/Vs bins as the models. When the entire reservoir interval was binned, 500 joint normally distributed porosity and pore fluid values were assigned to each depth point. This number of joint values was chosen for each combination of Ip and Vp/Vs to examine the full extent of the potential variability and to generate a probabilistic output of porosity and pore fluid. By calculating 500 bivariate values for each depth point, probabilistic logs of porosity and fluid saturation were generated. The joint values generated for each bin of measured values of Vp/Vs and Ip were selected to have the same mean, standard deviation, and covariance as the Vp/Vs and Ip results of the contact cement model for the same bin values. This was completed once for the measured Ip and Vp/Vs with each of the following reference fluid compositions: 0, 25, and 50% CO_2, with the remainder of the pore fluid composed of brine. Measured logs were fluid substituted to the pore fluids of 0, 25 and 50% CO_2 using Gassmann (1951) fluid substitution. Probabilistic results were then upscaled using the Backus (1962) average to show results at the seismic scale.

A single crossline from the 3D VSP was also inverted using the same technique as the well logs. Ip was calculated by completing a model-based impedance inversion on the post stack 3D VSP crossline. Is was then generated from the Ip volume. Vp/Vs was generated by dividing the Ip by Is. At the 3D VSP scale the dividing line between the upper and lower portion of the reservoir was based on a picked horizon from the VSP data.

Results

Results showed that the inverted porosity tended to match measured porosity at well F-2 quite well for all reference fluid saturations. Pore fluid inversion results were not quite as accurate. Inverted pore fluid results from all reference pore fluid combinations showed a high degree of variability at the well-log scale. At the seismic scale these results were smoothed and more closely resembled the reference pore fluid values. When the input elastic parameters represented a pure brine pore fluid, the model tended to

under predict brine slightly. When the input elastic parameters corresponded to a mixture of half brine and half CO_2 the model tended to over predict brine saturation. However, as the input elastic parameters changed to represent decreasing concentrations of brine, the model did predict decreasing concentrations of brine, just not to the same degree as the change in reference data. Results of the inversion on the well log for input data representing 50% brine and 50% CO_2 are shown in Figures 3 and 4. Figure 3 shows the results of the inversion for porosity (panel a) and fluid saturation (panel b) at the log scale, and Figure 4 shows the results after being upscaled to seismic resolution.
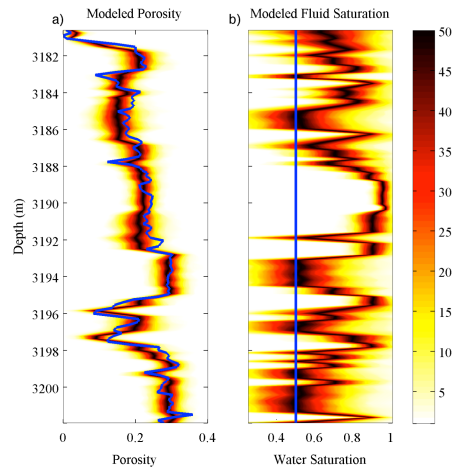
Figure 3: Results of the joint inversion for porosity and water saturation. Panel a) shows the porosity result, and panel b) shows the fluid saturation result. The blue line represents measured porosity and the fluid saturation for panel a) and panel b), respectively. The colored region in each panel represents the probability of a given porosity or saturation value being generated for a given depth point. Inverted data in both panels has had a two point moving average applied for smoothing.

Inversion of the crossline from the VSP returned a porosity section that is highly reasonable. An overlay of the upscaled porosity log from well F-2 is shown overlying the modeled porosity log from the VSP at the F-2 location in Figure 5. Figure 5 shows that much like the probabilistic inversion at the well location, this joint inversion tends to slightly under predict porosity in most of the reservoir interval. Porosity results shown in Figure 5 are the P50 probability porosity values from the probabilistic inversion of the entire crossline.

Results from the inversion of the entire crossline from the VSP are shown in Figure 6. In Figure 6 well F-2 falls at inline location 1029. Porosity values shown in Figure 6 are the P50 values returned from the probabilistic joint inversion. Results from the pore fluid inversion of the VSP

cross line are not included, as they are not deemed reliable being generated from synthetic data.
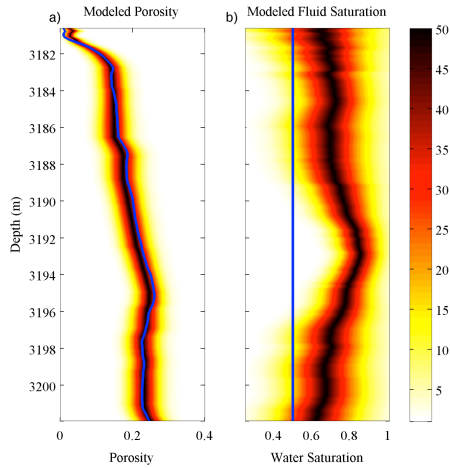
Figure 4: Results of the joint inversion for porosity and water saturation after being upscaled to seismic resolution. Panel a) shows the porosity result, and panel b) shows the fluid saturation result. The blue line represents measured porosity and the fluid saturation for panel a) and panel b), respectively. The colored region in each panel represents the probability of a given porosity or saturation value being generated for a given depth point.
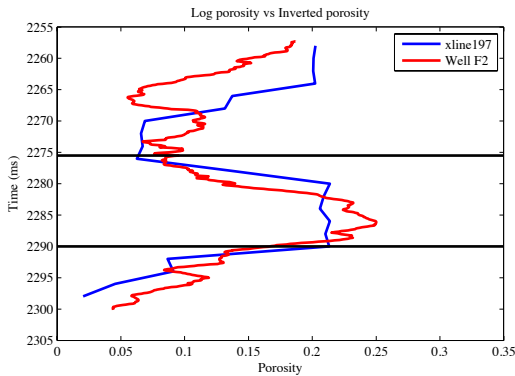
Figure 5: Results of the inversion of the VSP data at the location of well F-2. Time is on the vertical axis, and porosity is on the horizontal axis. Inverted values from the VSP are shown in blue and upscaled data taken from the porosity log of well F-2 are shown in red. Upper and lower black lines are the top and bottom of the reservoir, respectively.

Conclusions

This study showed that the contact cement model when properly calibrated, can be used to model the Cranfield reservoir for porosity. However, in this case the properties of the reservoir are such that the contact cement model tended to slightly under predict the porosity of the reservoir for a given set of Ip values. At the depth of the Cranfield

reservoir, over 3000 meters, the effective pressure is thought to be approximately 30 MPa. Given this effective pressure, unique p- and s-wave coefficients were required for each reservoir interval for the contact cement model to correctly link porosity and Ip given the relatively well constrained lithology of the Cranfield reservoir.
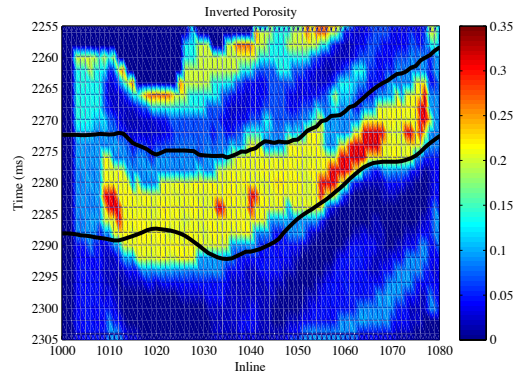
Figure 6: Results of the porosity inversion of crossline 197 from the 3D VSP. The upper and lower black lines indicate the top and bottom of the reservoir as picked from seismic data at this location. Color shading shows modeled P50 porosity values from the probabilistic inversion. Warm colors show higher porosity while cooler colors indicate lower porosity.

The joint inversion for both porosity and fluid saturation returned a porosity estimate that showed a relatively accurate match between reference and output porosity. Additionally when inverting for pore fluid at the log scale, the results showed a high degree of variability. When those same results were upscaled the results trended quite closely to the reference values. Inversion for pore fluid was sensitive to reference fluid but not sensitive enough to accurately detect small changes in gas concentration. Inversion of the single crossline from the 3D VSP returned porosity values that closely matched those of upscaled measured well logs at well location. However, due to the use of synthetic s-wave data, a reliable fluid inversion was not possible. S-wave information, currently being processed from multicomponent data, will likely allow for a pore-fluid estimate to be completed as part of the future work in this study.

Acknowledgments

Sensitivity analysis of Tuscaloosa sandstones to CO_2 saturation, Cranfield field, Cranfield, MS

Russell W. Carter[*], Kyle T. Spikes[1]

The University of Texas at Austin, Department of Geological Sciences, EPS RM 1.130, 1 University Station, C9000, Austin, TX 78712-0254, United States

ARTICLE INFO

ABSTRACT

The study of the seismic response of reservoirs containing injected CO_2 is important because it will improve monitoring and characterization of sites used for CO_2 utilization and storage. We investigated the sensitivity of the seismic properties to CO_2 saturation of the Cranfield injection site using rock physics modeling, fluid substitution, amplitude variation with angle (AVA), and statistical classification. Rock physics models quantitatively linked the elastic properties to variations of CO_2 saturation, lithology, and cement content. We modeled velocity and density logs with different fluid compositions. With seismic properties from to these different fluid compositions, we computed (1) AVA responses through Monte Carlo simulations and (2) probability density functions for statistical classification. Rock physics modeling indicated that the upper reservoir is a cemented sandstone and the lower portion a poorly to well sorted mixed lithology sandstone. Consequently, AVA illustrated that the stiff reservoir masked the seismic response due to fluid changes. Statistical classification differentiated between CO_2 and brine, with the ratio of compressional to shear wave velocity (Vp/Vs) used as a discerning parameter. Accordingly, these seismic-based tools, applied to relatively high-resolution data, showed the sensitivity of the elastic properties of the Cranfield reservoir to modeled changes of CO_2 saturation.

© 2013 Elsevier Ltd. All rights reserved.

1. Introduction

Sequestration of CO_2 within subsurface geologic formations is a potential technology to help minimize the amount of anthropogenic CO_2 released into the atmosphere. Recent studies have shown that brine reservoirs and depleted hydrocarbon reservoirs can store large quantities of CO_2. Various sites have shown this potential including the Sleipner (Ghaderi and Landrø, 2009), Weyburn (Ma and Morozov, 2010 and Verdon et al., 2010), and Otway projects (Dodds et al., 2009 and Urosevic et al., 2010). An important aspect of CO_2 sequestration is to monitor the volume and location of the fluid during and after injection to insure that the CO_2 remains in place. Geophysical techniques, in particular surface seismic methods, potentially can provide this monitoring capability over spatial areas not sampled by observation or injection well bores. When used in a time-lapse manner and linked quantitatively to the reservoir and fluid properties, seismic data potentially can be used to map the lateral extent of the injected fluid.

Quantitative seismic interpretation techniques have been used successfully to detect and characterize hydrocarbon reserves (e.g.,

Bosch et al., 2009; Russell et al., 2003; and Avseth and Skeji, 2011). These methods include fluid substitution and amplitude variation with angle (AVA), more commonly referred to as amplitude variations with offset (AVO), among others. Conventional fluid substitution work has focused primarily on modeling elastic properties and seismic data with different fluid-saturation scenarios to help distinguish between brine and hydrocarbon reservoirs (Das and Batzle, 2008; Artola and Alvarado, 2006). Signatures of AVA have proven useful in identifying natural gas and have been organized into different classes (Rutherford and Williams, 1989; Castagna et al., 1998; and Simm et al., 2000). Although these methods are useful for analyzing the fluid response of seismic data, injected CO_2 has very different physical properties than do hydrocarbons when contained within reservoirs. Accordingly, it is quite important to understand how sequestered CO_2 affects the elastic parameters of reservoirs into which it is injected. Our work here assesses the sensitivity of the elastic properties of the Cranfield reservoir to changes in CO_2 saturation using several quantitative seismic-based techniques.

Geophysical research pertaining to CO_2 injection and monitoring includes a wide range of topics. Siggins et al. (2010) compared laboratory ultrasonic velocities of CO_2-saturated core plugs to saturated synthetic sandstones from the Otway project for a wide range of pore pressures. This work concluded that replacing methane in the gas cap with CO_2 may not be noticeable from surface seismic measurements. However, replacing brine in a formation with CO_2

* Corresponding author. Tel.: +1 415 412 8649; fax: +1 512 471 5585.
  E-mail addresses: rwirkuscarter@gmail.com (R.W. Carter),
Kyle.spikes@jsg.utexas.edu (K.T. Spikes).
  [1] Tel.: +1 512 471 7674.

should produce a change in impedance that is measurable with surface seismic techniques. Additionally, high-frequency velocity measurements of CO_2-saturated core plugs from the Cranfield F-1 well were examined under a range of confining pressures (Joy, 2011). Joy (2011) found that the elastic wave velocities were approximately linearly proportional to the differential pressure of the sample. In addition changes in the pore structure and the cementation of the samples resulted from injecting brine containing dissolved CO_2. Lumley (2010) examined the feasibility of time-lapse seismic monitoring of CO_2 saturation by looking at the fluid properties of CO_2 as a function of temperature, pressure and saturation. The same study also helped to bridge the scale gap between laboratory-scale experiments and field-scale studies. This work concluded that the challenges to time-lapse monitoring of CO_2 include repeatability, CO_2–rock interactions, *in situ* CO_2 properties, pressure changes, and non-linear and non-unique responses of CO_2 to seismic waves.

Research has been completed that focuses on CO_2 monitoring and detection involving surface seismic data. Ghaderi and Landrø (2009) examined time-lapse amplitude and travel time shifts to estimate thickness and velocity changes in the Sleipner field. They found that when combined, 4-D amplitude and time shifts could be used to discriminate between changes in thickness and velocity changes in CO_2 layers in sand beds. Chadwick et al. (2010) quantitatively analyzed multiple vintages of data from the Sleipner field and applied a prestack stratigraphic inversion algorithm and compared it to poststack inversion methods. Prestack inversion better characterized thin intra-reservoir mudstone and sand layers compared to using poststack inversion. More recently, Daley et al. (2011) compared modeled and measured cross-well seismic data to model properties of an injected CO_2 plume at the Frio-II project and generated updated flow models from the relatively high-resolution cross-well seismic observations.

The study presented here combines rock physics modeling, fluid substitution, amplitude variations with angle (AVA), and statistical classification to differentiate between brine- and CO_2-saturated zones in the Cranfield reservoir located in Cranfield, MS. Rock physics modeling related the reservoir zone to lithology, porosity, and cement content to elastic parameters. We employed Gassmann (1951) fluid substitution to model the reservoir using multiple fluid mixing schemes and fluid compositions. For the AVA analysis, we modeled a shale-sandstone interface. The underlying sandstone was varied according to the fluid-substitution modeling, which allowed us to analyze the angle-dependent reflectivity as a function of saturation. The classification scheme compared modeled data to pairs of probability density functions (PDFs) to determine which class had the highest probability at the data location. Importantly, the method of fluid mixing and the corresponding ratio of compressional wave velocity to shear wave velocity (Vp/Vs) played important roles in the classification.

2. Cranfield background

The Cranfield study area consists of a sandstone reservoir of the Lower Tuscaloosa Formation, dated as Upper Cretaceous. The reservoir has porosity of about 20% and permeabilites in the range of 0.1–1000 millidarcies (Lu et al., 2012). Regionally the reservoir and seals are part of a sequence of sands and shales that are found in the Late Cretaceous Tuscaloosa Groups. A salt body underlies the entire complex, whose buoyant rising forced a local anticline. A large regional seal of marine shale and mudstone exists in the Middle Tuscaloosa Formation (Lu et al., 2012).

The Cranfield Field reservoir was discovered in 1943 and subsequently abandoned in 1966. The site was selected as a location for enhanced oil recovery (EOR) using CO_2 injection (Lu et al., 2012) due
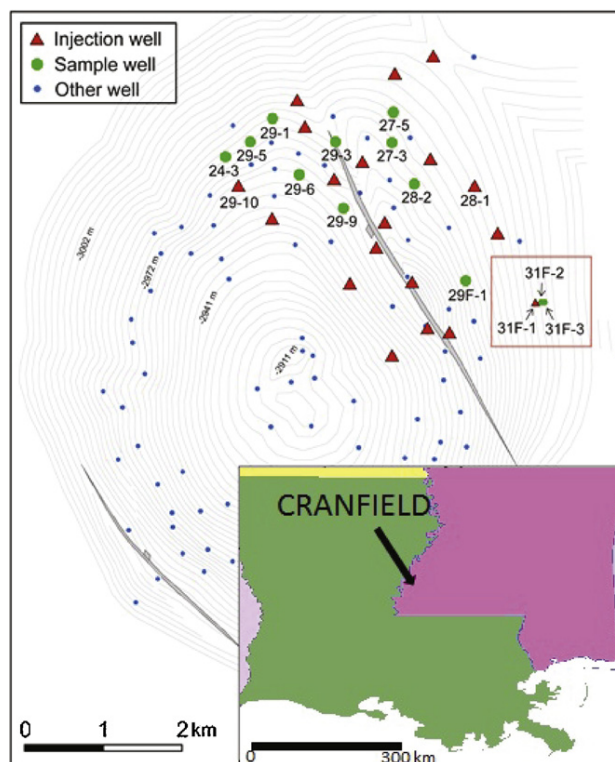
Fig. 1. The entire Cranfield site. Data for this project came from the DAS (red box). The DAS contains one injection well, 31F-1 (F-1), and two monitoring wells, 31F-2 (F-2) and 31F-3 (F-3). (For interpretation of the references to color in this figure legend, the reader is referred to the web version of the article.)
Modified from Lu et al. (2012).

to regional infrastructure, regionally available CO_2, and the high potential of economical, enhanced oil and gas production. The Gulf Coast Carbon Center of the Bureau of Economic Geology at the University of Texas at Austin is working in conjunction with both the Southeast Regional Carbon Sequestration Partnership and the field operator on the project (Lu et al., 2012). Over the entire field, the operator has injected over 3.4 million tons of CO_2 since the start of injection in July 2008. Data for this project comes from the 1 km^2 Detail Area Study (DAS), outlined in red in Fig. 1. The DAS consists of one injection well and two down dip monitoring wells (CFU 31#F1, 2, and 3, respectively). Injection rates at CFU 31#F1 (F-1) ranged from 200 to 500 tons per day during injection.

Well log data from CFU 31#F2 (F-2) was used for the work presented here. Well F-2 is located approximately 69 m down dip from the injection well F-1. Selected logs from the well F-2, acquired before injection, are shown in Fig. 2. Panels a, b, and c show Vp, Vs, and gamma ray logs, respectively. These logs contain the reservoir and shales above and below the reservoir. The blue line shows shales, the red corresponds to the upper reservoir zone from about 3183 to 3194 m, and the green overlay indicates the lower reservoir zone at approximately 3196–3200 m. The increase in the gamma ray count at about 3186 m indicates that a local shale layer divides the upper and lower reservoir intervals and is indicated in blue at that depth in Fig. 2.

3. Theory and methods

This study was a multi-step procedure that integrated rock physics modeling, fluid substitution, AVA, and statistical classification. Rock physics modeling linked reservoir properties to elastic
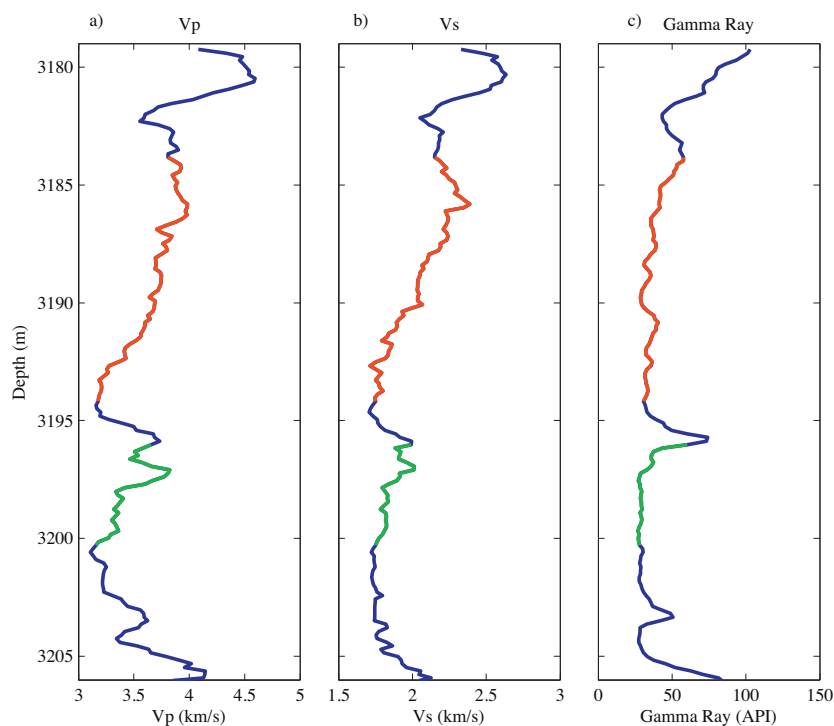
Fig. 2. Data from the monitoring well F-2, including (a) P-wave velocity, (b) S-wave velocity, and (c) gamma ray count. The red line shows the shallower reservoir zone, which extends from about 3184 to 3194 m, and the green line shows the deeper reservoir zone, which extends from about 3195 to 3200 m, and blue indicates shale. The local shale layer that divides the two reservoir zones is apparent from the increase in the gamma ray count between 3194 and 3197 m.

parameters. The fluid substitution showed the sensitivity of the reservoir elastic properties to saturation changes. Closely linked to the fluid substitution was the AVA analysis, which examined the sensitivity of the seismic response across the interface to fluid saturation variations. Statistical classification was performed on the results from the fluid substitution. The results from the statistical classification indicated which combinations of elastic properties within the reservoir interval provided the best discrimination among different CO_2–brine mixtures.

3.1. Rock physics modeling

Rock physics is the study of the relationships between reservoir properties such as porosity, lithology, pore fluid, and cementation (among others) and the elastic properties (P- and S-wave velocities or elastic moduli). Numerical, analytical, or empirically derived rock physics models transform reservoir properties to the elastic properties. Many models exist, but only a select few typically are applicable for a given reservoir. For this study we divided the Cranfield reservoir into two layers based on the gamma ray and velocity logs. For the shallower portion of the reservoir we used a contact-theory model. For the deeper portion of the reservoir, a model based on the Hashin and Shtrikman (1963) bounds was used.

Contact-theory models are derived from Hertz–Mindlin theory (Mindlin, 1949), which states that the stiffness and resistance to shear of a pack of uniform grains is a function of the Poisson's ratio of the grains, the friction between the grains, the pressure exerted on the grains, and the number of grain contacts. Modified Hashin–Shtrikman bounds provide interpolated elastic moduli (obtained from Hertz–Mindlin) values between zero porosity and a critical porosity value. The critical porosity is a transition point from a fluid- to grain-supported system (Avseth et al., 2005). Some contact-theory models (Dvorkin and Nur, 1996 and Avseth et al., 2000) allow for the inclusion of cement at grain contacts, but at

the expense of modeling pressure. The upper portion of the Cranfield reservoir consists of cemented sandstone (Lu et al., 2012), which makes the cemented sandstone contact-theory model the most appropriate. The contact cement model treats the rock as a package of uniform spherical grains with a single bulk and shear moduli. For mixed mineral situations composite or average elastic moduli must be calculated for the grains. In this model, cement can be deposited in two ways (Fig. 3a). First, cement can form along grain contacts (dark blue line); second, it can be deposited evenly around the grain surface (light blue line). For both methods, as cement volume increases, porosity of the sand pack decreases, and the overall stiffness of the rock frame increases. For this study we used the cementation method corresponding to a uniform and concentric deposition of clay-based cement around the grains to model the portion of the Cranfield reservoir from 3184 to 3194 m. We used a clay-based cement comprised of a mixture of approximately 65% chamosite and 35% kaolinite, which matches the compositional estimates (Lu et al., 2012). The contact cement model, however, is not valid for all porosity ranges between zero porosity and critical porosity. The model is valid for, at most, 20% cement, a range in this study, which extends for a range of porosities of 0.17–0.37.

The lower interval of the reservoir, 3195–3200 m, is interpreted to be a sandstone with poor to well sorted variations. To model this sorting trend, we implemented a theoretical bound, namely the lower modified Hashin–Shtrikman bound. Hashin–Shtrikman bounds are a way of mixing materials of different stiffnesses, either different mineral phases or a solid and a fluid. Examples of the Hashin–Shtrikman bounds and modified bounds are shown in Fig. 3b. The upper bound (solid red line) represents the solid material coating a spherical core of fluid. The lower bound (solid blue line) represents the reverse situation, in which the fluid concentrically coats the mineral grain. These bounds correspond to a mixture of quartz and brine. The two lines meet at the zero porosity mineral point (upper left) and at the 100% porosity point (lower
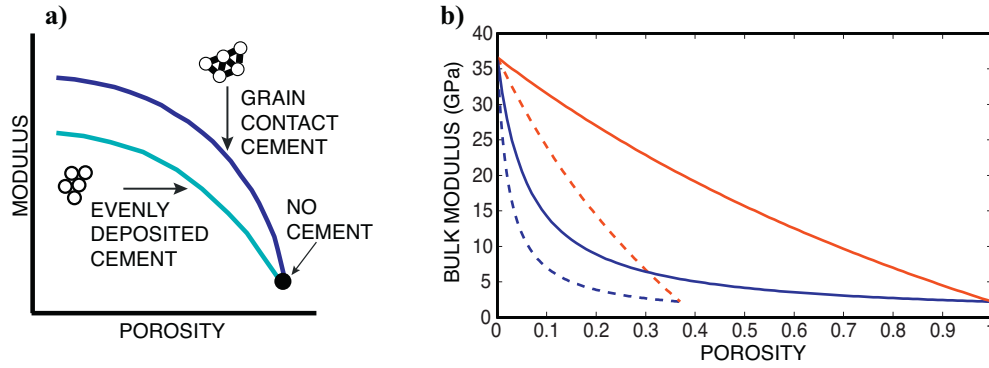
Fig. 3. Panel a shows a schematic of the contact cement model. Cement can be deposited concentrically around the grain following the lower path on the graph or only at grain contacts, following the upper line on the graph. As cementation increases, porosity decreases, and the elastic moduli (bulk and shear moduli) increase. Panel b shows Hashin–Shtrikman (solid) and modified Hashin–Shtrikman (dashed) bounds. The Hashin–Shtrikman bounds describe mixing of two materials as an isotropic combination of concentric spheres. They are the narrowest set of theoretical bounds for mixing two materials in terms of elasticity. The lower modified bound can be used to represent a sorting trend. The high porosity point is based on critical porosity, which is the maximum porosity that can be achieved while still having all grains in contact with other grains. This high porosity point represents a well-sorted mixture with deteriorating sorting as porosity decreases.

right). Modified Hashin–Shtrikman bounds (dashed lines Fig. 3b) are Hashin–Shtrikman bounds normalized to a critical porosity value. These bounds can be used to model velocities of unconsolidated sediments at depth (e.g., Blangy et al., 1993), where critical porosity is the highest possible porosity when grains are in contact with other grains. Loosely consolidated grains, with porosity greater than the critical porosity, tend to behave as if in a suspension and do not show significant changes in elastic moduli with respect to relatively large changes in porosity (Avseth et al., 2005). A lower modified Hashin–Shtrikman bound at porosity below critical porosity can also provides a heuristic approach to interpret sorting trends (Avseth et al., 2005). The interpretation is that low porosity represents poorly sorted material with a range of grain sizes partially filling the pore space between the larger grains. High porosity represents well-sorted material, with open pore space between equivalently sized grains. To fit this bound to data, a zero porosity moduli is chosen to represent the solid mineral grain, and arbitrary moduli values are selected to represent the critical porosity end point of the bound. The velocity or modulus at the critical porosity end point of the bound is used to fit the bound to the data, but it has no physical relation to either the grains or the fluid in the mixture.

3.2. Fluid substitution

Fluid substitution provides a way to calculate the bulk modulus of a porous rock saturated with any known pore fluid. The Biot–Gassmann equations (Gassmann, 1951; Biot, 1956) provide the basis for this method. Eq. (1) relates the different bulk moduli of the rock under examination, and Eq. (2) demonstrates the assumption that the shear moduli are equivalent in the saturated and dry cases.

$$\frac{K_{dry}}{K_0 - K_{sat}} = \frac{K_{dry}}{K_0 - K_{dry}} + \frac{K_{fl}}{\phi(K_0 - K_{fl})} \tag{1}$$

$$\frac{1}{\mu_{dry}} = \frac{1}{\mu_{sat}} \tag{2}$$

In these equations, K_{dry} is the dry rock bulk modulus, K_{sat} is the saturated rock bulk modulus, K_0 is the bulk modulus of the mineral phase of the rock, and K_{fl} is the bulk modulus of the pore fluid. These equations result in accurate calculations, provided that the following three criteria are met. A homogeneous mineral modulus exists, the rock is isotropic, and low frequency is used to maintain pore-pressure equilibrium (Gassmann, 1951).

Eqs. (3) and (4) relate Eqs. (1) and (2) to the compressional (Vp) and the shear wave (Vs) velocities. For the fluid substitution portion of this study, reformulations of Eq. (1) were used, solving for K_{dry} (Eq. (5)) and K_{sat} (Eq. (6)).

$$Vp = \sqrt{\frac{K + (4/3)\mu}{\rho}} \tag{3}$$

$$Vs = \sqrt{\frac{\mu}{\rho}} \tag{4}$$

$$K_{dry} = \frac{K_{sat}(\phi K_0/K_{fl} + 1 - \phi) - K_0}{(\phi K_0/K_{fl} + K_{sat}/K_0 - 1 - \phi)} \tag{5}$$

$$K_{sat} = \frac{\phi(1/K_0 - 1/K_{fl}) + 1/K_0 - 1/K_{dry}}{(\phi/K_{dry})(1/K_0 - 1/K_{fl}) + (1/K_0)(1/K_0 - 1/K_{dry})} \tag{6}$$

To determine the fluid substituted K_{sat} value corresponding to a particular fluid, the stiffness of that fluid (K_{fl}) must be provided. Moduli of fluid mixtures can be calculated using the Voigt (1907) bound, representing patchy saturation, or the Reuss (1929) bound, representing uniform saturation (Knight and Nolen-Hoeksema, 1990). The Voigt bound is an arithmetic average of the moduli of two or more fluids and results in the stiffest possible mixing of the constituent fluids. The Reuss bound is a harmonic average of the fluid moduli and represents the softest way of mixing two or more fluids. Table 2 contains the moduli and density of the fluids and minerals used in this study.

The effective grain moduli (K_0) were calculated from an average of the Voigt and Ruess bounds for the minerals percentages shown in the first row in Table 1. The mineral moduli for the clay used in this study was a mixture of moduli of two different clay varieties taken from the literature. We calculated our clay moduli based on a mixture of 65% chamosite and 35% kaolinite. This is approximately the same fractions of clay minerals as presented in Lu et al. (2012)

Table 1
Percentages of minerals used in the contact cement models. The black line moduli for the mineral end point are 35 and 38 GPa for bulk and shear modulus, respectively, and this corresponds to the mineral composition of 80% quartz and 20% clay. The moduli for the critical porosity end point (porosity equal to 0.37) are 13.4 and 0.8 GPa for bulk and shear modulus, respectively.

Line	Quartz %	Clay %	Feldspar %	Muscovite %	Calcite %
Red	60	20	20	0	0
Green	70	10	10	7	3
Blue	80	5	5	5	5

for the Cranfield reservoir interval. Bulk moduli for chamosite came from Theye et al. (2003), and elastic parameters for kaolinite were taken from Woeber et al. (1963). Shear moduli were not measured in the Theye et al. (2003) study and were interpolated to maintain a similar relationship to bulk moduli as 'Gulf Clays' (i.e., Tosaya, 1982 and Blangy, 1992). The properties for CO_2 were interpolated from measured values (Wang, 2000) for a pore pressure of 30 MPa and a temperature of approximately 120 °C. This temperature and pressure combination causes the CO_2 to be in the supercritical phase. These were approximate reservoir conditions during injection (Lu et al., 2012). Values of K_{fl} corresponding to a range of brine and CO_2 percentages were used in the Gassmann equations. These included 100% brine and 100% CO_2 as well as intermediate compositions of 25, 50, and 75% CO_2, where the remaining proportion was brine in each case.

3.3. Amplitude variations with angle

Signatures of seismic amplitude variations with angle (AVA) have proven useful in differentiating fluid compositions (Rutherford and Williams, 1989; Castagna et al., 1998; and Simm et al., 2000). The Knott–Zoeppritz (Knott, 1899; Zoeppritz, 1919) equations describe how reflection coefficients change as a function of incidence angle for a two-layer problem. These original equations have since been modified and linearized as in Shuey (1985) and Aki and Richards (1980). Effects of AVA are a function of P-impedance (Ip), S-impedance (Is), and density across the interface of the two-layer or half-space model. At relatively small angles (0–10°), seismic amplitude is primarily a function of Ip. As the angle of incidence increases, the seismic amplitude becomes primarily a function of Is and density.

Each layer in the AVA model must be assigned a value of Vp, Vs, and density. These property values and density can come from different data types including core plug velocity measurements, but they most often come from averages of well log sonic and density measurements. The AVA result from a single set of velocities and density measurements is a single set of angle-dependent reflection coefficients. However, using averages for each layer does not account for variations within each individual layer to be represented in the outcome. Furthermore, it does not provide a reliable representation of the interface between the two layers because the difference in average values of two layers rarely represents the change in properties across an interface (Bosch et al., 2007). To account for the variability in the elastic properties, we used a Monte Carlo simulation to estimate the range of reflection coefficients that could be expected between the overlying shale and the reservoir. This technique returns a range of possible outcomes and allows for the probability of each outcome to be determined. This range of outcomes can be related to variations in the rock properties such as fluid saturation.

The Monte Carlo simulation was performed on well data scaled up to the seismic scale using the Backus (1962) average. The Backus (1962) average is the long wavelength approximation of a seismic wave propagating though a series of thin layers. When applied to log data as a running average over a specific window size, it provides the seismic velocity at the resolution expected from surface seismic data. We used specific window sizes so that the frequency of the upscaled data was similar to the dominant frequency of the seismic (20–50 Hz) and 3D VSP (20–90 Hz) data acquired at the Cranfield site. For the Monte Carlo simulation we also varied the location of the interface between the shale layer and the reservoir over a range of 6 m. Shifting the shale–reservoir interface was necessary because of the lack of a definitive and resolvable interface in the upscaled data. Two hundred simulations were run for each of the 20 different half-space models generated by shifting the shale–reservoir interface. In total, 4000 simulations were computed. The same number

(4000) of simulations were computed for the five fluid compositions mentioned in the fluid substitution step. Additionally, even though it is understood that the injected CO_2 is primarily confined to the high permeability intervals of the reservoir (Tuscaloosa Sand D in Lu et al. (2012)) we chose to saturate uniformly the entire reservoir layer to maximize the number of available data points used for this simulation. With the entire reservoir saturated, the number of available data points was sufficient that the simulation would be able to model the full range of variability between the reservoir and the overlying shale interface. Decreasing the number of available data points from the reservoir for the simulation, as would happen if we only modeled CO_2 saturation in a thin subset of the reservoir, would remove a significant amount of the inherent variability that is present in the reservoir zone from the simulation. This saturation profile uniformly increased the likelihood of the simulation showing variations in response due to fluid composition.

Each simulation included a random selection of a single depth from both the overlying shale zone and from the reservoir zone. The AVA response was computed from the velocities and densities associated with each selected depth. We ran the simulations for each different fluid composition of 0, 25, 50, 75, and 100% CO_2 and for the two different schemes of fluid mixing (Voigt and Reuss). We calculated the AVA response using the full Zoeppritz equations for incidence angles 0–30°. For each fluid composition, a bivariate PDF was calculated from the 4000 simulations. Those PDFs indicate the probability of a reflection coefficient occurring at a given angle of incidence for a certain pore–fluid composition.

3.4. Classification

Synthetic velocity and density logs calculated using fluid substitution were used to generate crossplots for various combinations of Vp, Vs, Ip, Is, Vp/Vs and density. We chose these various pairs of elastic properties because they represented a wide range of parameter combinations and because they can be extracted from well logs and from offset surface seismic and VSP data. A bivariate PDF was computed for each crossplot. These PDFs were used to classify the data in terms of pore fluids.

An important element of this procedure was to determine the classification success rate for each pore fluid, where each different pore fluid corresponds to a class. For this study, the success rate was defined as the number of correctly classified points divided by the known number of points in that class. Classification success rates were calculated by mapping both the measured well log and modeled data back to the their respective bivariate PDFs and a comparison PDF from a different fluid class. Each data point was mapped to the PDF that showed the highest probability at the location of the data point.

Three parameter combinations showed the highest success rates for all different fluid combinations. These combinations were Vp/Vs to Ip, Vp/Vs to Vs and Vp/Vs to Vp. The fluid compositions compared were 0% and 100%, 0% and 25%, 0% and 50%, and 0% and 75% CO_2. The different CO_2 concentrations were also tested against measured well log data. When an equal probability occurred of a data point belonging to both classes, the data point was mapped to both. However, if probability in both PDFs was zero, the data point was mapped to neither class. These two situations were present in each classification procedure and affected the success rates.

4. Results

4.1. Rock-physics modeling

Modeled lines from the contact cement model (Dvorkin and Nur, 1996) can be seen in Fig. 4 to represent the depth range
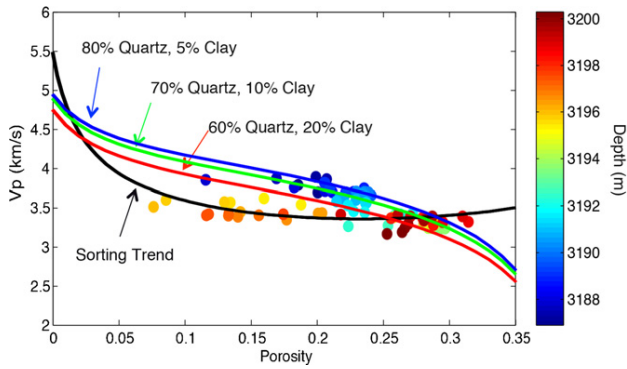
Fig. 4. Vp versus total porosity (points) from the reservoir zone, colored by depth. Blue, green, and red lines are from the contact cement model for different rock frame compositions. Only quartz and clay contents are displayed for clarity. The exact composition of each line is shown in Table 1, and component moduli are shown in Table 2. Velocity in these lines decreases as quartz content decreases and clay content increases. The black line is a modified lower Hashin–Shtrikman bound that represents a sorting trend. In terms of sorting, the lower portion (3195–3200 m) is well sorted, and the upper portion is poorly sorted. The zero porosity end member of the sorting trend has a composition of 80% quartz and 20% clay. Velocity at the critical porosity end member (porosity equal to 0.37) was selected to fit the data and is calculated from a bulk and shear modulus of 13.4 and 0.8 GPa, respectively.

3184–3194 m. The red, green, and blue lines represent different modeled grain compositions. Complete mineral compositions for the red, green, and blue lines are in Table 1, and the mineral moduli used are in Table 2. The cement moduli used in the contact cement model are the same as those listed for clay in Table 2 (a combination of chamosite and kaolinite). The calibrated models are important because they will enable modeling of the reservoir away from the control well by varying the model parameters in a geologically plausible manner. Altering porosity, cement, and mineral composition in the model can be a way to characterize reservoir parameter variations in between wells using surface seismic and/or 3D VSP data.

Mineral compositions used in the modeling were based on studies of core samples from the F-2 well. Those samples indicated that the mineral composition of the reservoir consisted of 60–80% quartz, 10–20% clay, and 10–20% feldspar, with the remainder composed of small percentages of muscovite, calcite, and other minerals (Kordi et al., 2010). Variations on these compositions provided a range of effective mineral moduli. For the deeper portion of the reservoir (3196–3200 m), a modified Hashin–Shtrikman lower bound was used (Fig. 4, black line). This model provides an interpretation for the deeper reservoir interval as well sorted trending

Table 2
Brine, CO_2, and mineral parameters used for fluid substitution analysis and rock physics modeling. Clay moduli and density was calculated from approximately 65% chamosite and 35% kaolinite.

Fluid/mineral	Density (g/cm^3)	Bulk modulus (GPa)	Shear modulus (GPa)
Brine	1.045	2.2	0
CO_2	0.591	0.0983	0
Quartz	2.65	36	45
Clay	2.8	30.5	10.5
Chamosite	3.3	47.2	15.4[a]
Kaolinite	1.58	1.5	1.4
Feldspar	2.63	55	28
Muscovite	2.79	58	35
Calcite	2.71	71	36

[a] A measured shear value for chamosite was not available so a shear moduli was interpolated to give the final clay mixture a bulk to shear modulus ratio approximately the same as that measured for 'Gulf Clays'.

upward to poorly sorted with the same lithology. Correspondingly, the porosity is highest for the well sorted part and lowest where the sorting deteriorates. We offer no interpretation for the modified lower Hashin–Shtrikman bound other than representing a possible sorting trend. For this interpretation, we chose the zero porosity end member to have a mineral composition of 80% quartz and 20% clay with a bulk and shear modulus of 35 and 38 GPa, respectively. This model was constrained to a two-mineral approximation of the reservoir composition in order to not over fit the data trend. For the critical porosity end point (porosity is equal to 0.37), a bulk modulus and shear modulus of 13.4 and 0.8 GPa, respectively, were used. This interpretation of a sorting trend is consistent with the gamma ray log for this portion of the reservoir (Fig. 2c) which is relatively uniform. This is interpreted to indicate a uniform lithology through this region with the change in velocity present in the acoustic velocity (Fig. 2a) being attributed to sorting.

4.2. Fluid substitution

Fig. 5 contains measured velocity logs and modeled logs calculated from fluid substitution with different pore fluids. In all panels of Fig. 5, the blue curve represents a 100% brine-saturated rock. The green, red, cyan, and magenta lines show the modeled data for 25, 50, 75 and 100% CO_2, respectively. The thin black line is the measured log data. Velocity curves from the reservoir interval, with fluid moduli calculated from the Voigt bound, are shown in Fig. 5a. The lines in Fig. 5a show a uniform spacing between different fluid compositions, corresponding to the linearity of the Voigt average. Fig. 5b shows the velocity curves for the same reservoir interval using the Reuss bound for the fluid moduli for the different fluid compositions. These lines show a large decrease in velocity with a small amount of dissolved CO_2, but very little difference exists among the lines with CO_2 included. End member (0 or 100% CO_2) velocity curves were independent of how the fluids were mixed, as expected. Fig. 5c is a plot of Vs for different CO_2 saturations. Shear velocity increases slightly with increasing CO_2 saturation due to the inverse relationship with bulk density.

4.3. AVA

Angle-dependent reflectivity was calculated using the full Zoeppritz equations, for incidence angles of 0–30°. Four thousand simulations were computed for each fluid composition (0, 25, 50, 75, and 100% CO_2). These correspond to Fig. 6a–e, respectively. Additionally, the same number of simulations was run based on the measured log data (Fig. 6f). All the AVA plots in Fig. 6 are conditional PDFs of reflection coefficients for any given angle of incidence. The elastic properties used to populate these AVA models came from the modeled and measured logs in Fig. 5a. Warm colors represent a high probability of generating a given reflection coefficient at a given angle, whereas cool colors indicate a low probability. The black line represents the mean curve for each fluid scenario.

The increase of reflection coefficient with increasing angle is consistent with a shale over sand sequence. In each case, high probability regions correspond to negative intercepts and less negative to zero values at 30°. All panels of Fig. 6 show a significant degree of similarity, due to the stiffness of the cemented sandstone reservoir, which minimizes the fluids effect on the seismic response in the simulation. PDFs corresponding to AVA simulations generated from the modeled well logs in Fig. 5b (not shown) were statistically equivalent to the PDFs corresponding to Fig. 5a.

4.4. Classification

The three elastic property combinations that resulted in the highest success rates for mapping the fluid classes were Vp/Vs–Ip
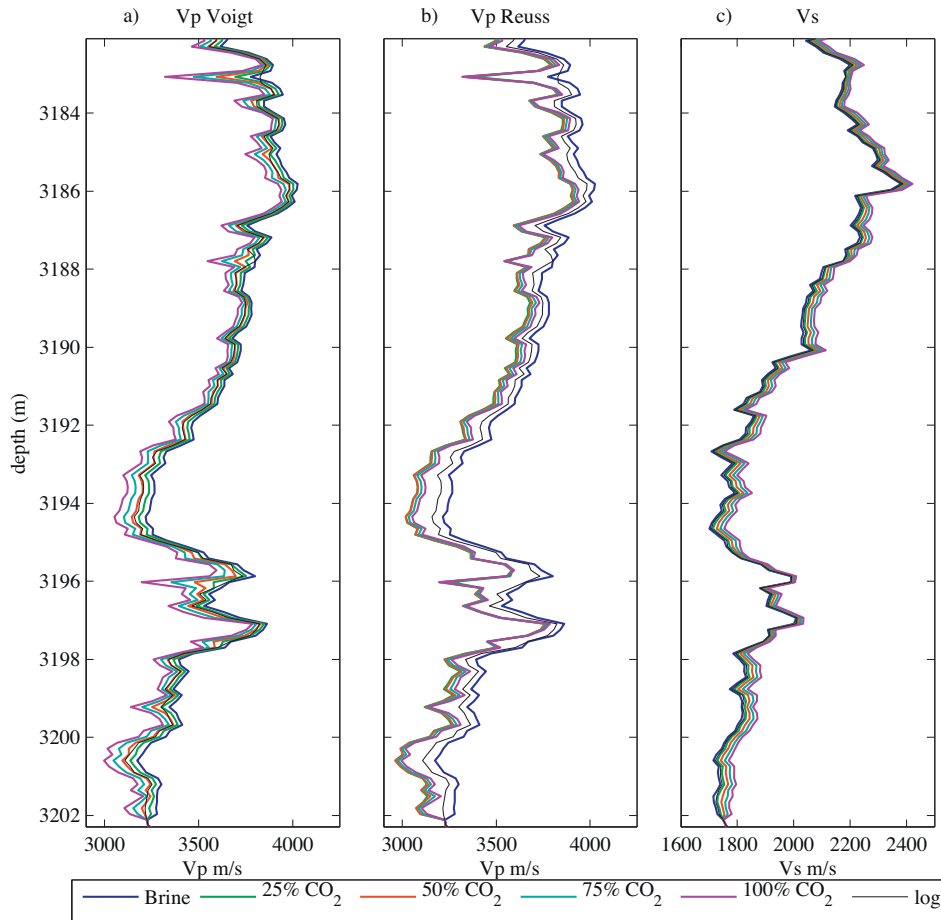
Fig. 5. Panel a shows the fluid substituted velocity curves with fluid moduli calculated from the Voigt average. Panel b shows the same, but the fluid moduli were calculated with the Reuss average. Panel c shows Vs data. In these graphs the blue, green, red, cyan, and magenta lines represent pure brine, 25, 50, 75 and 100% CO_2, respectively. The thin black line on all graphs is the measured log data included as a reference. The uniform spacing between different fluid compositions is because the Voigt average is linear (panel a). In panel b there is a large gap between the brine saturated curve and the curves containing partial or full CO_2 saturation because the Reuss average moduli change significantly at low CO_2 concentrations and remains nearly constant with increasing CO_2. In panel c, Vs increases with increasing gas saturation because of density.

(Fig. 7), Vp/Vs–Vs (Fig. 8) and Vp/Vs–Vp (Fig. 9). Bivariate PDFs were generated from these crossplots for each class. We examined the 100% CO_2 and 100% brine classes first because they corresponded to the largest differences in velocity and density. The expectation was that the highest classification success rate would occur for these two classes. Data points from each class were mapped to their respective PDFs to determine their success rates. Fig. 7a shows 100% CO_2 (blue) and 100% brine (green) data plotted by Vp/Vs as a function of Ip. Panels b and c show the PDFs generated from the CO_2 and brine data, respectively. Dark colors are areas of high probability, light colors are areas of low probability, and white are areas of zero probability. The numbers in panels b and c show the success rates for mapping to the fluid class of that panel, which were 0.72 when mapping 100% CO_2 data and 0.62 when mapping 100% brine data.

In Fig. 8a, Vs as a function of Vp/Vs was used to crossplot 100% CO_2 and 100% brine data, blue and green, respectively. The data in panel a was used to calculate the PDFs shown in panels b and c that correspond to 100% CO_2 and 100% brine data, respectively. Colors in Fig. 8a and b signify the range of probability from low (light) to high (dark). When classifying with this combination of parameters, the success rate for CO_2 data was 0.70, and the brine data gave a 0.70. The axes in Fig. 9 show Vp as a function of Vp/Vs. Data plotted in Fig. 9a corresponds to 100% CO_2 (blue) and 100% brine (green). The 100% CO_2 data was used to generate the PDF shown in Fig. 9b and

the 100% brine data was used to generate the PDF shown in Fig. 9c. When classifying with these parameters, the success rates were 0.68 for 100% CO_2 data and 0.73 for 100% brine data. Fig. 9a and b are colored to the same scheme as their counterparts in Figs. 7 and 8.

Results from classifying the intermediate fluid compositions generated lower success rates than did classifying the end members, as expected. Table 3 shows the results of mapping intermediate fluid compositions against brine and against measured log data. In Table 3 the six columns of data represent the results of plotting 25, 50 and 75% CO_2 concentrations against measured data (columns 2 through 4) and against 100% brine (columns 5 through 7). Fluid moduli in Table 3 were calculated using the Reuss average.

Table 4 shows the same data as Table 3 except that the fluid parameters were calculated using the Voigt average. The results show, in general, an increase in the success rate with an increase in percent CO_2 for both methods of calculating fluid moduli. When using the Reuss average, slight increases occurred in success rates with increases in CO_2 percentage. However, success rates of data derived from the Voigt bounds displayed a larger increase in success rate with increasing CO_2 percentage compared to the respective class calculated with the Reuss bound. The highest success rate for either fluid modeling method corresponded to Vp against Vp/Vs ratio, with Vs against Vp/Vs showing a similar but slightly reduced success rate compared to Vp–Vp/Vs.
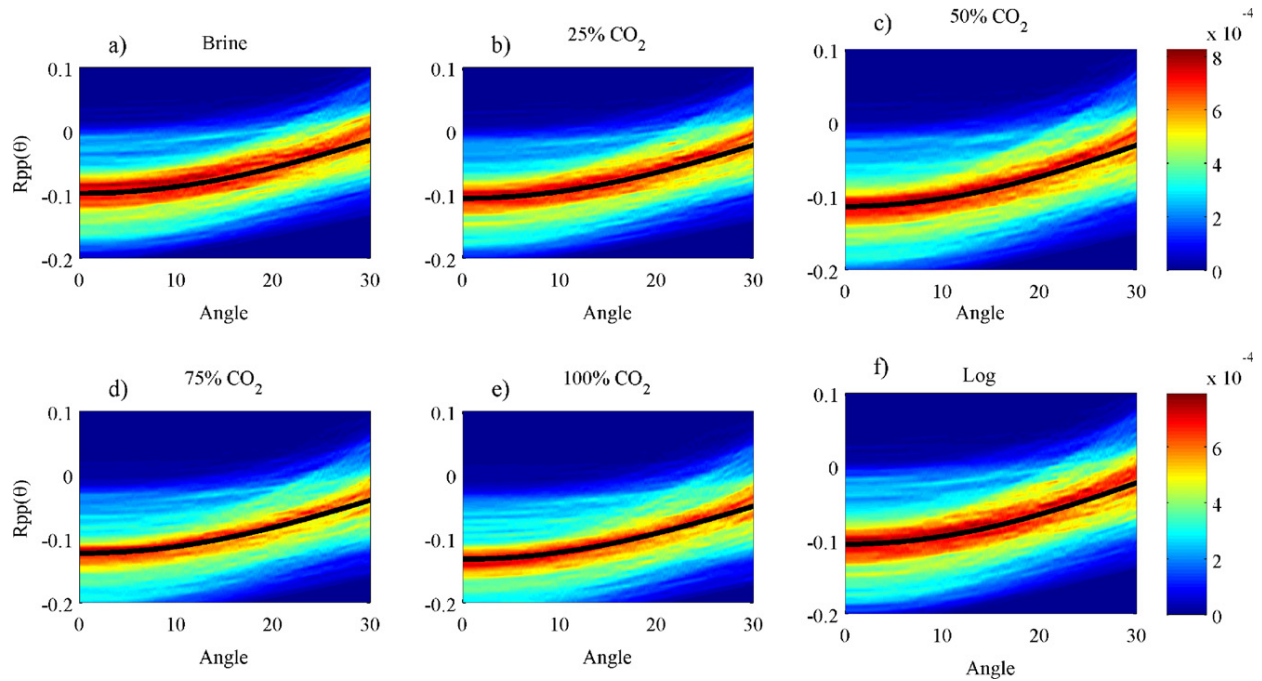
Fig. 6. Each panel shows a PDF from a Monte Carlo simulation with 4000 iterations of angle-dependent reflectivity for a sandstone–shale interface. Reflection coefficients are on the *y*-axis and angle of incidence on the *x*-axis. Warm colors indicate high probability density, and cool colors show low probability density. Plots a–e were computed with the lines from Fig. 5a. Plot f is generated from the measured log data. Minimal differences exist among the AVA probability plots for pure brine and pure CO_2 (a and e) or the intermediate compositions. (For interpretation of the references to color in this figure legend, the reader is referred to the web version of the article.)
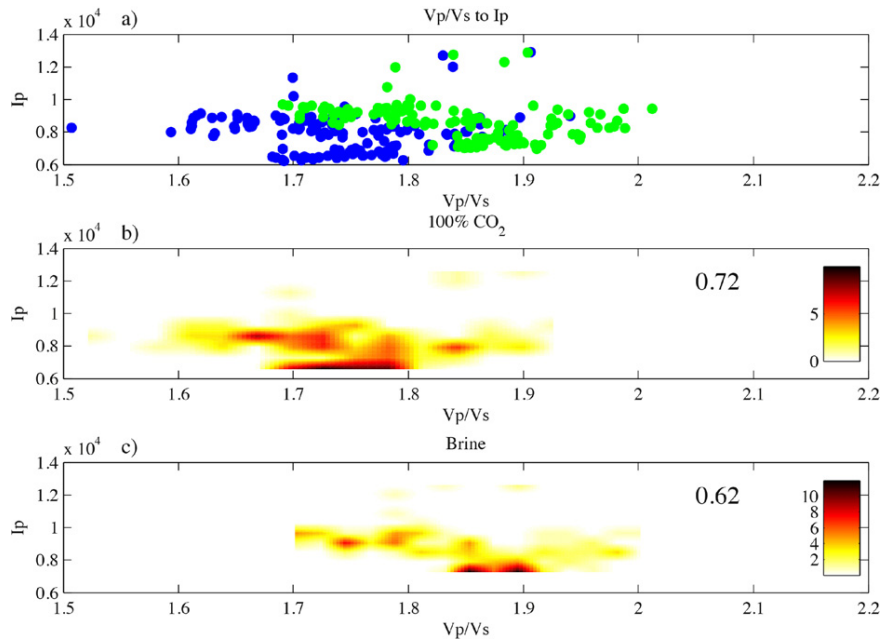
Fig. 7. (a) Ip as a function of Vp/Vs for 100% CO_2 (blue) and 100% brine (green). (b) and (c) show the bivariate PDFs computed for the data in (a), for the 100% CO_2 and the 100% brine data, respectively. For (b) and (c) black and red indicate areas of high probability density, whereas light yellow and white indicate areas of low probability or zero probability density. The number (0.72) on panel b is the success rate for classifying 100% CO_2 data to its PDF. In (c) 0.62 is the success rate for classifying 100% brine data to its corresponding PDF.

5. Discussion

Rock physics modeling for this study was useful in that it provided a way to correlate the mineral compositions provided by the petrography studies to mineral moduli that were needed for fluid substitution modeling and AVA analysis. Additionally,

the calibrated rock physics model showed that increasing quartz and decreasing clay content in the matrix can cause Vp and Vs to increase. Increases in cement concentration can have a similar effect. The calibrated models that link lithology, porosity, and cementation to seismic velocity will be useful for providing constraints on those same parameters away from well control.
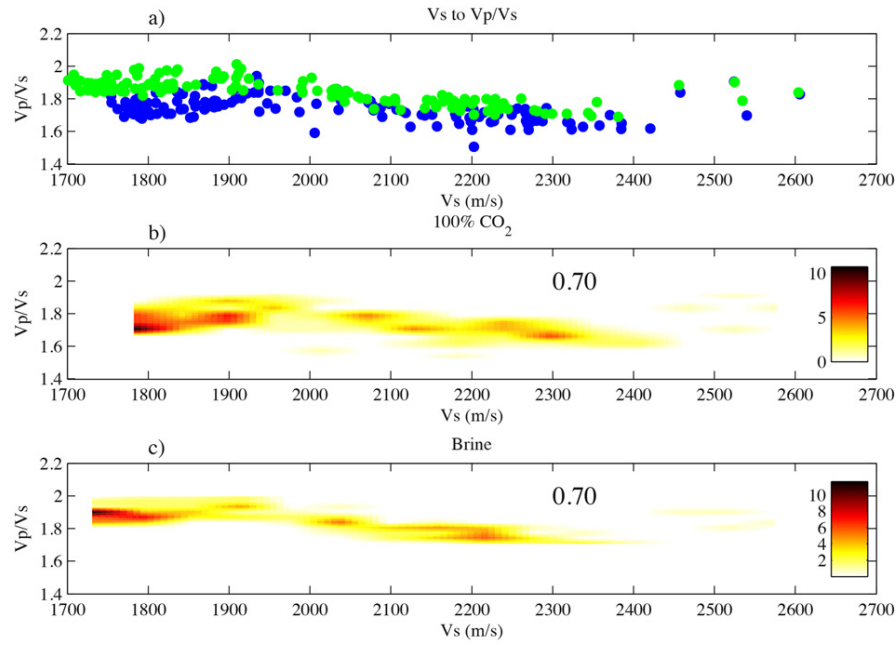
Fig. 8. (a) Modeled data for 100% CO_2 (blue) and 100% brine (green) for Vp/Vs as a function of Vs. (b) The bivariate PDF generated from the 100% CO_2 data points, and (c) contains the bivariate PDF generated from the 100% brine data. Color in (b) and (c) range from black and red (high probability density) to light yellow and white (low or zero probability density). The numbers in black on panels b and c indicate the success rate of classifying data back to its PDF.
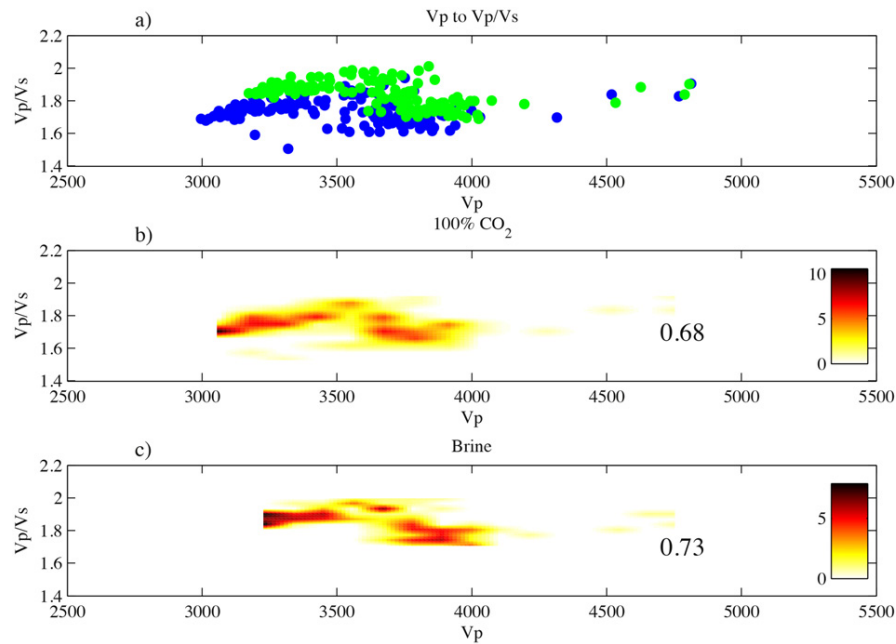
Fig. 9. This figure is Vp/Vs as a function of Vp. (a) Blue and green data representing 100% CO_2 and 100% brine, respectively. (b) and (c) The bivariate PDFs generated from the 100% CO_2 and 100% brine data from panel a. Black and red colors indicate high probability density. Light yellow and white indicate low probability density. Success rates for mapping 100% CO_2 and 100% brine are shown in panels b and c, respectively.

Table 3
Classification success rates for the intermediate fluid concentrations mapped to their respective PDFs for the three best performing crossplots from the study. Fluid properties were calculated from the Reuss average. The column headings indicate the two fluid classes being compared. For example, 25/log indicates that 25% CO_2 was being compared to log data, 25/0 indicates that 25% CO_2 data was being compared to 100% brine date. Values in the body of the table indicate the success rate of classifying the data correctly between the mixed fluid (first value) and either the log and or brine data (second value).

Crossplot	25/log	50/log	75/log	25/0	50/0	75/0
Vp/Vs to Ip	0.478/0.732	0.617/0.683	0.664/0.577	0.593/0.688	0.693/0.602	0.735/0.495
Vp/Vs to Vs	0.550/0.835	0.628/0.727	0.627/0.672	0.519/0.857	0.675/0.761	0.698/0.597
Vp/Vs to Vp	0.576/0.815	0.641/0.704	0.638/0.652	0.671/0.713	0.705/0.692	0.733/0.645

Table 4

The intermediate fluid concentrations classified to their respective PDFs for the three best performing crossplots from the study. Fluid properties were calculated from the Voigt average. Column headings refer to the fluid classes being compared with the first value indicating the CO_2 percentage and the second value being either log data or 100% brine data. Values indicate the success rate of classifying the data correctly between the mixed fluid (first value) and either the log and or brine data (second value).

Crossplot	25/log	50/log	75/log	25/0	50/0	75/0
Vp/Vs to Ip	0.322/0.577	0.440/0.642	0.522/0.672	0.505/0.447	0.621/0.514	0.636/0.611
Vs to Vp/Vs	0.459/0.537	0.458/0.606	0.492/0.811	0.385/0.692	0.631/0.878	0.549/0.833
Vp to Vp/Vs	0.385/0.611	0.445/0.630	0.496/0.748	0.491/0.487	0.626/0.624	0.646/0.684

Fluid composition and the mixing of fluid moduli played an important role in the velocity modeling. When the fluids were mixed using a patchy saturation model, a linear trend resulted in Vp with changes in CO_2 saturation. When the fluids were mixed uniformly, as is represented by the Reuss bound, little variation in velocity existed among concentrations of CO_2 of 25–100% (Fig. 6b). However, a substantial change in velocity occurred between 100% brine and 25% CO_2. This agrees with previous work that indicates that velocities depend on fluid saturations and on the way those fluids are distributed within the pore space (Mavko and Mukerji, 1998). This phenomenon is similar to the commonly recognized fizz-water problem characterized by a minimal difference in seismic responses between high and low gas content in brine. The consistency between the modeled Vs values is easily understood because only density affects Vs (Fig. 6c and Eq. (4)) as a function of fluid composition. Bulk density changes linearly with changes in CO_2 percent because it is calculated from a weighted average of fluid components and rock frame minerals.

A lack of variation in the AVA modeling due to fluid composition is evident in the results. All panels of Fig. 6 show very similar reflection coefficients at all angles. This lack of variation in the AVA responses can be explained by the stiffness of the rock frame in the upper reservoir, due to the cement content. The stiff frame restricts the sensitivity of the rock elastic properties to fluid changes (Castagna and Backus, 1993). Given the stiffness and relatively high velocities associated with the reservoir rock, we should expect small variations in the AVA response with a change in fluid composition. Additionally, the larger the contrast in the rock properties across an interface, the smaller the effect the fluid will have on the reflection coefficient (Stine, 2004). By shifting the interface in

this study we hoped to minimize this effect and mimic the upscaled interface as would be seen with surface seismic or VSP data. However, due to the internal stiffness of the reservoir we were still not able to attribute an AVA response to changes in fluid saturation. Given the lack of variation present in the AVA response due to fluid composition when the entire reservoir zone is saturated with CO_2, it is unlikely that given the resolution of seismic data it would be possible to detect vertical variation in the saturation due to permeability variations using this method.

Results from the classification scheme were encouraging because they showed a relatively high success rate when using Vp/Vs versus Ip, Vp, or Vs within the reservoir interval. These occurrences indicate that Vp/Vs is important and useful for characterizing and monitoring injected CO_2. This is because Vp/Vs effectively emphasizes the fluid-saturated bulk modulus while density cancels and shear modulus remains constant. Additionally, we showed that in general, as the difference between the fluid compositions increased, the classification success rate increased. The ability of Vp/Vs to discriminate between different fluids has been shown before in trying to differentiate between brine and hydrocarbons (e.g. Castagna and Backus, 1993).

When examining the scatter plots of the data and the bivariate PDFs (Figs. 7–9), sharp edges are present along the boundaries of the PDFs separating areas of high probability and zero probability. An example of this is Fig. 8b (Vp/Vs = 1.8 and Vs = 1780 m/s). This is an artifact of the binning used when computing the PDFs. It has the potential to have a small negative impact on successfully mapping data sets back to their respective classes. Fig. 10a shows the PDF for 100% CO_2 pore fluid, and Fig. 10b shows the PDF for 100% brine pore fluid. Black points in both panels are the data from which the
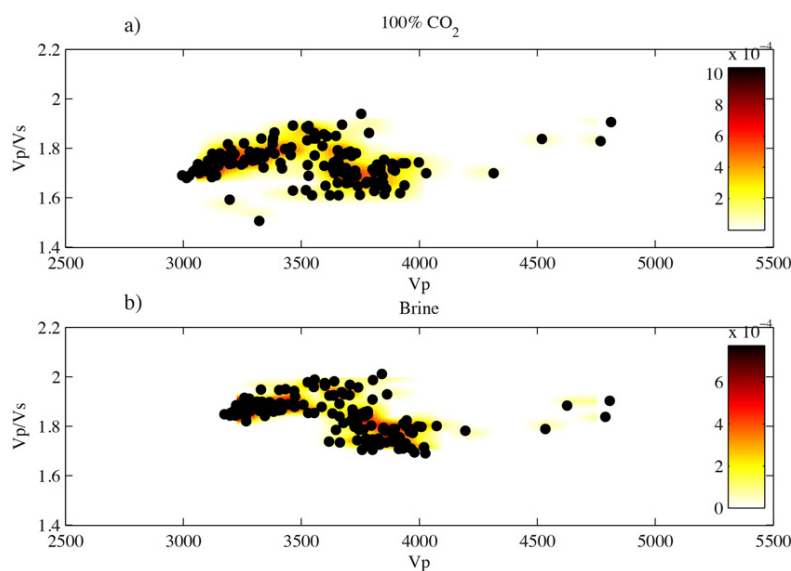

Fig. 10. Modeled data plotted atop its corresponding bivariate PDF. Panel a shows 100% CO_2 data and panel b shows 100% brine data. Red and black colors in these panels represent high probability density, whereas light yellow and white represent low and zero probability density. These plots illustrate that some high-density clusters of data points extend beyond the edges of the PDFs into areas of zero probability. In the classification scheme, these points were not mapped to any PDF, which lowered the success rate.

distributions were computed. Because of the binning procedure, some data points fall outside the boundaries of their respective PDFs. During the mapping routine, these data points were not assigned to either distribution. One way to minimize this effect in future studies would be to simulate statistically equivalent data points to increase the total number of data points used to compute the PDF. This could help to extend the range of the PDF and smooth the edges to avoid large numbers of data points from falling into zero probability regions, likely improving classification success rates.

6. Conclusions

This study showed that AVA may not be reliable when examining fluid substitution in the Cranfield reservoir because the rock frame is stiff. When looking at a shale–sandstone interface with a large impedance contrast, the reflection coefficient will not show significant changes with respect to changes in fluid composition. Because the changes in fluid composition do not significantly alter either the shear impedance or the density of the rock, the angle-dependent reflection coefficients will not show much variability with changes in fluid. The combination of these two factors works to minimize the change in AVA due to a change in fluid composition.

Fluid mixing laws can impact significantly the elastic properties of the fluid. When mixing two fluids that have very different elastic moduli, such as brine and supercritical CO_2, using the Reuss bound versus the Voigt bound, the change in effective moduli is more apparent at small percentages of supercritical fluid saturation than higher concentrations. Because shear moduli are fluid independent and density is computed as an arithmetic average, calculated Vs for a fluid-saturated rock does not change regardless of which method is used to calculate the fluid parameters. Accordingly, crossplots of Vp as a function of Vp/Vs and Vs as a function of Vp/Vs provide the best ability to discriminate between variations in fluid composition in a stiff rock frame. Although Vp/Vs cannot be used as a direct indicator of fluid composition, crossplots generated with it are useful for comparing modeled fluid substitution data to measured data. From these crossplots, PDFs can be generated to assess the change and the associated uncertainty for time-lapse studies.

This study showed the sensitivity of the elastic properties of the Cranfield reservoir to changes in CO_2 saturation through different quantitative seismic methods. We did this using relatively high resolution well log data. Although surface seismic data and 3D VSP data both are lower resolution than well log data, they provide areal coverage away from well control. Among the methods we examined, the classification scheme provided the most encouraging results. When we apply this to the surface data, we likely will use the same combinations of elastic properties used in the well log data procedure. Those elastic properties are the parameters most commonly extracted from seismic data. Classification of seismically derived elastic properties, calibrated to well data, should allow for characterizing fluid volume and location and assessing the associated uncertainty.

References

Aki, K., Richards, P.G., 1980. Quantitative Seismology: Theory and Methods. W.H. Freeman and Co, San Francisco.

Artola, F., Alvarado, V., 2006. Sensitivity analysis of Gassmann's fluid substitution equations: some implications in feasibility studies of time-lapse seismic reservoir monitoring. Journal of Applied Geophysics 59, 47–52.

Avseth, P., Dvorkin, J., Mavko, G., Rykkje, J., 2000. Rock physics diagnostics of North Sea sands: link between microstructure and seismic properties. Geophysical Research Letters 27, 2761–2764.

Avseth, P., Mukerji, T., Mavko, G., 2005. Quantitative Seismic Interpetation. Cambridge University Press, New York.

Avseth, P., Skeji, N., 2011. Rock physics modeling of static and dynamic reservoir properties – a heuristic approach for cemented sandstone reservoirs. The Leading Edge 30, 90–96.

Backus, G.E., 1962. Long-wave elastic anisotropy produced by horizontal layering. Journal of Geophysical Research 68, 4427–4440.

Biot, M.A., 1956. Theory of propagation of elastic waves in a fluid saturated porous solid. I. Low-frequency range. Journal of the Acoustical Society of America 28, 168–178.

Blangy, J.P., 1992. Integrated seismic lithologic interpretation: the petrophysical basis, Ph.D. Dissertation, Stanford University.

Blangy, J.P., Strandenes, S., Moos, D., Nur, A., 1993. Ultrasonic velocities in sands, revisited. Geophysics 58, 344–356.

Bosch, M., Cara, L., Rodrigues, J., Navarro, A., Diaz, M., 2007. A Monte Carlo approach to the joint estimation of reservoir and elastic parameters from seismic amplitudes. Geophysics 72, O29–O39.

Bosch, M., Carvajal, C., Rodrigues, J., Torres, A., Aldana, M., Sierra, J., 2009. Petrophysical seismic inversion conditioned to well-log data: methods and application to a gas reservoir. Geophysics 74, O1–O15.

Castagna, J.P., Backus, M., 1993. Offset Dependent Reflectivity—Theory and Practice of AVO Analysis. Society of Exploration Geophysics.

Castagna, J.P., Swan, H.W., Foster, D.J., 1998. Framework for AVO gradient and intercept interpretation. Geophysics 63, 948–956.

Chadwick, A., Williams, G., Delepine, N., Clochard, V., Labat, K., Sturton, S., Buddensiek, M., Dillen, M., Nickel, M., Lima, A., Arts, R., Neele, F., Rossi, G., 2010. Quantitative analysis of time-lapse seismic monitoring data at the Sleipner CO_2 storage operation. The Leading Edge 29, 170–177.

Daley, T.M., Ajo-Franklin, J.B., Doughty, C., 2011. Constraining the reservoir model of an injected CO_2 plume with crosswell CASSM at the Frio-II brine pilot. International Journal of Greenhouse Gas Control 5, 1022–1030.

Das, A., Batzle, M., 2008. Modeling studies of heavy oil in between solid and fluid properties. The Leading Edge 27, 1116–1123.

Dodds, K., Daley, T., Freifeld, B., Urosevic, M., Kepic, A., Sharma, S., 2009. Developing a monitoring and verification plan with reference to the Australian Otway CO_2 pilot project. The Leading Edge 28, 812–818.

Dvorkin, J., Nur, A., 1996. Elasticity of high-porosity sandstones: theory for two North Sea datasets. Geophysics 61, 1363–1370.

Gassmann, F., 1951. Uber die elastizitat poroser medien. Vierteljahrsschrift Naturwissenschaften Gesellschaft 96, 1–23.

Ghaderi, A., Landrø, M., 2009. Estimation of thickness and velocity changes of injected carbon dioxide layers from prestack time-lapse seismic data. Geophysics 74, O17–O28.

Hashin, Z., Shtrikman, S., 1963. A variational approach to the elastic behavior of multiphase materials. Journal of the Mechanics and Physics of Solids 11, 127–140.

Joy, C.A., 2011. The effects of pressure variations and chemical reactions on the elasticity of the lower Tuscaloosa sandstone of the Cranfield field, MS. The University of Texas at Austin Master Thesis.

Knight, R., Nolen-Hoeksema, R., 1990. A laboratory study of dependence of elastic wave velocities on pore scale fluid distributions. Geophysical Research Letters 17, 1529–1532.

Knott, C.G., 1899. Reflection and refraction of elastic waves, with seismological applications. Philosophical Magazine 48, 567–569.

Kordi, M., Hovorka, S., Milliken, K., Treviño, R., Lu, J., 2010. Diagenesis and reservoir heterogeneity in the Lower Tuscaloosa Formation at Cranfield field. In: Presented at the 60th Annual Convention of the Gulf Coast Association of 96 Geological Societies and the Gulf Coast Section of SEPM, Mississippi, San Antonio, TX, October 10–12, 2010, GCCC Digital Publication Series #10–13.

Lu, J., Kharaka, Y., Thordsen, J., Horita, J., Karamalidis, A., Griffith, C., Hakala, A., Ambats, G., Cole, D., Phelps Manning, M., Cook, T., Hovorka, P.S., 2012. CO_2–rock–brine interactions in Lower Tuscaloosa Formation at Cranfield CO_2 sequestration site, Mississippi, USA. Chemical Geology 291, 269–277.

Lumley, D., 2010. 4D seismic monitoring of CO_2 sequestration. The Leading Edge 29, 150–155.

Ma, J., Morozov, I., 2010. AVO modeling of pressure-saturation effects in Weyburn CO_2 sequestration. The Leading Edge 29, 178–183.

Mavko, G., Mukerji, T., 1998. Bounds on low-frequency seismic velocities in partially saturated rocks. Geophysics 63, 918–924.

Mindlin, R.D., 1949. Compliance of elastic bodies in contact. Journal of Applied Mechanics 16, 259–568.

Reuss, A., 1929. Berechnung der fleissgrenzen von mischkristallen auf grund der plastizitatsbedingung fur einkristalle. Zeitschrift fur Angewandte Mathematik aus Mechanik 9, 49–58.

Russell, B.H., Heldin, K., Hilterman, F.J., Lawrence, R.L., 2003. Tutorial: fluid-property discrimination with AVO: a Biot-Gassmann perspective. Geophysics 68, P29–P39.

Rutherford, S.R., Williams, R.H., 1989. Amplitude-versus-offset variations in gas sands. Geophysics 54, 680–688.

Shuey, R.T., 1985. A simplification of the Zoepprtiz equations. Geophysics 50, 609–614.

Siggins, A.F., Lwin, M., Wisman, P., 2010. Laboratory calibration of the seismo-acoustic response of CO_2 saturated sandstone. International Journal of Greenhouse Gas Control 4, 920–927.

Simm, R., White, R., Uden, R., 2000. The anatomy of AVO crossplots. The Leading Edge 19, 150–155.

Stine, J.A., 2004. Sensitivity of AVO reflectivity to fluid properties in porous media, Masters Thesis, The University of Texas at Austin.

Theye, T., Parra, T., Lathe, C., 2003. Room temperature compressibility of clinochlore and chamosite. European Journal of Minerals 15, 465–468.

Tosaya, C.A., 1982. Acoustical properties of clay-bearing rocks, Ph.D. Dissertation, Stanford University.

Urosevic, M., Pevzner, R., Kepic, A., Wisman, P., Shulakova, V., Sharma, S., 2010. Time-lapse seismic monitoring of CO_2 injection into a depleted gas reservoir–Naylor Field, Australia. The Leading Edge 29, 164–169.

Verdon, J.P., Kendall, J-M., White, J.D., Angus, D.A., Fisher, Q.J., Urbancic, T., 2010. Passive seismic monitoring of carbon dioxide storage at Weyburn. The Leading Edge 29, 208–214.

Voigt, W., 1907. Bestimmung der elastizitatskonstanten von eisenglanz. Anallen der Physik 24, 129–140.

Wang, Z., 2000. Dynamic versus static properties of reservoir rocks, in seismic and acoustic velocities in reservoir rocks. SEG Geophysics Reprint Series 19, 531–539.

Woeber, A.F., Katz, S., Ahrens, T.J., 1963. Elasticity of selected rocks and minerals. Geophysics 28, 658–663.

Zoeppritz, K., 1919. ErdbebenwellenVIIIB, Ueber Reflection and Durchgang seis-mischer Wellen durch Unitestigkeitsflaechen. Goettinger Nachrichten. I, 66–84.

MODELING FLUID COMPOSITION IN CO_2 SATURATED SANDSTONE USING A STATISTICAL ROCK PHYSICS APPROACH, CRANFIELD FIELD, CRANFIELD, MS.

Analysis of the effects of injected CO_2 on the seismic response of reservoirs is important because it can provide improved characterization and monitoring of sites undergoing CO_2 injection for both utilization and storage purposes. In this study we used two different inversion schemes to better understand the effect of CO_2 saturation on the elastic parameters of the Cranfield reservoir in to which over 3.4 million tons of CO_2 have been injected. The first was statistical classification to determine which combination of elastic parameters were best discriminated CO_2 saturation. The second scheme used that combination to invert jointly a rock physics model for CO_2 saturation and porosity. This determines the reliability of the chosen parameters and the rock physics model for discriminating fluid composition and correlated properties. For the first scheme, we calibrated a rock physics model to well data from the Cranfield reservoir interval. We then performed fluid substitution to model density and velocity logs for different in situ CO_2 saturations. From the modeled synthetic logs, we computed bivariate probability density functions (PDFs). The modeled logs were statistically classified to these PDFs to determine which elastic parameters and parameter combinations best discriminated fluid composition. P-impedance and the Vp/Vs ratio was the best combination. The logs of the highest performing parameter combination were then input into an inverted rock physics model to generate modeled logs of CO_2 saturation and porosity. In the second step, this combination was used to invert the contact cement rock physics model for CO_2 saturation and porosity. This rock physics

model provides a quantitative link between elastic parameters and the lithology and fluid saturation of the reservoir, and through inversion, can be used to model CO_2 saturation and porosity. Results from the second phase of this study showed that the model was able to predict porosity and an absence of in situ CO_2 with a relatively high degree of accuracy. However, when some CO_2 was present, the ability to discriminate among varying CO_2 concentrations was reduced. The two-step approach taken here estimates the relationship and associated uncertainty between the elastic properties and the reservoir properties of interest at the well log scale. Future work may use these estimates along with high-resolution seismic data to provide spatial distribution of injected CO_2.

A new stochastic inversion workflow for time-lapse data: hybrid starting model and double-difference inversion

Yi Tao[1], Mrinal K Sen[2,3], Rui Zhang[4] and Kyle T Spikes[2]

[1] ConocoPhillips, Houston, TX, USA

[2] Jackson School of Geosciences, The University of Texas at Austin, Austin, TX, USA

[3] National Geophysical Research Institute, Uppal Road, Andhra Pradesh, India

[4] Lawrence Berkeley National Laboratory, CA, USA

E-mail: yitao1983@gmail.com

Abstract

Non-uniqueness presents challenges to seismic inverse problems, especially for time-lapse inversion where multiple inversions are needed for different vintages of seismic data. For time-lapse applications, the focus typically is to detect relatively small changes in seismic attributes at limited locations and to relate these differences to changes in the underlying physical properties. We propose a robust inversion workflow where the baseline inversion uses a starting model, which combines a high-frequency fractal component and a low-frequency component from well log data. This starting model provides an estimate of the null space based on fractal statistics of well data. To further focus on the localized changes, the inverted elastic parameters from the baseline model and the difference between two time-lapse data are summed together to produce the virtual time-lapse seismic data. This is known as double-difference inversion, which focuses primarily on the areas where time-lapse changes occur. The misfit function uses both data and model norms so that the ill-posedness of the inverse problem can be regularized. We pre-process the seismic data using a local correlation-based warping algorithm to register the time-lapse datasets. Finally, very fast simulated annealing, a nonlinear global search method, is used to minimize the misfit function. We demonstrate the effectiveness of our method with synthetic data and field data from Cranfield site used for CO_2 sequestration studies.

(Some figures may appear in colour only in the online journal)

Introduction

Time-lapse (4D) seismic data is an important tool to monitor temporal changes of reservoir properties associated with hydrocarbon production and environmental engineering. With the improvement of the data fidelity and repeatability in seismic acquisition, processing and interpretation, 4D seismic data are now used routinely for many reservoir management tasks. Successful applications of time-lapse data have been reported worldwide for different types of reservoirs (Koster

et al 2000, Landrø et al 2001, Lumley 2001, Hall et al 2006, Vedanti and Sen 2009). Future 4D seismic technology is expected to be even more sensitive to small dynamic reservoir changes induced by fluid flow and/or pressure changes to provide more quantitative interpretations (Calvert 2005, Boelle et al 2012).

Seismic inversion is an important tool for quantitative interpretation of time-lapse seismic data. It minimizes the misfit between observed and modelled seismic data and converts the seismic information into elastic properties such as

1

P-wave velocity, S-wave velocity and density (e.g., Sen 2006). There are many types of seismic inversions. They mainly differ from each other by the forward modelling strategy and the use of travel time and/or amplitude information. Travel time is sensitive to smooth changes or low-frequency variations that are important in defining the geometrical structures at a large scale. Seismic amplitude, on the other hand, is affected by small-scale heterogeneities or high-frequency variations within the seismic resolution range. Travel time tomography (e.g., Ivansson 1985, Grand 1987) uses ray tracing as its forward modelling method and uses only travel time information from seismic data. Full waveform inversion (e.g., Tarantola 1984, Pratt *et al* 1998, Sen and Roy 2003, Tao and Sen 2013a) uses wave equation modelling approaches and both travel time and amplitude information. Despite the general success of this inversion method within the seismic imaging community in the last few decades, it is still not applicable at the reservoir characterization scale because of its computational cost and the local minimum issue, especially for the high-frequency components (Virieux and Operto 2009). Up to now, seismic inversion with a convolution model as its forward modelling scheme (e.g., Rowbotham *et al* 2003, Hampson *et al* 2005) is still the most effective and efficient approach for reservoir characterization. This approach typically uses NMO corrected angle gathers and focuses primarily on the amplitude variation with angle in predefined seismic horizons. Under this framework, high-frequency well log data are combined with seismic data to obtain considerably high resolution and geologically continuous elastic properties.

Time-lapse seismic inversion requires high resolution and robust algorithms (Zhang and Castagna 2011) because accurate differences in elastic properties are needed to map dynamic reservoir parameters. In general, a robust inversion algorithm depends on the starting model (e.g., Tao and Sen 2012). A fractal starting model captures the self-similar or self-affine statistics of well logs. It is an effective approach to estimate the high-frequency components not constrained by band-limited seismic data (Srivastava and Sen 2009 and 2010). This approach overcomes the limitation of random Gaussian statistics in building a high-frequency starting model such as kriging (Isaaks and Srivastava 1989) and Markov-chain Monte Carlo methods (Sen and Stoffa 1991, 1995, Hong and Sen 2009). Some aliased estimates, especially at the beginning and end of the well logs can be improved with a combination of the fractal model and a low-frequency starting model (Tao *et al* 2011). When a stochastic optimization approach, such as very fast simulated annealing (VFSA) is used, reliable high resolution elastic properties can be obtained from seismic data. This approach can be directly extended to the inversion of 4D seismic data.

A conventional time-lapse inversion workflow requires two separate inversions and a subtraction of the two different inverted datasets to obtain a difference image. Because of noise characteristics and different nonlinear search processes, this inversion method can introduce spurious structures instead of real time-lapse signatures in the difference image. Double-difference inversion (Watanabe *et al* 2004, Denli and Huang 2009, Zheng *et al* 2011) uses the inverted results from the

inversion of baseline data and the difference of the two time-lapse datasets for the inversion of the repeat data. In the second inversion process, 'virtual' data is used instead of the repeat data. Synthetic data generated using the inverted result of the first pass is added with time-lapse residual data to form the data. Thus, it focuses mainly on the residual data where temporal changes have taken place while keeping other places constant.

In this paper, we report on a robust workflow for the stochastic inversion of time-lapse datasets. This workflow uses the hybrid starting model (high-frequency fractal model plus low-frequency trend) as *a priori* constraint for the baseline data and double-difference inversion for the repeat data. A local correlation-based warping algorithm is used to register the time-lapse datasets to improve on the consistency of time-lapse signatures. VFSA is used as the nonlinear global search approach to find the minimum of the misfit function. This approach is justified by synthetic data and by comparison with the conventional inversion workflow. We further demonstrate the feasibility of this approach with a field dataset from Cranfield CO_2 sequestration site.

Methodology

Hybrid starting model

We start with the mathematical description of the fractal approximation of well log data to describe how we build a hybrid starting model for the inversion of the baseline data. Synthesizing well logs with fractal statistics is justified by the fact that self-similar and self-affine statistics can be approximated by fractal heterogeneities (Hewett 1986, Stefani and Gopa 2001, Browaeys and Fomel 2009). Within a fractal framework, elastic and petrophysical properties of the subsurface can be represented by a smooth background trend at a large scale plus fluctuations at finer scales

$$f(\mathbf{r}) = f_0(\mathbf{r}) + \sigma(\mathbf{r}), \qquad (1)$$

where $f(\mathbf{r})$ is any elastic or petrophysical parameter, $f_0(\mathbf{r})$ is the background parameter which can be defined deterministically, and $\sigma(\mathbf{r})$ is the spatial fluctuation which can be synthesized stochastically.

The fractal series $f(\mathbf{r})$ has a zero expectation value, a determined spatial covariance and a power-law dependence of its Fourier spectrum

$$P(k) = k^{-\beta}, \qquad (2)$$

where $P(k)$ is the energy spectrum, k is the wavenumber and β is a scaling factor that is linearly related to the Hurst coefficient H (Hurst *et al* 1965). Specifically, $\beta = 2H - 1$ is for fractal Gaussian noise and $\beta = 2H + 1$ is for fractal Brownian motion.

To examine if a time signal or a space signal has strong or weak fractal behaviour, spectral analysis is used, and the value of β is examined. For a signal with $\beta = 0$, the energy spectrum is independent of frequency and the signal consists of uncorrelated random noise. When $\beta > 0$, the signal is positively correlated to the data. When $\beta < 0$, the signal is anti-correlated.
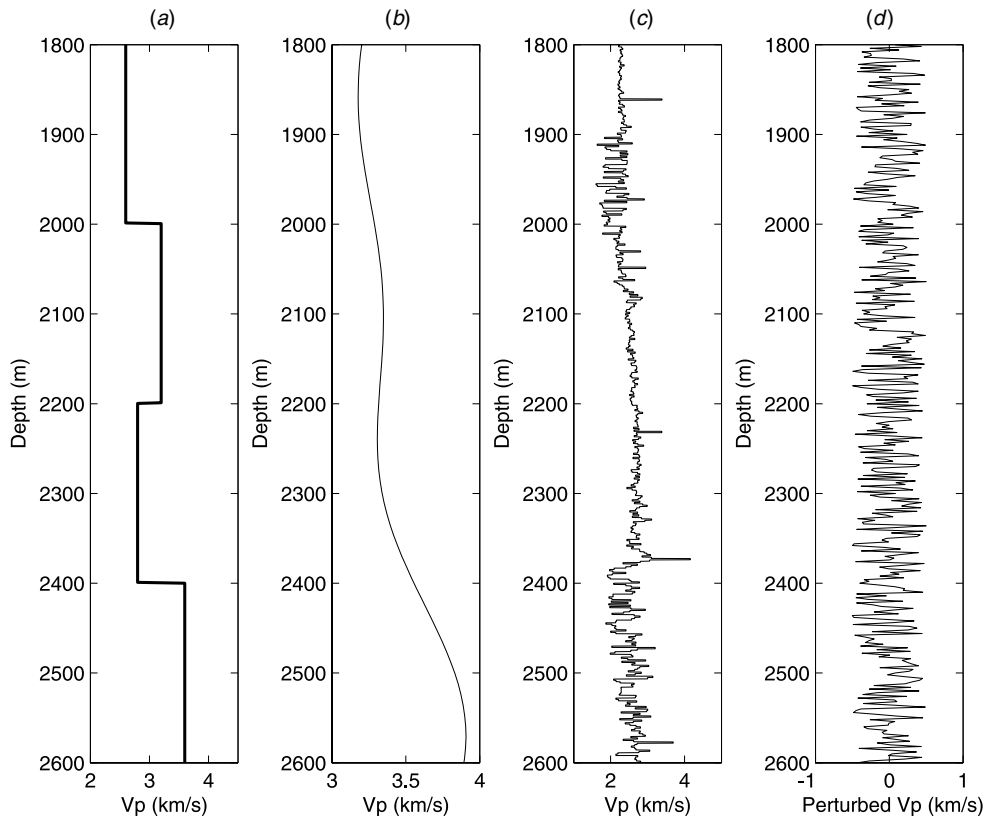
2

Figure 1. (*a*) A blocky heterogeneous velocity curve; (*b*) a smooth low-frequency velocity trend derived from a well log; (*c*) P-wave velocity from a real well log data; (*d*) random velocity perturbations.

We describe the aforementioned fractal behaviour with examples. Figure 1 shows four different velocity curves and figure 2 shows the corresponding log–log Fourier spectrum. Although only velocity is shown here, spectra of other parameters, such as density, impedance, permeability and porosity, can also be depicted this way. Figure 1(*a*) is a blocky velocity model that represents layered strata that can generate seismic reflections. A blocky model consists of piecewise Heaviside functions while its amplitude spectrum is a superposition of *sinc* functions (figure 2(*a*)). Figure 1(*b*) is a smoothed low-frequency background velocity trend that can be used as a low-frequency starting model for inversion. Its spectrum does not have perturbations and it typically cannot be synthesized by a fractal series accurately (figure 2(*b*)). For a typical well log shown in figure 1(*c*), fractal statistics provide a good approximation of it considering power-law dependence of its spectrum (figure 2(*c*)). A random series (figure 1(*d*)) can be considered as a special case of a fractal series when the least-square-fit slope of its log–log spectrum equals zero (figure 2(*d*)).

To describe a given well log data using fractal statistics, three parameters should be estimated from the well log data: the expectation, the standard deviation and the Hurst coefficient. Expectation and standard deviation can be easily estimated. To estimate the Hurst coefficient, several methods

are available. Following Srivastava and Sen (2009), we use a method known as rescaled range analysis:

$$\frac{R}{S} = \left(\frac{N}{2}\right)^H, \qquad (3)$$

where R and S are the range and standard deviation, respectively, of the given dataset. N is the number of sampling points. R, S and N can be directly obtained from the data. The Hurst coefficient (H) is obtained by the slope of the straight line fitting of $\log(R/S)$ versus $\log(N/2)$.

After H is estimated, we synthesize the log curve with a fractal Gaussian series. This involves a process to generate random perturbations with an estimated auto-covariance and H (Srivastava and Sen 2010). The auto-covariance of the fractal Gaussian noise can be given by

$$\mathbf{A}(t) = 0.5\sigma^2(|t+1|^{2H} - 2|t|^{2H} + |t-1|^{2H}), \qquad (4)$$

where $\mathbf{A}$ is the auto-covariance and σ is the standard deviation of the well log data. Here t represents time, but the series can also be a spatially sampled.

A fractal initial model typically has the same frequency range as that of the well log data. This provides a good estimate of the null space that is not constrained by seismic data. However, this method can introduce spurious frequency components when the well log does not strictly satisfy fractal statistics. Random realizations of well data can also bring frequency uncertainties into the model space. This can be compensated for with a hybrid model approach. Suppose we

3
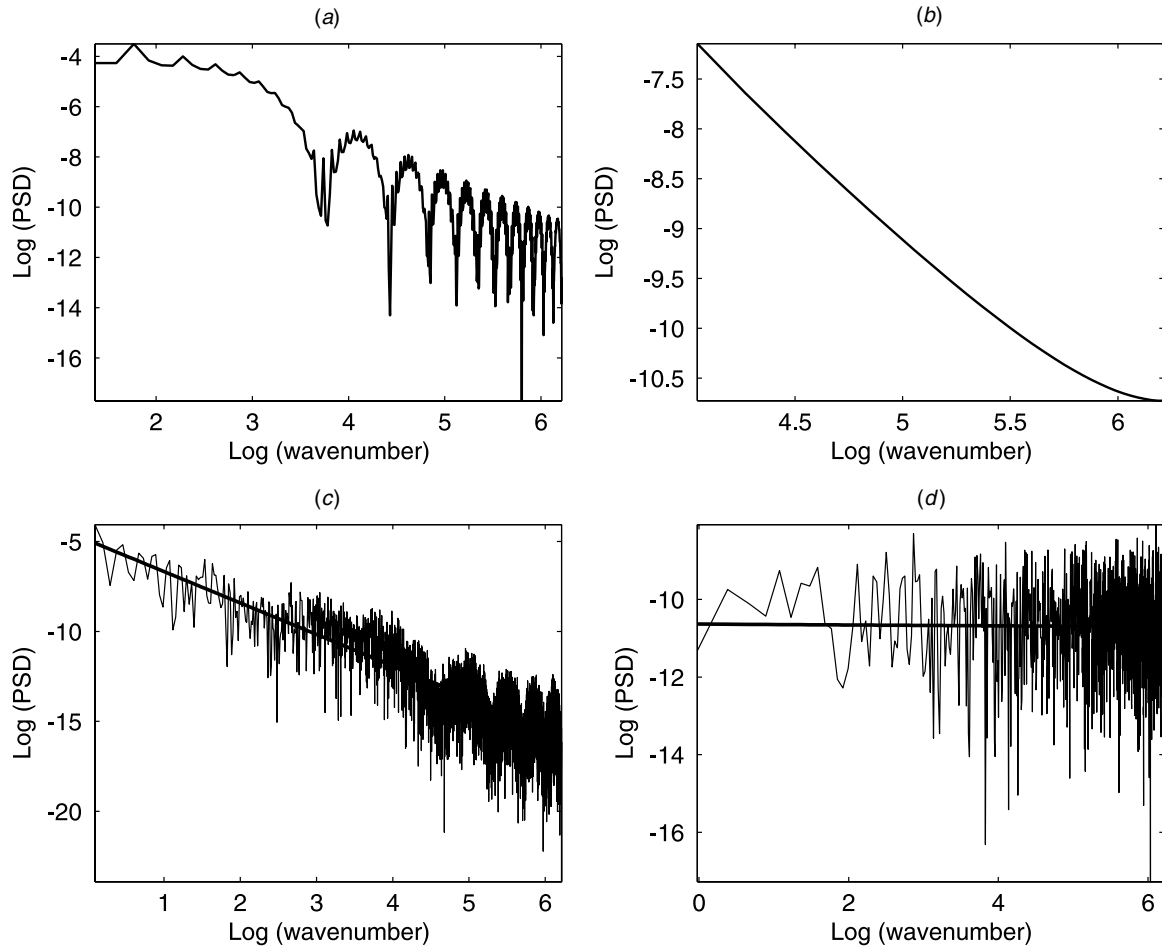
Figure 2. Log–log spectra for: (*a*) a blocky velocity; (*b*) a smooth velocity; (*c*) P-wave velocity from a real well log data; (*d*) random velocity perturbations. A linear trend is estimated for (*c*) and (*d*).

have the low-frequency model $\mathbf{m}_1$ and the fractal model $\mathbf{m}_2$, the hybrid starting model $\mathbf{m}$ is given by

$$\mathbf{m} = \alpha \mathbf{m}_1 + (1 - \alpha)\mathbf{m}_2, \tag{5}$$

where α is a weight number such that $0 \leqslant \alpha \leqslant 1$. Setting $\alpha = 0.5$ gives the low-frequency trend and high-frequency components equal weight.

Figure 3 shows a comparison between synthetic well logs generated using the fractal method and the hybrid method. Compared to the real impedance log, the pure fractal model has some deviations, especially at the start and end of the log. The root mean square error is 19.4 km/s*g/cc for the pure fractal model, and is 10.5 km/s*g/cc for the hybrid model. Our hybrid model better matches the true answer.

Forward modelling and optimization scheme

This paper uses a convolution model as its forward modelling scheme. The modelling assumes a layered Earth. Inversion of the seismic data is based on a trace-by-trace approach and can be applied to 3D datasets with horizon constraints. The forward model is given by

$$\mathbf{S}(\theta, t) = \mathbf{w}(t) * \mathbf{R}(\theta, t) + \mathbf{n}(t), \tag{6}$$

where $\mathbf{S}(\theta, t)$ is the observed seismic data, typically an angle gather in a prestack case; $\mathbf{w}(t)$ is the source wavelet, and $\mathbf{n}(t)$

is the noise; $\mathbf{R}(\theta, t)$ is the reflectivity, and the angle-dependent reflectivity can be given by a linear approximation of the Zoeppritz equations (e.g., Fatti *et al* 1994). A full Zeoppritz equation with 1D reflectivity modelling can also be used (e.g., Sen and Roy 2003). This paper uses the convolution model for numerical simplicity and computational efficiency.

The presence of noise and limited knowledge of the true models make most real inverse problems ill-posed. Regularization is necessary to make the inversion process more robust. Similar to Srivastava and Sen (2010), we choose the misfit function between the observed and calculated data as

$$M = \frac{2\sum |\mathbf{d}_{\text{obs}} - \mathbf{d}_{\text{cal}}|}{\sum |\mathbf{d}_{\text{obs}} - \mathbf{d}_{\text{cal}}| + \sum |\mathbf{d}_{\text{obs}} + \mathbf{d}_{\text{cal}}|}$$
$$+ \varepsilon_1 \sum |\mathbf{m}_{\text{new}} - \mathbf{m}_0| + \varepsilon_2 \sum |\mathbf{A}_{\text{obs}} - \mathbf{A}_{\text{cal}}|, \tag{7}$$

where $\mathbf{d}_{\text{obs}}$ and $\mathbf{d}_{\text{cal}}$ are the observed and calculated seismic data, respectively; $\mathbf{m}_{\text{new}}$ and $\mathbf{m}_0$ are the model parameter of new iteration and the starting model, respectively; $\mathbf{A}_{\text{obs}}$ and $\mathbf{A}_{\text{cal}}$ are the observed and calculated autocorrelation series; ε_1 and ε_2 are the weighting factors. L1 norm is chosen for the model parameters to scale the outlier noises (Tao and Sen 2013b). We choose $\varepsilon_1 = \varepsilon_2 = 0.01$ for our applications.

The optimization method used in this paper is VFSA. VFSA is an efficient global searching algorithm with its ability to identify optimal parameters for nonlinear problems

4
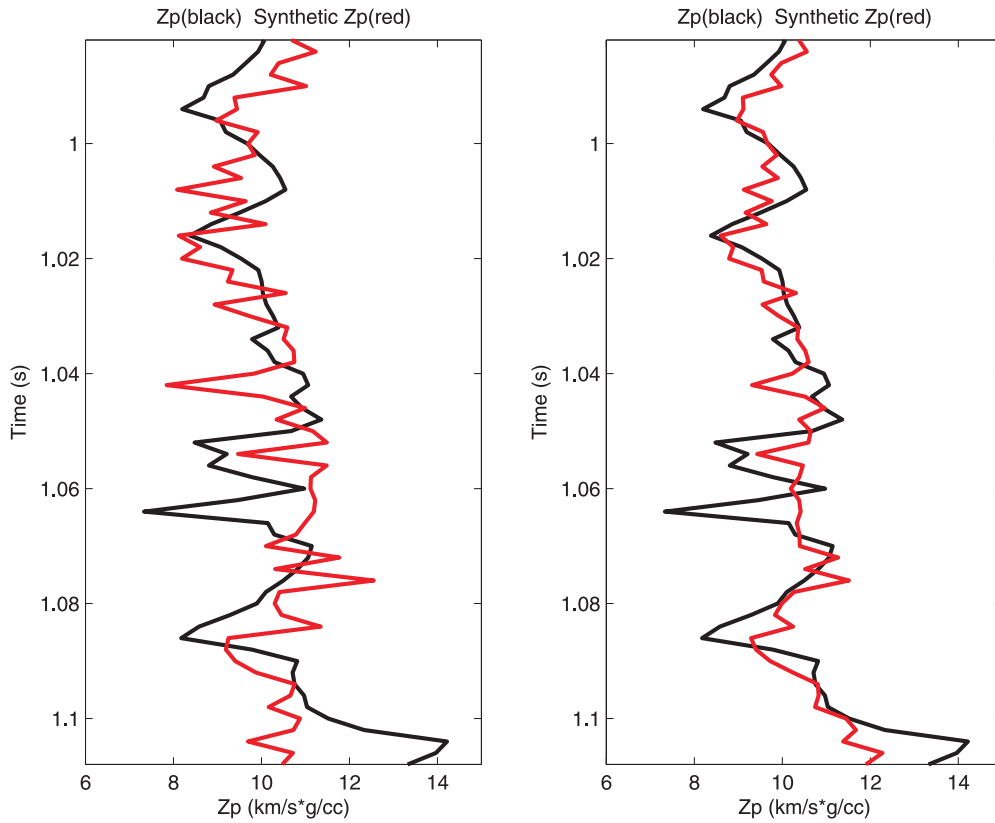
Figure 3. Comparison of synthetic well log P-impedance (red) with real well log data (black). Left: fractal model. Right: hybrid model.

(Sen and Stoffa 1995). This algorithm requires the model space to be subdivided into equally spaced intervals. Within different iterations, the temperature, i.e. the control parameter, is selected based on an exponentially decaying cooling schedule. Starting from an initial model, which is typically random but here it is a fractal-based hybrid model, a new model is accepted by evaluating the probability of the misfit function. This search process is typically known as the Metropolis algorithm (Metropolis *et al* 1953). The best-fit model is accepted by repeating this inversion process to reduce the bias of sampling in the model space. In theory, global optimization based on Monte Carlo searching can be applied to other computational intensive inverse problems such as full waveform inversion with two-way wave equation forward modelling (e.g., Tarantola 1984). However, because the number of forward calculations is typically prohibitively large, global optimization methods are still considered impractical for those problems.

Double-difference inversion

Double-difference inversion for 4D seismic data has been applied in travel time tomography (Waldhauser and Ellsworth 2000) and full waveform inversion problems (Watanabe *et al* 2004, Denli and Huang 2009). Here we extend this idea to the stochastic time-lapse inversion.

Conventional inversion strategy for time-lapse data involves two independent inversions. Changes in the

underlying elastic properties are given by a subtraction between those model parameters. This can be written as

$$\delta \mathbf{m} = \mathbf{m}_{\text{repeat}} - \mathbf{m}_{\text{base}}, \tag{8}$$

where $\delta \mathbf{m}$ is the time-lapse changes of the model parameters. $\mathbf{m}_{\text{repeat}}$ and $\mathbf{m}_{\text{base}}$ are the inverted model parameters for the repeat data and baseline data, respectively. The two different inversions typically require the same inversion workflow to ensure that the inversion process itself does not introduce time-lapse difference. However, because of non-uniqueness, independent inversions of these two different datasets may converge into different results that are not true time-lapse signatures.

Similar to joint 4D inversion proposed by Johnson *et al* (2009), where geophysical parameters are used to constrain the inversion of hydrogeologic data, inverted parameters from the baseline data is used as a constraint for the repeat data for double-difference inversion. The observed repeat data is replaced by the simulated data of the baseline model and the residual data

$$\mathbf{d}_{\text{obs\_repeat}} = f(\mathbf{m}_{\text{base}}) + \Delta \mathbf{d}_{\text{obs}}, \tag{9}$$

where $f(\mathbf{m}_{\text{base}})$ is the calculated data for the baseline model. Δd_{obs} is the residual data between two different datasets and $\Delta \mathbf{d}_{\text{obs}} = \mathbf{d}_{\text{obs\_repeat}} - \mathbf{d}_{\text{obs\_base}}$.

This method is equivalent to conventional time-lapse inversion if the inversion performed on the baseline data truly match the observed data (Zheng *et al* 2011). However, data matching cannot be perfect for real inverse problems. Correspondingly, the inverted time-lapse difference for

```
┌─────────────────────────────────────────┐
│  Process seismic data with warping method,│
│  tie the well with seismic data, extract  │
│  wavelet and pick horizons                │
└─────────────────────────────────────────┘
                    │
                    ▼
┌─────────────────────────────────────────┐
│  Estimate fractal statistics from well    │
│  log data, generate a hybrid starting     │
│  model.                                    │
└─────────────────────────────────────────┘
                    │
                    ▼
┌─────────────────────────────────────────┐
│  Use VFSA to invert the baseline data     │
│  with the hybrid starting model.          │
└─────────────────────────────────────────┘
                    │
                    ▼
┌─────────────────────────────────────────┐
│  Use a double difference inversion        │
│  approach to invert the repeat data.      │
└─────────────────────────────────────────┘
                    │
                    ▼
┌─────────────────────────────────────────┐
│  Obtain inverted time-lapse difference    │
└─────────────────────────────────────────┘
```

Figure 4. Flow chart of the inversion methodology used in this paper.

double-difference inversion and the conventional approach are typically different. Because $\Delta \mathbf{d}_{obs}$ corresponds to the localized changes in the time-lapse survey, this method only inverts for the actual differences in the seismic data. Therefore, it better constrains the inversion of the repeat data.

Local correlation-based warping

Seismic data for time-lapse purposes are typically processed through multiple independent workflows. At any step, if not processed properly, artefacts can be brought into the final image. Although modern acquisition techniques have increased the repeatability of time-lapse datasets, acquisition can still introduce unwanted artefacts. To correctly identify the time-lapse signature, we use a warping method to isolate the changes at the reservoir interval from its surrounding environments. Warping was firstly investigated as a cross equalization method on 4D seismic image registration (Rickett and Lumley 2001, Druzhinin and MacBeth 2001).

In this paper, the warping method is applied on the repeat data based on a maximum local correlation trend (Fomel 2007, Fomel and Jin 2009). This approach involves the calculation of the local correlation, followed by squeezing and stretching the stacked image of the repeat data with reference to the baseline data. This is a trace-by-trace approach, which implements a shaping regularization to stabilize the local-correlation output. The maximum local-correlation trend is picked automatically as same as semblance picking in velocity analysis (Fomel 2009). To summarize the inversion process in this paper, we show the basic steps as a workflow in figure 4.
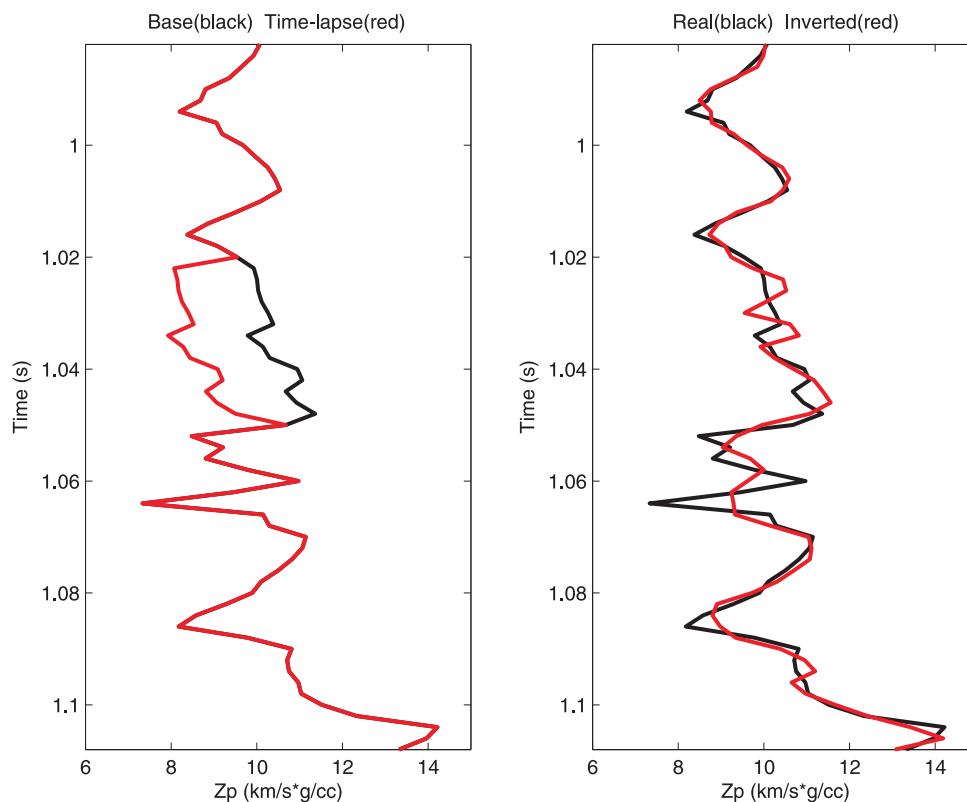
Figure 5. Left: P-impedance log data of the baseline model (black) and the time-lapse model (red); Right: comparison of inverted impedance (red) for the baseline model with the true model (black).

6
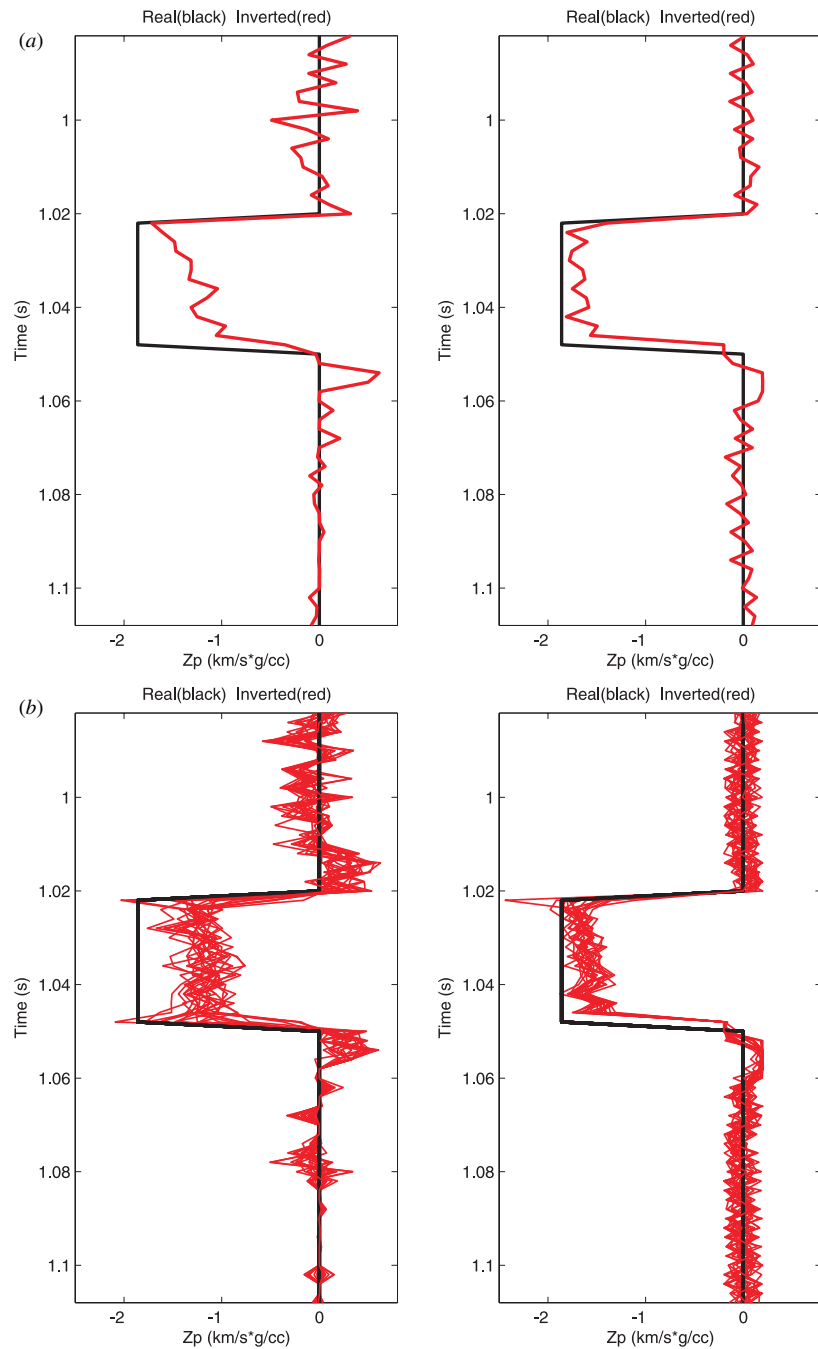
Figure 6. (*a*) Comparison of the inverted impedance difference with conventional approach (left) and the double-difference inversion approach (right); (*b*) multiple realizations of (*a*). For all of those plots, black denotes the true difference and red denotes the inverted difference.

Numerical examples

Synthetic validation

Synthetic examples are used to validate the effectiveness of our inversion workflow. Since this inversion requires an initial model with high-frequency components, we create 1D synthetic data and 2D synthetic data based on the hybrid initial model from Hampson–Russell's demonstration datasets (Srivastava and Sen 2010). This impedance model also involves extrapolating the impedance well log based on picked horizons. Seismic dataset is created by convolving a wavelet with the reflectivity derived from the impedance model.

Figure 5 shows the 1D P-impedance well log data and its corresponding inverted result. The time-lapse impedance model is created by putting an impedance difference of 1860 m/s*g/cc from 1.02 to 1.05 s. This is used to simulate the effect of injected CO_2. We use a constant impedance difference for all the sampling points within a reservoir interval to simplify the fluid substitution and to quantitatively analyse how our inversion workflow spatially resolves the time-lapse difference. From the inverted result of the baseline model,

7
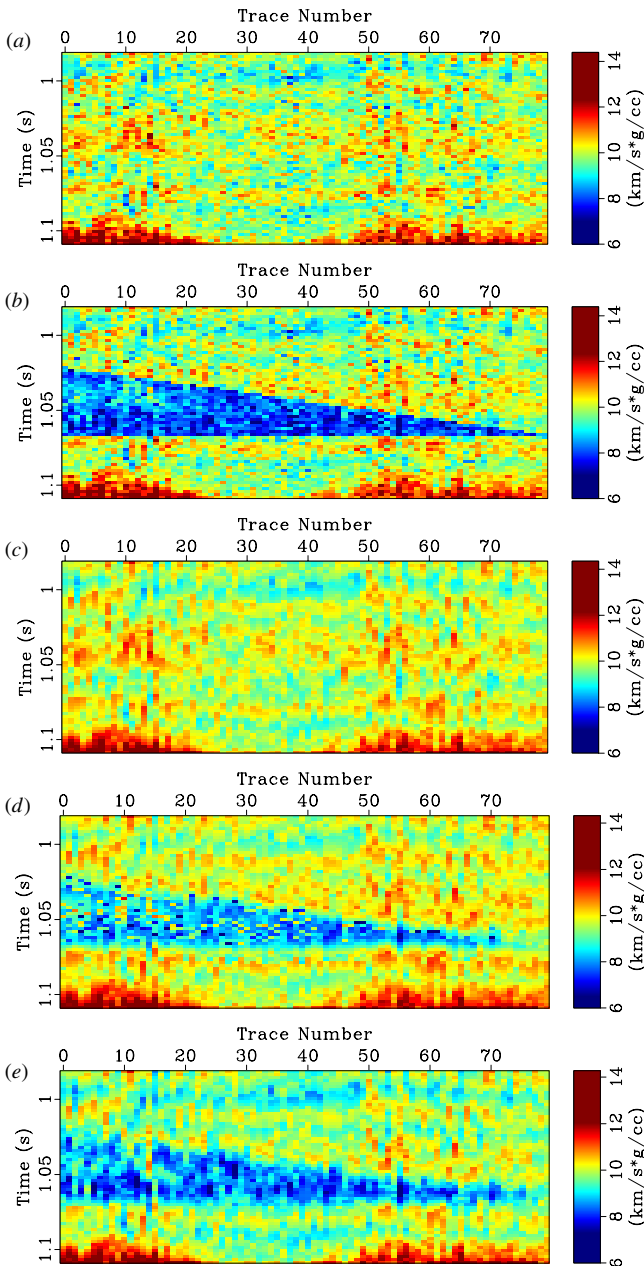
Figure 7. P-impedance plots for (*a*) baseline model; (*b*) time-lapse model; (*c*) inverted base line model; (*d*) inverted time-lapse model with conventional approach; (*e*) inverted time-lapse model with double-difference inversion.

we observe that, in general, stochastic inversion using a hybrid initial model can provide effective estimate of the true impedance, despite some mismatches because of the tuning effects of seismic data.

Figure 6 shows the inverted best-fit P-impedance difference of the 1D model using a conventional approach (two separate independent inversions) and double-difference inversion. Both approaches detect the decreased impedance change due to CO_2 injection. However, the magnitude of the impedance difference with the conventional approach is smaller than the true difference, and there are some deviations outside the target interval. In comparison, inversion with
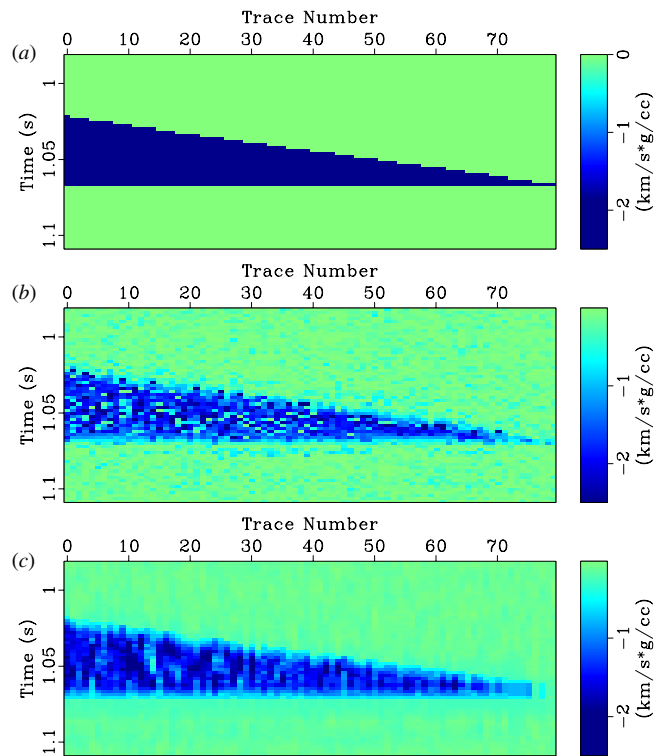
Figure 8. Comparison of the subtracted P-impedance with conventional approach and with double-difference inversion. (*a*) True difference; (*b*) inverted difference with conventional approach; (*c*) inverted difference with double-difference inversion.

the double-difference approach produces better matching of the target interval and fewer deviations outside of it. For stochastic inversion, multiple realizations produce slightly different inverted results because the optimization strategy randomly selects different model parameters. Figure 6(*b*) shows 20 realizations of the inverted differences. We observe that the deviations for different inversions are quite small, especially for the double-difference inversion. This suggests that our inversion workflow is stable.

Figure 7 shows 2D true impedance models and their corresponding inverted models with the two approaches. Figure 8 shows the impedance differences. The geometry is a wedge model to test how our algorithm can resolve the tuning effects of thin-bed layers. Similar to the 1D scenario, for each case, inverted impedance model is close to the true model. Although the inverted difference becomes smaller than the true answer when the layer becomes thinner, both of the approaches could resolve the wedge model very well. The inverted difference with a double-difference inversion approach matches the shape of the wedge better than conventional approach. Double-difference inversion also shows better match in terms of amplitude of the difference inside the wedge model and better constrains the deviations outside the places where temporal changes occur.

Field data applications

The field data used in this study comes from Cranfield in southwest Mississippi. The Gulf Coast Carbon Center (GCCC)

8
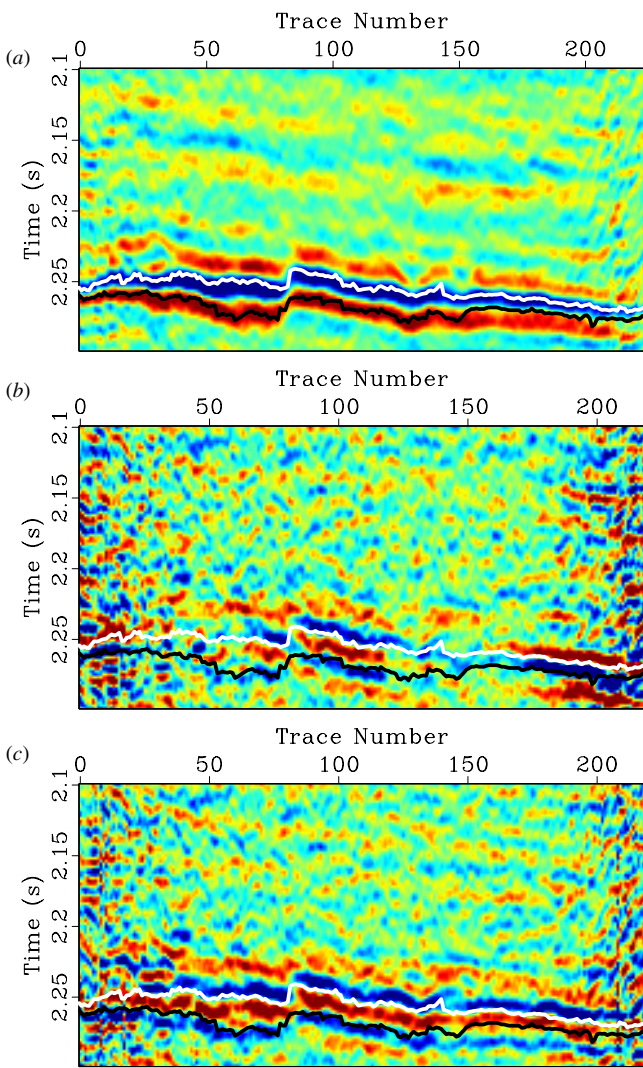
Figure 9. A cross-section of (*a*) pre-injection seismic data; (*b*) time-lapse difference without warping; (*c*) with local correlation-based warping. Two horizons are overlaid to this plot. The white denotes the top sand, and base denotes the bottom sand of the injection interval.

at the University of Texas used this site for CO_2 injection at 23 drilled well locations. The injection interval is the lower

Tuscaloosa formation from 3012 to 3142 m below the surface. From 2008 to 2010, a cumulative mass of 2.2 million metric tons of CO_2 was injected. To monitor this CO_2 injection process, pre-injection seismic data were acquired in 2007 before the CO_2 injection, and post-injection seismic data were acquired in 2010 (Hovorka *et al* 2011).

The injection interval of the lower Tuscaloosa formation at Cranfield appears as a thin bed layer with the thickness around 15 m, and no overburden emission is detected from the *in situ* well-log measurements. This leads to an assumption that the time shifts at this Cranfield datasets are aliasing because injected CO2 will not change the thin bed characteristics of the injection interval. This confirms that a warping method is necessary to identify the true time-lapse signature for this dataset.

Figure 9 shows a cross-section of the pre-injection seismic data and the calculated time-lapse differences. For comparison, the differences calculated using the warped and non-warped post-injection data are shown. Within the injection interval (the two picked horizons in figures 9(*b*) and (*c*)), the original difference (figure 9(*b*)) shows the opposite sign of the amplitude for different crossline locations. This processing-induced misalignment could cause false interpretations of the time-lapse signatures and false estimation of CO_2 saturations. After warping, seismic differences become laterally continuous for all the crossline locations. This is because the time-shift has been separated from amplitude changes (Fomel and Jin 2009). We think warping might help improve the fidelity of time-lapse interpretation. However, we cannot rule out the possibilities that data without warping are more close to the true time-lapse signatures because of the heterogeneities in the injection interval.

Well-to-seismic analysis was performed to find optimal wavelets, which ensure the well log data tie well with seismic section. The extracted wavelet and its corresponding spectrum are shown in figure 10. This wavelet is close to zero phase. After pre-processing with warping and wavelet extraction, the well log data were resampled to the seismic sampling interval and extrapolated to the entire seismic section with the guidance of picked horizons. A hybrid starting model was then built based on the extrapolated well logs and used for the inversion of the pre-injection data.
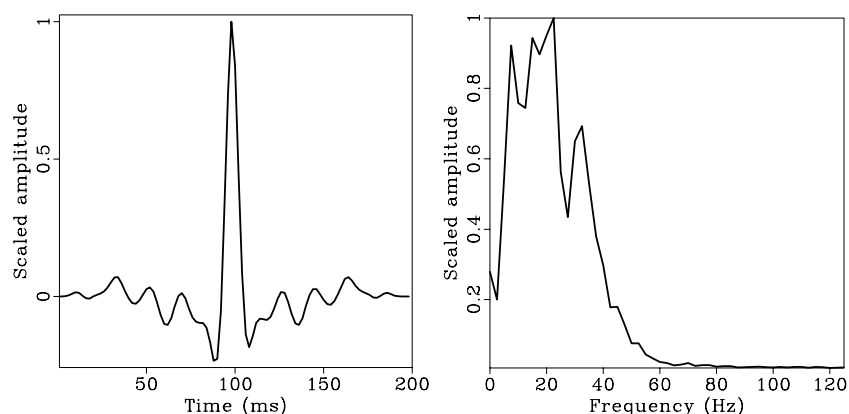
Figure 10. Wavelet used for the Cranfield datasets. Left: wiggle plot of the wavelet; right: its corresponding spectrum.

9
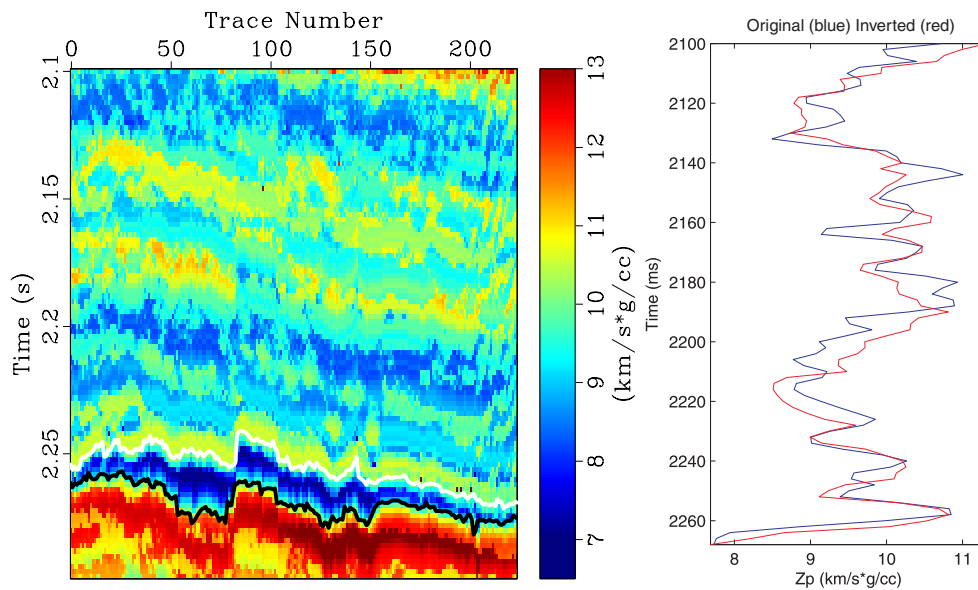
Figure 11. Inverted P-impedance for the pre-injection data (left). Right shows the true impedance (scaled to the seismic data sampling interval) and inverted result at the well location.
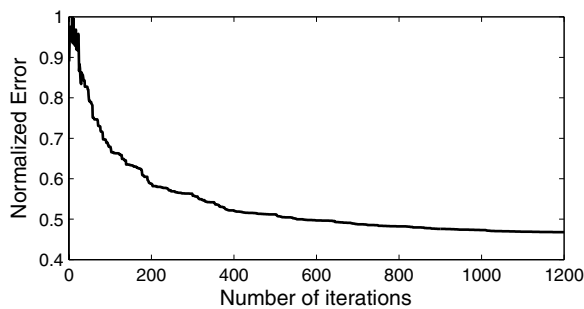
Figure 12. Normalized misfit versus number of iterations at the well location.

Figure 11 shows the inverted P-impedance for the pre-injection data. There is one well located in this seismic section. A comparison of the inverted result at a well location is shown on the right. In general, the inverted impedance agrees with the true impedance. Within the injection interval, the impedance is apparently lower than the surrounding environment. The convergence history at the well location is shown in figure 12. This resembles a typical convergence history of the VFSA optimization scheme. At the beginning, the misfit has some fluctuations. After 400 iterations, this searching is close to the global minimum and begins a slow searching process. The observed seismic data and inverted seismic data for the 2D line are shown in figure 13. Most of the key features of the observed seismic data are captured by the simulated data using the inverted impedance.

Figure 14 shows the subtracted P-impedance for different scenarios. Within the injection interval, there are some discrepancies between the conventional approach (figures 14(*a*) and (*b*)) and double-difference inversion (figures 14(*c*) and (*d*)). The most notable discrepancy is that the inverted difference for double-difference inversion has a longer time span. As analysed by the synthetic examples, we think that the inverted results with a double-difference
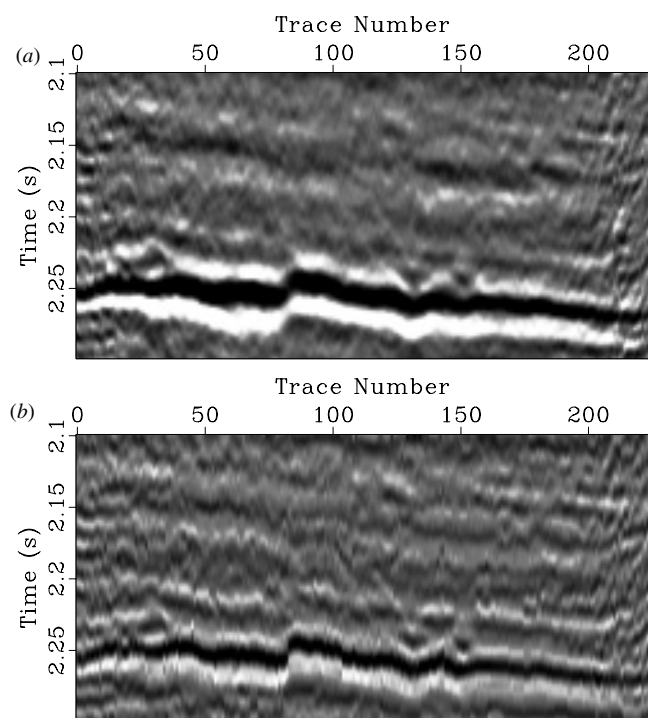
Figure 13. Comparison of the pre-injection seismic data and inverted result. (*a*) Observed seismic data; (*b*) simulated data with inverted P-impedance.

approach can better capture the true time-lapse difference. Also, conventional inversion (figures 14(*a*) and (*b*)) has more fluctuations of the inverted difference outside the CO_2 injection interval than the double-difference inversion approach (figures 14(*c*) and (*d*)). Similar to the seismic data, misalignment of the impedance difference exists for the non-warped seismic data (figures 14(*a*) and (*b*)). Inverted results show same negative change of P-impedance across the picked

10
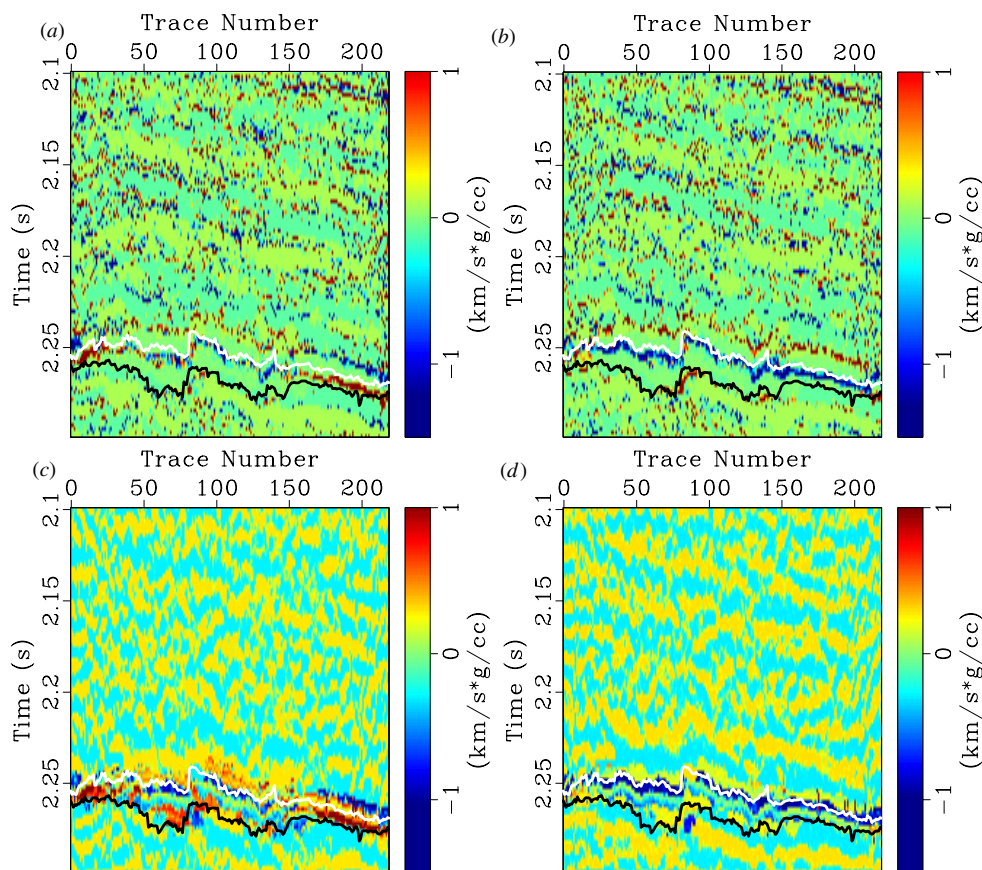
Figure 14. Comparison of inverted time-lapse differences for four different scenarios. (*a*) Conventional inversion of the data without warping; (*b*) double-difference inversion of the data without warping; (*c*) conventional inversion of the data with warping; (*d*) double-difference inversion of the data with warping.

horizons. There is an impedance decrease below the picked top sand horizon on the inverted warped result (figures 14(*c*) and (*d*)). This confirms the conjecture that most CO_2 accumulates at the top of the injection interval.

Conclusions

We have presented a robust stochastic time-lapse inversion strategy. This workflow involves two key steps. The first step is to invert the baseline model with a hybrid starting model which uses both the high-frequency fractal component and the low-frequency component of the well log data. The second step is to use a double-difference inversion scheme to focus on the local areas where time-lapse changes have occurred. We find that double-difference inversion is able to capture the time-lapse differences better than the conventional separate inversion approach. In addition, inversions with warped data show continuous change of the reservoir properties. This suggests that the CO_2 may accumulate more at the top of the injection interval.

Acknowledgments

References

Boelle J L, Brechet E, Ceragioli E, Nawab R, Lecerf D and Lafram A 2012 A large-scale validation of OBN technology for time-lapse studies through a pilot test, deep offshore Angola *Leading Edge* **31** 397–403

Browaeys T J and Fomel S 2009 Fractal heterogeneities in sonic logs and low-frequency scattering attenuation *Geophys.* **74** WA77–92

Calvert R 2005 4D technology: where are we, and where are we going? *Geophys. Prospect.* **53** 161–71

Denli H and Huang L 2009 Double-difference elastic waveform tomography in the time domain *79th Annu. Int. Meeting, SEG* (expanded abstracts) pp 2302–6

Druzhinin A and MacBeth C 2001 Robust cross-equalization of 4D-4C PZ migrated data at Teal South *71st Annu. Int. Meeting, SEG* (expanded abstracts) pp 1670–3

Fatti J L, Smith G C, Vail P J, Strauss P J and Levitt P R 1994 Detection of gas in sandstone reservoirs using AVO analysis *Geophys.* **59** 1362–76

Fomel S 2007 Local seismic attributes *Geophys.* **72** A29–33

11

Fomel S 2009 Velocity analysis using AB semblance *Geophys. Prospect.* **57** 311–21

Fomel S and Jin L 2009 Time-lapse image registration using the local similarity attribute *Geophys.* **74** A7–11

Grand S P 1987 Tomographic inversion for shear velocity beneath the North American plate *J. Geophys. Res.* **92** 14065–90

Hall S A, MacBeth C, Stammeijer J and Omerod M 2006 Time-lapse seismic analysis of pressure depletion in the southern gas basin *Geophys. Prospect.* **54** 63–73

Hampson D P, Russell B H and Bankhead B 2005 Simultaneous inversion of pre-stack seismic data *75th Annu. Int. Meeting, SEG* (expanded abstracts) pp 1633–6

Hewett T A 1986 Fractal distribution of reservoir heterogeneity and their influence on fluid transport *61st Annu. Technical Conf., SPE* p 15386

Hong T and Sen M K 2009 A new MCMC algorithm for seismic waveform inversion and corresponding uncertainty analysis *Geophys. J. Int.* **177** 14–32

Hovorka S D *et al* 2011 Monitoring a large volume CO_2 injection: year two results from Secarb project at Denburys Cranfield, Mississippi, USA *Energy Procedia 10th Int. Conf. on Greenhouse Gas Control Technologies* vol 4 pp 3478–85

Hurst H E, Black R P and Simaika Y M 1965 *Long-Term Storage: An Experimental Study* (London: Constable)

Isaaks E H and Srivastava R M 1989 *An Introduction to Applied Geostatistics* (New York: Oxford University Press) p 561

Ivansson S 1985 A study of methods for tomographic velocity estimation in the presence of low-velocity zone *Geophys.* **50** 969–88

Johnson T C, Versteeg R J, Huang H and Routh P S 2009 Data-domain correlation approach for joint hydrogeologic inversion of time-lapse hydrogeologic and geophysical data *Geophys.* **74** F127–40

Koster K, Gabriels P, Hartung M, Verbeek J, Deinum G and Staples R 2000 Time-lapse seismic surveys in the North Sea and their business impact *Leading Edge* **19** 286–93

Landrø M, Strønen L K and Digranes P 2001 Mapping reservoir pressure and saturation changes using seismic methods–possibilities and limitations *First Break* **19** 671–7

Lumley D 2001 Time-lapse seismic reservoir monitoring *Geophys.* **66** 50–3

Metropolis N, Rosenbluth A W, Rosenbluth M N, Teller A H and Teller E 1953 Equation of state calculations by fast computing machines *J. Chem. Phys.* **21** 1087–92

Pratt R G, Shin C and Hicks G J 1998 Gauss-Newton and full Newton methods in frequency-space seismic waveform inversion *Geophys. J. Int.* **133** 341–62

Rickett J E and Lumley D E 2001 Cross-equalization data processing for time-lapse seismic reservoir monitoring: a case study from the Gulf of Mexico *Geophys.* **66** 1015–25

Rowbotham P S, Marion D, Lamy P, Insalaco E, Swaby P A and Boisseau Y 2003 Multidisciplinary stochastic impedance inversion: integrating geological understanding and capturing reservoir uncertainty *Pet. Geosci.* **9** 287–94

Sen M K 2006 *Seismic Inversion* (Richardson, TX: SPE Publications)

Sen M K and Roy I G 2003 Computation of differential seismograms and iteration adaptive regularization in prestack waveform inversion *Geophys.* **68** 2026–39

Sen M K and Stoffa P L 1991 Nonlinear one-dimensional seismic waveform inversion using simulated annealing *Geophys.* **56** 1624–38

Sen M K and Stoffa P L 1995 *Global Optimization Methods in Geophysical Inversion* (Amsterdam: Elsevier)

Srivastava R P and Sen M K 2009 Fractal-based stochastic inversion of poststack seismic data using very fast simulated annealing *J. Geophys. Eng.* **6** 412–25

Srivastava R P and Sen M K 2010 Stochastic pre-stack seismic inversion using fractal based priors *Geophys.* **75** R47–59

Stefani J and Gopa S D 2001 On the power-law behavior of subsurface heterogeneity *61st Annu. Int. Meeting, SEG* (expanded abstracts) pp 2033–6

Tao Y, Spikes K and Sen M K 2011 Stochastic seismic inversion using both fractal and low-frequency priors *81st Annu. Int. Meeting, SEG* (expanded abstracts) pp 2732–6

Tao Y and Sen M K 2012 Shallow splay fault properties of the Nankai Trough accretionary wedge inferred from seismic inversion *J. Geophys. Eng.* **9** 1–11

Tao Y and Sen M K 2013a Frequency-domain full waveform inversion with plane-wave data *Geophys.* **78** R13–23

Tao Y and Sen M K 2013b Suppressing non-Gaussian noises with scaled receiver wavefield for reverse-time migration: comparison of different approaches *Geophys. Prospect.* at press doi:10.1111/1365-2478.12016

Tarantola A 1984 Inversion of seismic reflection data in the acoustic approximation *Geophysics* **49** 1259–66

Vedanti N and Sen M K 2009 Seismic inversion tracks *in situ* combustion: a case study from Balol oil field, India *Geophys.* **74** B103–12

Virieux J and Operto S 2009 An overview of full waveform inversion in exploration geophysics *Geophys.* **74** WCC127–52

Waldhauser F and Ellsworth W L 2000 A double-difference earthquake location algorithm: method and application to the Northern Hayward fault, California *Bull. Seismol. Soc. Am.* **90** 1353–68

Watanabe T, Shimizu S, Asakawa E and Matsuoka T 2004 Differential waveform tomography for time-lapse crosswell seismic data with application to gas hydrate production monitoring *74th Annu. Int. Meeting, SEG* (expanded abstracts) pp 2323–6

Zhang R and Castagna J 2011 Seismic sparse-layer reflectivity inversion using basis pursuit decomposition *Geophys.* **76** R147–58

Zheng Y, Barton P and Singh S 2011 Strategies for elastic full waveform inversion of time-lapse Ocean Bottom Cable (OBC) seismic data *81st Annu. Meeting, SEG* (expanded abstracts) pp 4195–200

Characterization of a saturated, fractured porous rock and estimation of its fracture-fluid factors

Jiao Xue[1,2], Mrinal K. Sen[1,3], Robert H. Tatham[1]*
[1]Jackson School of Geosciences, The University of Texas at Austin
[2]Institute of Geophysics and Geomatics, China University of Geosciences, Wuhan, China
[3]CSIR-National Geophysical Research Institute, Hyderabad, India

Summary

For fluid-saturated porous rocks with fractures, the elastic moduli are related not only to the physical properties of the host rock and fractures, but also to the fluid-infill material and hydraulic connectivity between pores and fractures. In the low frequency limit, considering fluid flow and hydraulic equilibrium between pores and fractures, we propose to use a fracture-fluid factor matrix to characterize the effect of the fractures and fluids. Here, the fracture-fluid factors are a combination of physical properties of the dry/saturated host rock, fractures and fluid infill, instead of the commonly applied normal and tangential fracture weaknesses. In this paper, we derive analytic expressions for the proposed fracture-fluid factors, express the anisotropic parameters and approximate P-wave reflection coefficients in terms of these fracture-fluid factors. Next, assuming the orientation of the fractures, physical properties of the overburden and unfractured background rock are determined. We use simulated annealing inversion to estimate the fracture-fluid factors. Inversion results from synthetic AVOA data, with 10% Gaussian random noise, show that the fracture-fluid factors can be successfully and reliably estimated.

Introduction

Natural fractures in porous reservoirs often control the permeability. Thus, characterization of fractures in a saturated porous rock is important. For a porous isotropic medium with dry or hydraulically isolated aligned fractures, the fractures may be described in terms of normal and tangential fracture compliances (Schoenberg, 1980). However, for fluid-saturated fractured rocks, when compressed or distorted by seismic waves at low frequency, the fluid pressure has sufficient time to equilibrate throughout the fracture and pore space, and the fluid can escape into the equant pores. Thus, they cannot be directly quantified using the linear-slip model (Schoenberg and Douma, 1988) or Hudson's (Hudson, 1980) model. Gurevich (2003) developed a fluid substitution equation by combining linear-slip theory for the dry fractured rock with equant pores and Gassmann's (1951) anisotropic fluid substitution equations. Shaw and Sen (2006) use AVOA data to estimate the fracture weakness and fluid indicator. A schematic representation of a fractured reservoir with equant porosity is shown in figure 1(Gurevich 2009). Using Gurevich's (2003) fluid substitution equations, we obtained the fracture-fluid factors, which show the effect of physical properties of the dry fractures, fracture infill and hydraulic connectivity between fractures and equant pores on the elastic moduli of the saturated rock. Further, we apply AVOA to estimate these fracture-fluid factors.
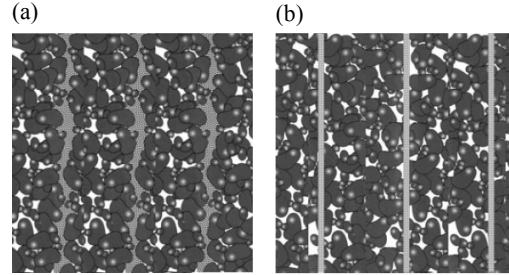
Figure 1: Fractured and porous reservoir: (a) schematic representation and (b) porous model with infinitely thin and highly compliant layers. From Gurevich et al. (2009).

The effect of fracture and fluid

For a porous rock with rotationally invariant fractures, if the symmetry axis of the fracture plane is parallel to the x-axis, the relationship between dry and saturated rock are derived from the Gassmann's equation by Gurevich (2003) :

$$C_{11}^{sat} = \frac{L}{D}\left\{ d_1\theta + \frac{K_f}{\varphi K_g L}\left[L_1\alpha' - \frac{16\mu^2\alpha_0\Delta_N}{9L} \right] \right\}$$

$$C_{13}^{sat} = \frac{\lambda}{D}\left\{ d_1\theta + \frac{K_f}{\varphi K_g \lambda}\left[\lambda_1\alpha' + \frac{8\mu^2\alpha_0\Delta_N}{9L} \right] \right\}$$

$$C_{33}^{sat} = \frac{L}{D}\left\{ d_2\theta + \frac{K_f}{\varphi K_g L}\left[L_1\alpha' - \frac{4\mu^2\alpha_0\Delta_N}{9L} \right] \right\}$$

$$C_{44}^{sat} = \mu$$

$$C_{66}^{sat} = \mu(1-\Delta_T), \qquad (1)$$

Here,

$$L = \lambda + 2\mu$$

$$D = 1 + \frac{K_f}{K_g\varphi}\left(\alpha_0 - \varphi + \frac{K^2\Delta_N}{K_g L} \right)$$

$$\theta = 1 - \frac{K_f}{K_g}$$

$$\alpha_0 = 1 - \frac{K}{K_g}$$

Characterization of saturated, fractured and porous rocks

$$\alpha' = \alpha_0 + \frac{K^2}{K_g L}\Delta_N$$

$$L_1 = K_g + \frac{4}{3}\mu$$

$$\lambda_1 = K_g - \frac{2}{3}\mu$$

$$d_1 = 1 - \Delta_N$$

$$d_2 = 1 - \frac{\lambda^2}{L^2}\Delta_N , \tag{2}$$

In the above equations, φ is the porosity of the host rock; λ and μ are the Lame parameters of the dry host rock; K, K_g and K_f are bulk modulus of the dry host rock, grain mineral, and fluid infill, respectively; Δ_N and Δ_T are normal and tangential fracture weakness of the medium (Schoenberg and Sayers, 1995).

We assume that the stiffness matrix can be expressed as:

$$C = \begin{bmatrix} L^{sat}(1-\Delta_f^{11}) & \lambda^{sat}(1-\Delta_f^{13}) & \lambda^{sat}(1-\Delta_f^{13}) \\ \lambda^{sat}(1-\Delta_f^{13}) & L^{sat}(1-r_{sat}^2\Delta_f^{33}) & \lambda^{sat}(1-r_{sat}\Delta_f^{23}) \\ \lambda^{sat}(1-\Delta_f^{13}) & \lambda^{sat}(1-r_{sat}\Delta_f^{23}) & L^{sat}(1-r_{sat}^2\Delta_f^{33}) \\ & & & \mu \\ & & & & \mu(1-\Delta_T) \\ & & & & & \mu(1-\Delta_T) \end{bmatrix} \tag{3}$$

where, $L^{sat} = \lambda^{sat} + 2\mu$ and $r^{sat} = \lambda^{sat}/L^{sat}$, as λ^{sat} is Lame parameter of the saturated host rock. Let Δ_f be a fracture-fluid factor matrix, expressed by

$$\Delta_f = \begin{bmatrix} \Delta_f^{11} & \Delta_f^{13} & \Delta_f^{13} \\ \Delta_f^{13} & \Delta_f^{33} & \Delta_f^{23} \\ \Delta_f^{13} & \Delta_f^{23} & \Delta_f^{33} \\ & & & 0 \\ & & & & \Delta_T \\ & & & & & \Delta_T \end{bmatrix}, \tag{4}$$

As an excess fracture and fluid factor matrix, Δ_f is related to physical properties of the fractures, fracture infill material, and hydraulic connectivity of fractures and pores, and has an effect on (reduce) the elastic moduli of the saturated rock. We derive the fracture-fluid factors as:

$$\Delta_f^{11} = 1 - \frac{L}{L^{sat}}\frac{1}{D}\left\{d_1\theta + \frac{K_f}{\varphi K_g L}\left[L_1\alpha' - \frac{16\mu^2\alpha_0\Delta_N}{9L}\right]\right\}$$

$$\Delta_f^{13} = 1 - \frac{\lambda}{\lambda^{sat}}\frac{1}{D}\left\{d_1\theta + \frac{K_f}{\varphi K_g \lambda}\left[\lambda_1\alpha' + \frac{8\mu^2\alpha_0\Delta_N}{9L}\right]\right\}$$

$$\Delta_f^{33} = \frac{1}{(r^{sat})^2}\left\{1 - \frac{L}{L^{sat}}\frac{1}{D}\left[d_2\theta + \frac{K_f}{\varphi K_g L}\left(L_1\alpha' - \frac{4\mu^2\alpha_0\Delta_N}{9L}\right)\right]\right\}.\tag{5}$$

For saturated, fractured and porous media, the Thomsen's anisotropic parameters (Thomsen, 1986) $\varepsilon^{(V)}$, $\delta^{(V)}$, γ are:

$$\varepsilon^{(V)} = \frac{C_{11}^{sat} - C_{33}^{sat}}{2C_{33}^{sat}} \approx \frac{(1-2g^{sat})^2\Delta_f^{33} - \Delta_f^{11}}{2}$$

$$\delta^{(V)} = \frac{C_{13}^{sat} - C_{33}^{sat} + 2C_{55}^{sat}}{C_{33}^{sat}}$$

$$\approx -(1-2g^{sat})\Delta_f^{13} + (1-2g^{sat})^2\Delta_f^{33} - 2g\Delta_T$$

$$\gamma = \frac{C_{44} - C_{55}}{2C_{55}} \approx \frac{\Delta_T}{2}, \tag{6}$$

where $g^{sat} = \mu/L^{sat}$.

In order to investigate how the fluid-infill and hydraulically connected fractures with the equant pores affect the elastic elements and anisotropy parameters, we consider high-porosity sandstone with fractures. The P-wave and S-wave velocities of the dry host rock are 3.8 km/s and 2.16 km/s, respectively. The density is 2330 kg/m^3, and the porosity is 18%. These physical properties of the sandstone are documented by Mavko et al. (2003). For the particular case of penny-shaped cracks, the relationship between dry fracture weakness and fracture density (Schoenberg and Douma, 1988, Cardona, 2002) are

$$\Delta_N = \frac{4e}{4e + 3g(1-g)}$$

$$\Delta_T = \frac{16e}{16e + 3(3-2g)}, \tag{7}$$

where, e denotes fracture density, and $g = \mu/L$.

The variation in fracture-fluid factors with fracture density for gas and brine saturated rock is shown in figure 2a. If the fractures and cracks are isolated and fully saturated with fluid, they will be stiff enough to preserve the continuity of the normal displacement component, thus $\Delta_N = 0$. However, for partially fluid saturated fractures or fractures that are hydraulically connected with the equant pores, when compressed, the fluid may escape into the hydraulically connected pores; thus, the fracture-fluid factors will be between 0 and fracture weakness for dry rocks. Figure 2a also shows $\Delta_f^{11} > \Delta_f^{13} > \Delta_f^{33}$. When such a rock is compressed horizontally (perpendicular to the fracture plane), the fluid can move to the equant pores, and the effects of fractures and fluids with fluids are equal to that of the dry fractures with fracture weakness $\Delta_N = \Delta_f^{11}$. Similarly, when such a rock is compressed vertically (parallel to the fracture plane), the effect of fractures and fluids are equal to that of the dry rock

with fracture weakness $\Delta_N = \Delta_f^{33}$. Since $\Delta_f^{11} > \Delta_f^{33}$, it seems that the fluids in the fractures are more likely to move horizontally than vertically, since the fractures themselves are vertical. Figure 2b shows the Thomsen parameters $\varepsilon^{(V)}$ and $\delta^{(V)}$ (Thomsen, 1986) variation with fracture density, for dry and brine saturated rock. Parameters $\varepsilon^{(V)}$ and $\delta^{(V)}$ of brine-saturated rock are negative and larger then that of the dry rock; thus, anisotropy parameters ε and δ for brine-saturated rock will be smaller then that for the dry rock. The fluid reduces the overall degree of anisotropy of the rock.
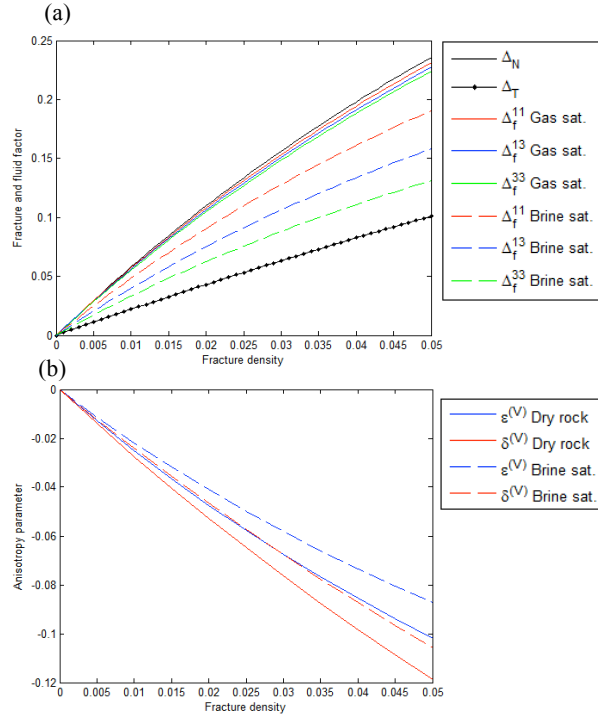
Figure 2: Variation in (a) fracture-fluid factors and (b) anisotropy parameters with fracture density for dry and fluid-saturated rocks.

Reflection coefficient variation with azimuth and incidence angle for brine-saturated fractured rock

We consider a saturated porous rock with a set of parallel dipping fractures (figure 3), with a symmetry axis inclined at an angle θ in x-z plane, and an angle ϕ to the seismic line. Following Shaw and Sen (2004), the linearized PP reflection coefficients for a medium with obliquely dipping fractures and isotropic overburden can be expressed as

$$R_{PP}(i,\phi) = R_{PP}^{iso}(i) + R_{PP}^{ani}(i,\phi), \qquad (8)$$

where,

$$R_{PP}^{iso}(i) = \frac{1}{2}\frac{\Delta Z}{\bar{Z}} + \frac{1}{2}\left[\frac{\Delta\alpha}{\bar{\alpha}} - 4g\frac{\Delta G}{\bar{G}}\right]\sin^2 i + \frac{1}{2}\frac{\Delta\alpha}{\bar{\alpha}}\sin^2 i \tan^2 i$$
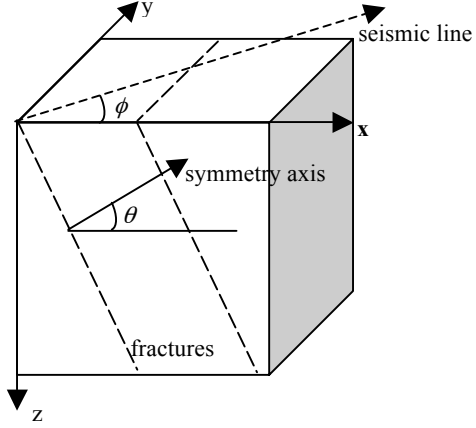
Figure 3: Geometry of the porous medium with dipping fractures. The fractures are striking along y axis, and the symmetry axis of the fracture plane is tilted by an angle θ with the x axis in x-z plane.

$$\begin{aligned}
R_{PP}^{ani}(i,\phi) = {} & \left[\frac{\Delta\delta^{(V)}}{2}\left(\cos^2\psi - \sin^2\theta\right) + 4g\gamma\cos^2\psi\right]\sin^2 i \\
& - \left[\left(\Delta\varepsilon^{(V)} - \Delta\delta^{(V)}\right)\left(\cos^2\psi + \sin^2\theta\right)\sin^2\theta\right]\sin^2 i \\
& + \frac{1}{2}\left[\Delta\delta^{(V)}\left(\cos^2\psi - \sin^2\theta\right)\right]\sin^2 i \tan^2 i \\
& + \frac{1}{2}\left[\left(\Delta\varepsilon^{(V)} - \Delta\delta^{(V)}\right)\left(\cos^4\psi + \sin^4\theta\right)\right]\sin^2 i \tan^2 i, \quad (9)
\end{aligned}$$

where, R_{PP}^{iso} and R_{PP}^{ani} are isotropic and anisotropic part of the reflection coefficients, respectively. In the above equations, $\cos\psi = \cos\phi\cos\theta$, with ϕ and θ representing azimuth of the observation and dipping angle of the fractures, respectively. i is the incidence phase angle, α and β are P-wave and S-wave velocity of the saturated isotropic background rock, Z and G are P-wave impedance and shear modulus. The symbol Δ denotes contrasts in respective properties across the interface, and bar over a symbol denote an average.

For the purpose of investigation, we consider a two-layer model. We assume that the upper layer is water saturated isotropic sandstone and the lower layer is high-porosity sandstone with dipping fractures. The physical properties of the upper layer and that of the dry host rock of the lower layer are shown in table 1. The physical properties of the sandstone are documented by Mavko et al. (2003).

We assume the fracture density to be 0.05. The reflection coefficient variation with azimuth and incidence angle is shown in figure 4a. Figure 4b and 4c indicate that the AVOA of the dipping fractures exhibits a characteristic similar to that of the vertical fractures, and the symmetry axes can be determined, with an ambiguity of 90°.

Characterization of saturated, fractured and porous rocks

Table 1: Physical properties of the two-layer model

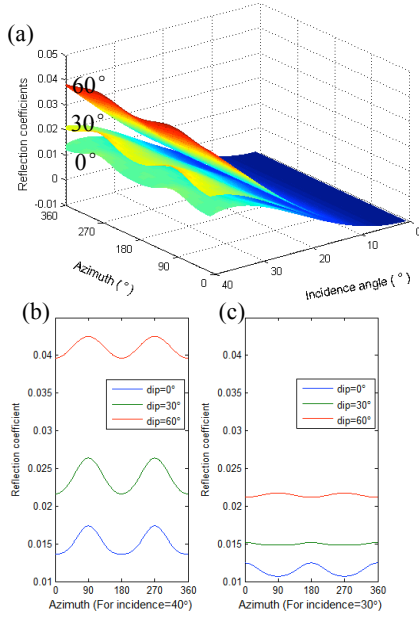| Medium	P-wave velocity m/s	S-wave velocity m/s	Density kg/m^3	Porosity
Isotropic sandstone	4090	2410	2370	16%
Fractured sandstone	3800	2160	2330	18%

Figure 4: (a) Reflection coefficient variation with azimuth and incidence angle for dipping fractures with dip angle of 0°, 30°, and 60°. Variations for (b) incidence angle=40°, and (c) incidence angle=30°.

Fracture-fluid factors inversion

Since for vertical fractures, the anisotropy parameters have a relationship with the fracture-fluid factors, we can substitute equation 6 into equation 8, resulting in:

$$\Delta R(i,\phi) = R_{PP}^{obs}(i,\phi) - R_{PP}^{iso}(i,\phi = 90^\circ)$$

$$= \left[\frac{-(1-2g^{sat})\Delta_f^{13} + (1-2g^{sat})^2\Delta_f^{33}}{2} + g\Delta_T \right] \cos^2\phi\sin^2 i$$

$$+ \frac{1}{2}\left[-(1-2g^{sat})\Delta_f^{13} - 2g\Delta_T \right] \cos^2\phi\sin^2\phi\tan^2 i\sin^2 i$$

$$+ \frac{1}{2}\left[(1-2g^{sat})^2\Delta_f^{33} \right] \cos^2\phi\sin^2\phi\tan^2 i\sin^2 i$$

$$+ \frac{(1-2g^{sat})^2\Delta_f^{33} - \Delta_f^{11}}{4} \cos^4\phi\tan^2 i\sin^2 i. \tag{10}$$

We generated synthetic reflection coefficients (figure 4) for an interface between an isotropic sandstone and porous sandstone with vertical fractures, and estimated the fracture-fluid factors. During the inversion and estimation, we use the reflection data, with 10% Guassian random noise, for incidence angle from 0° to 40° (in 5° increments), and azimuth from 0° to 90° (in 15° increments). We assume that the physical properties of the overburden are known, as well as the parameters of the dry fractures and host rock of the lower layer. We used simulated annealing inversion to estimate the fracture-fluid factors. The results (figure 5) show that the fracture-fluid factors can be estimated with reasonable precision and accuracy after 300 iterations.
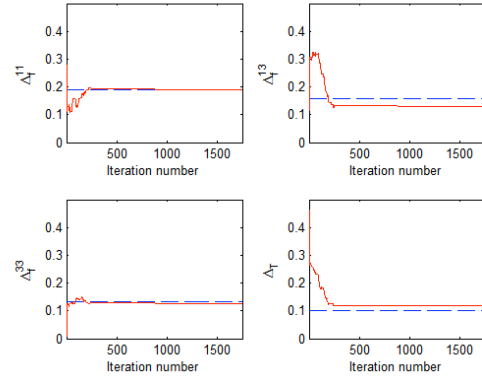
Figure 5: Fracture-fluid factors inversion using simulated annealing algorithm. The blue dashed lines denote the fracture-fluid factors of the input model and the red lines show the results of the inversion.

Conclusions

We proposed the fracture-fluid factors by combining linear-slip theory for the dry fractured rock and Gassmann's anisotropic fluid substitution equations. We also investigate the reflection coefficient variation with azimuth and incidence angle with various dipping angles. The fracture-fluid factors indicate the effect of physical properties of the dry fractures, fracture infill material and hydraulic connectivity of the pores and fractures on the elastic moduli of the saturated host rock. Simulated annealing inversion of synthetic reflection coefficients with 10% Guassian random noise shows that fracture-fluid factors can be determined reliably.

A prestack basis pursuit seismic inversion

Rui Zhang[1], Mrinal K Sen[2], and Sanjay Srinivasan[3]

ABSTRACT

Resolving thin layers and clearly delineating layer boundaries in inverted seismic sections are very important goals for exploration and production. Many seismic inversion methods based on a least-squares optimization approach with Tikhonov-type regularization can lead to unfocused transitions between adjacent layers. A basis pursuit inversion (BPI) algorithm based on the L_1 norm optimization method can, however, resolve sharp boundaries between layers. We have formulated a BPI algorithm for amplitude-versus-angle inversion and investigated its potential to improve contrasts between layers. Like the BPI for poststack case, the sparse layer constraint, rather than the sparse spike constraint, is used to construct the model space as a wedge dictionary. All the elements of the dictionary are bed reflectivities, which include solutions consisting of thin beds as well. With this dictionary, we use an L_1 norm optimization framework to derive three reflectivities, namely, R_p, R_s, and R_ρ. Although BPI does not require a starting model, high-resolution absolute velocities (V_P, V_S) and density (ρ) can be obtained by incorporating initial models in the BPI derived reflectivities. Tests on synthetic and field data show that the BPI algorithm can indeed detect and enhance layer boundaries by effectively removing the wavelet interference.

INTRODUCTION

Prestack seismic data contain more elastic property information on the subsurface than poststack seismic data because the' amplitude variation with offset (AVO) phenomenon is related to V_P, V_S, and density contrasts at layers interface. The original prestack seismic data, which is usually sorted by offset, can be transformed to the angle domain as amplitude variation angle (AVA) data. The V_P,

V_S, and density are then inverted from the AVA data, leading to an AVA inversion problem. Like other inverse problems, the AVA inversion also suffers difficulties stemming from noise contamination, band-limitation, and nonuniqueness (e.g., Varela et al., 2006). For these reasons, regularization has to be used to select a model (or some models) with specific properties among many possible solutions by constraining the problem with a priori information. Tikhonov (1963) first introduces the regularization method for the least square solution, which has been applied to various geophysical problems, for example, traveltime tomography (Bube and Langan, 1997), migration velocity analysis (Liu and Bleistein, 1995), and waveform inversion (Sen and Roy, 2003). Seismic reflectivity inversion with a priori reflectivity patterns is an example of one such application which is used to overcome the limitation of seismic bandwidth. Nguyen and Castagna (2010) use matching pursuit decomposition (MPD) to decompose a seismic trace into a superposition of reflectivity patterns derived from existing well control. Zhang and Castagna (2011) incorporate the basis pursuit technique (Chen et al., 2001) with a wedge model as a priori information in seismic reflection inversion. Beside these deterministic methods, Srivastava and Sen (2009, 2010) and Zhang et al. (2012) develop a stochastic method using a fractal-based simulated annealing algorithm.

The prestack seismic data usually have low signal-noise-ratio (S/N) and are nonstationary, and therefore, it is important to investigate the stability of AVA inversion algorithms with a priori information. The most commonly used sources of a priori information for AVA inversion are some existing rock physics models comprising AVA parameters; for example, V_P-V_S or V_P-density relationships (Castagna et al., 1985; Gardner et al., 1985). Besides these relationships, some available in situ relationships among V_P, V_S, and density, usually derived from well-log measurements, can also be used. This a priori information can be formulated with AVA inversion within the Bayesian framework (Buland and Omre, 2003), which assumes a Gaussian prior probability distribution for the model parameters (Sen and Stoffa, 1996; Scales and Tenorio,

2001). However, the solution via this a priori distribution is too smooth and, hence, follows the band-limitation of the seismic data. To obtain high-resolution models, we propose a set of spiky reflectivity solutions (R_p, R_s, and R_ρ) for the AVA inversion problem, leading to sharp boundaries at interfaces of V_P, V_S, and density.

In this paper we use basis pursuit inversion (BPI), which is an L_1 norm optimization method, to invert AVA prestack seismic data simultaneously for the reflectivity series (R_p, R_s, and R_ρ). These reflectivities can be converted to V_P, V_S, and ρ with the incorporation of an initial model. We demonstrate the effectiveness of our algorithm with application to a synthetic and field data sets. The BPI results from the field data are compared with well logs and conventional inversion results and demonstrate the resolving power of our algorithm.

METHOD

Forward problem

When an incident plane P- wave reaches a boundary between two media, it generates reflected and transmitted P- and S- waves. Zoeppritz (1919) introduces a set of equations describing these reflection and transmission coefficients. However, it is hard to incorporate the Zoeppritz equations for AVA inversion of prestack seismic data because of their nonlinear nature. For this reason, different linear approximations of the Zoeppritz equations have been developed for AVA analysis and inversion (e.g., Bortfeld, 1961; Richards and Frasier, 1976; Aki and Richards, 1980). A linearized approximation of the plane wave reflection coefficient derived by Aki and Richards (1980), which is typically valid up to 40° incidence angle and small changes of elastic properties across a boundary, is commonly used in computing amplitude variation with angle. The P-wave reflection coefficient as a function of the incident angle is given by the sum of three terms,

$$R_{pp}(\theta) = (0.5 + 0.5\tan^2\theta)\frac{\Delta V_P}{\bar{V}_P} + (-4\sin n^2\theta)\frac{V_S^2}{V_P^2}\frac{\Delta V_S}{\bar{V}_S}$$
$$+ \left(0.5 - 2\sin n^2\theta\frac{V_S^2}{V_P^2}\right)\frac{\Delta\rho}{\bar{\rho}}, \quad (1)$$

where $\bar{V}_P$, $\bar{V}_S$, and $\bar{\rho}$ are the average velocities and density values across the boundary; ΔV_P, ΔV_S, and $\Delta\rho$ are the contrasts in the velocity and density values across the boundary; θ is considered to be the incident angle because of the small contrast assumption; and V_S/V_P is the shear-to-compressional wave velocity ratio for the layers. Note that equation 1 assumes small contrast in velocities and density, i.e., the terms $\Delta V_P/\bar{V}_P$, $\Delta V_S/\bar{V}_S$ and $\Delta\rho/\bar{\rho}$ are around 0.2. Equation 1 is generally referred to as the Aki and Richards equation. Because equation 1 is a linear summation of three reflectivity terms with angle dependent coefficients (the terms in brackets), it can be illustrated as a matrix-vector multiplication at each time sample t. For a gather with N angles, the forward problem can be written as

$$\begin{bmatrix} R_{pp}(t,\theta_1) \\ R_{pp}(t,\theta_2) \\ \vdots \\ R_{pp}(t,\theta_N) \end{bmatrix} = \begin{bmatrix} C_p(t,\theta_1) & C_s(t,\theta_1) & C_\rho(t,\theta_1) \\ C_p(t,\theta_2) & C_s(t,\theta_2) & C_\rho(t,\theta_2) \\ \vdots & \vdots & \vdots \\ C_p(t,\theta_N) & C_s(t,\theta_N) & C_\rho(t,\theta_N) \end{bmatrix}$$
$$\times \begin{bmatrix} R_p(t) \\ R_s(t) \\ R_\rho(t) \end{bmatrix}, \quad (2)$$

where C_p, C_s, and C_ρ are angle dependent; R_p, R_s, and R_ρ are three reflectivity time series

$$C_p(\theta_i) = (0.5 + 0.5\tan^2\theta) \quad R_p(t) = \frac{\Delta V_P(t)}{V_P(t)}$$
$$C_s(\theta_i) = \left(-4\sin^2\theta\frac{V_s^2}{V_p^2}\right) \quad R_s(t) = \frac{\Delta V_S(t)}{V_S(t)}$$
$$C_\rho(\theta_i) = \left(0.5 - 2\sin^2\theta\frac{V_s^2}{V_p^2}\right) \quad R_\rho(t) = \frac{\Delta\rho(t)}{\rho(t)}. \quad (3)$$

Convolution of a wavelet with the reflection coefficients then generates a synthetic seismogram for a given angle. The convolution model does not take complete wave propagation effects into account; however, although there is little difference between convolution and wave equation modeling results at angles less than 25°, it could become larger at far angles (Mallick, 2001).

A given wavelet is convolved with both sides of equation 2 to yield equation 4,

$$S_{pp}(t,\theta_i) = \int_0^t R_{pp}(\tau,\theta_i) * \text{wavelet}(t-\tau)d\tau,$$
$$W(t,\theta_i) = \int_0^t C(\tau,\theta_i) * \text{wavelet}(t-\tau)d\tau; \quad (4)$$

where $S_{pp}(t,\theta_i)$ is an angle gather at incident angle θ_i and $W(t,\theta_i)$ is a wavelet kernel matrix. The accuracy of the wavelet plays a critical role on inversion results. A set of synthetic tests on the sensitivity of the wavelet, such as wavelet frequency and phase, are presented by Zhang (2010). The synthetic tests show that the incorrect phase of the wavelet would cause phase errors in the inversion results, whereas the incorrect frequency of the wavelet would produce incorrect results and possible instabilities.

After this convolution operation, we have

$$\begin{bmatrix} S_{pp}(t,\theta_1) \\ S_{pp}(t,\theta_2) \\ \vdots \\ S_{pp}(t,\theta_N) \end{bmatrix} = \begin{bmatrix} W_p(t,\theta_1) & W_s(t,\theta_1) & W_\rho(t,\theta_1) \\ W_p(t,\theta_2) & W_s(t,\theta_2) & W_\rho(t,\theta_2) \\ \vdots & \vdots & \vdots \\ W_p(t,\theta_N) & W_s(t,\theta_N) & W_\rho(t,\theta_N) \end{bmatrix}$$
$$\times \begin{bmatrix} R_p(t) \\ R_s(t) \\ R_\rho(t) \end{bmatrix}, \quad (5)$$

or, more simply, $\mathbf{d} = \mathbf{Gm}$, where S_{pp} represents the prestack angle gather comprising the data vector $\mathbf{d}$; W_p, W_s and W_ρ constitute the wavelet kernel matrix $\mathbf{G}$. The $\mathbf{G}$ matrix is also the Jacobian matrix commonly uses in inverse problem and R_p, R_s, and R_ρ are the reflectivity terms comprising $\mathbf{m}$.

Incorporation of wedge models

In this paper, we assume a blocky layer earth model rather than a transitional model because the sharp boundaries of blocky layers are generally more helpful in interpretation than smooth boundaries. Such blocky layer models will generate spiky reflection coefficients

series at the boundaries, which can be decomposed into a summation of impulse pairs (Bork and Wood, 2001). BPI uses dipole decomposition to represent the reflectivity series as a sum of even and odd impulse pairs multiplied by scalars. The top and base reflectors of a layer can be represented as two impulse functions $c\delta(t)$ and $d\delta(t + n\Delta t)$, where $n\Delta t$ is the time thickness of a thin bed, Δt is the sample rate, and c and d are two reflection coefficients. Dipole decomposition is used to decompose each reflector pair into one even pair r_e and one odd pair r_o

$$r_e = \delta(t) + \delta(t + n\Delta t), \ r_o = \delta(t) - \delta(t + n\Delta t), \quad (6)$$

$$c\delta(t) + d\delta(t + n\Delta t) = a_e * r_e + b_o * r_o. \quad (7)$$

However, the layer thickness is typically unknown. To include all possible bed thicknesses, n varies from zero to a number representing the theoretically resolvable layer time thickness, e.g., one-fourth of the dominant period. For example, for a peak frequency of a seismogram at 25 Hz, with a corresponding period of 40 ms, the resulting maximum wedge thickness becomes 10 ms. The sampling rate Δt plays a decisive role for the accuracy of the timing of reflection coefficients and for the minimum time thickness resolvable. A smaller sampling rate can improve accuracy and resolution.

The wedge models, including the odd and even wedges, are a collection of dipole reflectors with increased time separation (Figure 1b through 1e). Figure 1b and 1c displays odd and even wedge reflectivity models, respectively. Figure 1d and 1e shows corresponding seismic responses after convolution with a given wavelet. Interference from the top and base of the wedge models, which degrades the seismic resolution, becomes useful information for our BPI.

Because the sample rate is Δt, each trace of even wedge reflectivity consists of a pair of equal impulse functions (spikes) with an interval $n\Delta t$. The reflector kernel matrix for the reflectivity pair is constructed by shifting the reflectivity pair along the time axis by $m\Delta t$ samples, where m ranges from one to the number of samples in the seismic trace. Thus, each even wedge reflectivity pattern can be written as

$$r_e(t, m, n, \Delta t) = \delta(t - m\Delta t) + \delta(t - m\Delta t + n\Delta t). \quad (8)$$

Similarly, the odd wedge reflectivity pattern can be written as

$$r_o(t, m, n, \Delta t) = \delta(t - m\Delta t) - \delta(t - m\Delta t + n\Delta t). \quad (9)$$

Three reflectivities R_p, R_s, and R_ρ series can be considered as a summation of even and odd wedge reflectivity patterns shown in equation 10 as follows

$$
\begin{aligned}
R_p(t) &= \sum_{n=1}^{N} \sum_{m=1}^{M} (a_{ep,n,m} * r_e(t, m, n, \Delta t) \\
&\quad + b_{op,n,m} * r_o(t, m, n, \Delta t)) \\
R_s(t) &= \sum_{n=1}^{N} \sum_{m=1}^{M} (a_{es,n,m} * r_e(t, m, n, \Delta t) \\
&\quad + b_{os,n,m} * r_o(t, m, n, \Delta t)) \\
R_\rho(t) &= \sum_{n=1}^{N} \sum_{m=1}^{M} (a_{e\rho,n,m} * r_e(t, m, n, \Delta t) \\
&\quad + b_{o\rho,n,m} * r_o(t, m, n, \Delta t)),
\end{aligned}
\quad (10)
$$

where a_{ep}, b_{op}, a_{es}, b_{os}, $a_{e\rho}$, and $b_{o\rho}$ are the dipole decomposition coefficients; N corresponds to the maximum bed thickness and M corresponds to the maximum data length. By using this decomposition and considering all the coefficients as time series, we can have the matrix form of the decomposition of R_p, R_s, and R_ρ as

$$
\begin{bmatrix} R_p(t) \\ R_s(t) \\ R_\rho(t) \end{bmatrix} = \begin{bmatrix} \mathbf{r}_e & \mathbf{r}_o & 0 & 0 & 0 & 0 \\ 0 & 0 & \mathbf{r}_e & \mathbf{r}_o & 0 & 0 \\ 0 & 0 & 0 & 0 & \mathbf{r}_e & \mathbf{r}_o \end{bmatrix} \times \begin{bmatrix} \mathbf{a}_{ep}(t) \\ \mathbf{b}_{op}(t) \\ \mathbf{a}_{es}(t) \\ \mathbf{b}_{os}(t) \\ \mathbf{a}_{e\rho}(t) \\ \mathbf{b}_{o\rho}(t) \end{bmatrix}.
$$
(11)

When equation 11 is substituted into equation 5, we have

$$
\begin{bmatrix} S_{pp}(t, \theta_1) \\ S_{pp}(t, \theta_2) \\ \vdots \\ S_{pp}(t, \theta_N) \end{bmatrix} = \begin{bmatrix} W_p(t, \theta_1) & W_s(t, \theta_1) & W_\rho(t, \theta_1) \\ W_p(t, \theta_2) & W_s(t, \theta_2) & W_\rho(t, \theta_2) \\ \vdots & \vdots & \vdots \\ W_p(t, \theta_N) & W_s(t, \theta_N) & W_\rho(t, \theta_N) \end{bmatrix}
$$

$$
\times \begin{bmatrix} \mathbf{r}_e & \mathbf{r}_o & 0 & 0 & 0 & 0 \\ 0 & 0 & \mathbf{r}_e & \mathbf{r}_o & 0 & 0 \\ 0 & 0 & 0 & 0 & \mathbf{r}_e & \mathbf{r}_o \end{bmatrix} \times \begin{bmatrix} \mathbf{a}_{ep}(t) \\ \mathbf{b}_{op}(t) \\ \mathbf{a}_{es}(t) \\ \mathbf{b}_{os}(t) \\ \mathbf{a}_{e\rho}(t) \\ \mathbf{b}_{o\rho}(t) \end{bmatrix}. \quad (12)
$$

The multiplication of the wavelet kernel matrix with the matrix of wedge reflectivity patterns forms a new kernel matrix $\mathbf{G}_W$. Similarly, the vector coefficients $\mathbf{a}_{ep}$, $\mathbf{b}_{op}$, $\mathbf{a}_{es}$, $\mathbf{b}_{os}$, $\mathbf{a}_{e\rho}$, and $\mathbf{b}_{o\rho}$, form a new model vector $\mathbf{m}_W$. With this decomposition, any angle gather can be modeled by the summation of wedge seismic dictionary elements. Because equations 11 and 12 share the same coefficients, after the decomposition coefficients $\mathbf{a}_{ep}$, $\mathbf{b}_{op}$, $\mathbf{a}_{es}$, $\mathbf{b}_{os}$, $\mathbf{a}_{e\rho}$, and $\mathbf{b}_{o\rho}$ are calculated by the basis pursuit method in equation 12, the final inverted reflectivities R_p, R_s, and R_ρ can be calculated using equation 11.

Equation 12 is the dipole decomposition result of equation 5, which has been commonly used as a linear equation for prestack seismic inversion problem for decades. The stability of equation 5 relies on several factors, including the wavelet accuracy, data stationarity and noise level. The dipole decomposition, as a unique operation, does not change the stability condition of the equation 12. However, the computational complex of equation 12 is greater than that of equation 5, which is related to the maximum wedge thickness.

Basis pursuit decomposition

Basis pursuit (BP), which is a kind of L_1 optimization method, solves the linear equation by minimizing an objective function of the form given by equation 13.

$$\min[\|\mathbf{d} - \mathbf{G}_W \mathbf{m}_W\|_2 + \lambda \|\mathbf{m}_W\|_1]. \quad (13)$$

However, the L_1-norm regularization isn't the only sparseness-promoting functional; for example, Brossier et al. (2010) discuss Huber criterions for robust optimization. Also, besides the basis pursuit method, other methods can also solve equation 13; for example, the L-BFGS method (Guitton and Symes, 2003). The objective function of the basis pursuit method contains an L_2-norm of the data misfit term and the L_1-norm of the solution (e.g. Gill et al., 1991; Astfalk et al., 1992; Wright, 1992, 1997; Roos, 2006; Varela et al., 2006), where the L_2-term calculates the root mean square error of the data and the L_1-term is the summation of the absolute values of the solution. These two terms are minimized simultaneously to derive the final solution. In this manner, sparse layers with dipole reflector pairs with appropriate thicknesses instead of isolated spikes are determined together with the derived coefficients. The parameter λ is a trade-off factor that controls the sparseness of the solution. A large λ would generate sparse solutions, whereas a small λ could generate smooth solutions. For normalized data sets, its value is usually around one. The best choice of λ on field data will be decided by testing on a small piece of data by calibration with well-log data. Contrary to the poststack BPI algorithm of Zhang and Castagna (2011), the data vector **d** is a prestack angle gather, whereas the matrix G_W is the multiplication of the two middle matrices in equation 12 and the model vector m_W is made of the dipole decomposition coefficients.
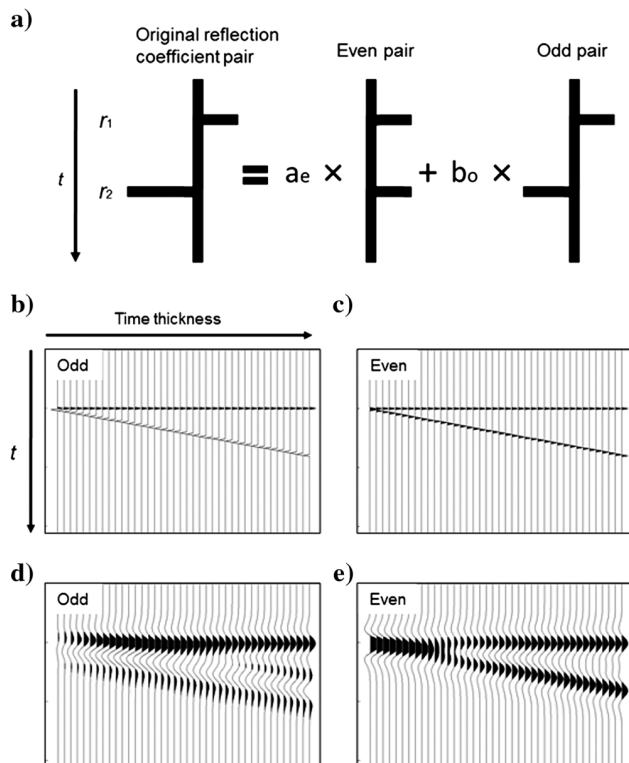
Figure 1. (a) Any arbitrary pair of reflection coefficients r_1 and r_2 can be represented as a sum of even and odd components. The even pair has the same magnitude and sign, and the odd pair has the same magnitude, but opposite sign; (b and c) are odd and even wedge reflectivity models; (d and e) show corresponding model seismic responses with a 30-Hz Ricker wavelet, which become dictionary elements.

INITIAL MODEL

To derive the final output of V_P, V_S, and ρ from the inverted reflectivities, a set of initial models (V_{P0}, V_{S0}, and ρ_0) has to be incorporated. Such initial models are constructed in the same way as is done in the poststack seismic inversion by interpolating and extrapolating well-log measured V_P, V_S, and density values guided by interpreted horizons. Unlike the conventional AVA inversion with output of smooth results, BPI results appear as blocky layers with no wavelet imprint. The primary difference between the two methods lies in the assumption of the earth model, i.e., smooth or blocky transition. The resulting different objective functions are that the conventional inversion employs minimization of L_2-norm of error and solution terms, whereas BPI uses equation 13. Theune et al. (2010) present an analysis of the difference between blocky and smooth inversions based on different distribution assumption, which can be schematically explained in an idealized inverse problem consisting of two layers with different seismic properties, as shown in the solid black line in Figure 2. A potential result of the conventional inversion is illustrated by the red dashed line. Such a result makes the interpretation very difficult because of the strong side lobes and a rather smeared boundary between the two layers. In contrast, the schematic BPI solution (blue dashed line) is nearly constant within the layers and follows the interface more closely.

The blocky assumption yields a step-like earth model with constant velocities and densities within each layer. When the velocity and density contrasts across the boundary are assumed "small" compared to the absolute velocity and density values, the three reflection coefficient terms (R_p, R_s, and R_ρ) can be approximated by
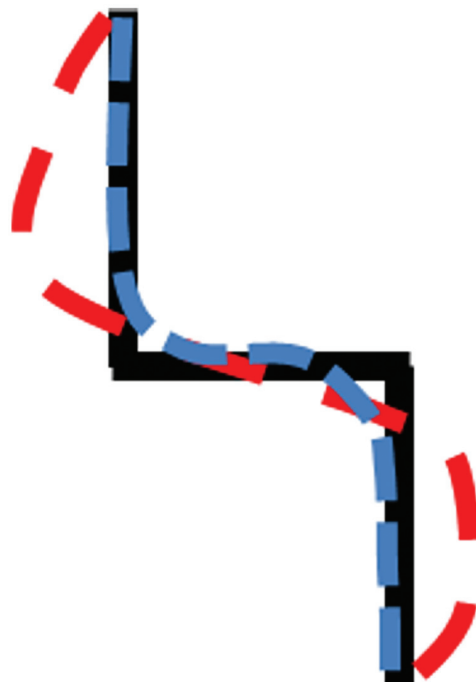

Figure 2. Sketch of the BPI idea for the absolute velocity and density. The solid black line represents an idealized boundary between two layers. The red dashed line represents a conventional inversion result exhibiting side lobes and unfocused layer boundary. The blue dashed line represents a schematically BPI with reduced side lobes and sharp layer contrasts (Theune et al., 2010).

the time derivative of the logarithm of the V_P, V_S, and ρ as follows:

$$R_p(t) = \frac{\Delta V_P(t)}{\bar{V}_P(t)} \asymp \frac{\partial}{\partial t} \ln V_P(t),$$

$$R_s(t) = \frac{\Delta V_S(t)}{\bar{V}_S(t)} \asymp \frac{\partial}{\partial t} \ln V_S(t),$$

$$R_\rho(t) = \frac{\Delta \rho(t)}{\bar{\rho}(t)} \asymp \frac{\partial}{\partial t} \ln \rho(t). \quad (14)$$

Integrating in time on both sides, the above equations can be transformed into equation 15 for estimation of absolute V_P, V_S, and ρ:

$$\ln V_P(t) = \int R_p(t)dt + \ln V_{P0}(t),$$

$$\ln V_S(t) = \int R_s(t)dt + \ln V_{S0}(t),$$

$$\ln \rho(t) = \int R_\rho(t)dt + \ln \rho_0(t). \quad (15)$$

The low-frequency models $V_{P0}(t)$, $V_{S0}(t)$, and $\rho_0(t)$ will have to be added to provide the missing low-frequency components, as shown in equation 15. Such low-frequency models ($V_{P0}(t)$, $V_{S0}(t)$, and $\rho_0(t)$) are usually generated from the low-pass filtered well-log data

with a high-cut frequency of 10–15 Hz. By using these formulas, the output velocities and density become the multiplication of the low-frequency model and exponential integration of the reflection coefficients:

$$V_P(t) = V_{P0}(t) \exp \int R_p(t)dt,$$

$$V_S(t) = V_{S0}(t) \exp \int R_s(t)dt,$$

$$\rho(t) = \rho_0(t) \exp \int R_\rho(t)dt. \quad (16)$$

SYNTHETIC EXAMPLES

The prestack BPI is first tested on a synthetic angle gather with incidence angles ranging from 0 to 45° (Figure 3b). This synthetic angle gather is generated from a piece of well-log data (Figure 3a) following the Aki and Richards approximation with a 40-Hz Ricker wavelet. Figure 3c shows the BPI reflectivities R_p, R_s, and R_ρ (in red), and the real R_p, R_s, and R_ρ from the well-log data (in black). Figure 3d shows the corresponding inverted V_P, V_S, and ρ (in red), with the real V_P, V_S, and ρ (in black). The initial models are also plotted in blue, which are the low-pass filtered well-log data (high-cut frequency of 10–15 Hz). It is found that the BPI results match well with the true reflectivities, velocity, and density. Comparing the inverted results with the initial models, for example, the event at
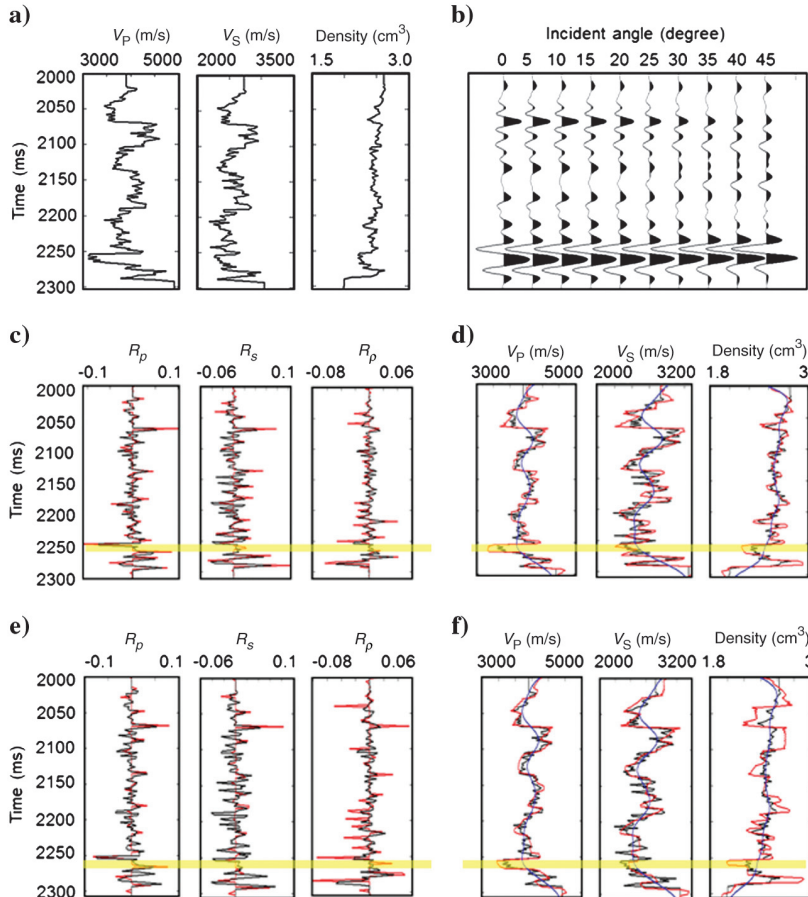
Figure 3. One-dimensional synthetic tests are applied on a piece of real well-log data; (a) shows real well-log data V_P, V_S, and ρ; (b) shows corresponding noise-free synthetic AVA gathers; (c) red lines show the inverted R_p, R_s, and R_ρ from noise-free data and the black lines are real R_p, R_s, and R_ρ calculated from well-log data; (d) shows red lines which are inverted V_P, V_S, and ρ from the noise free synthetic data, black lines are real V_P, V_S, and ρ, and blue lines are the low-frequency initial models; (e and f) show the inverted results with 10% noise added into the same synthetic AVA gathers. The yellow zone highlights an interval of inversion results, which is attributed mostly to the prestack seismic data.
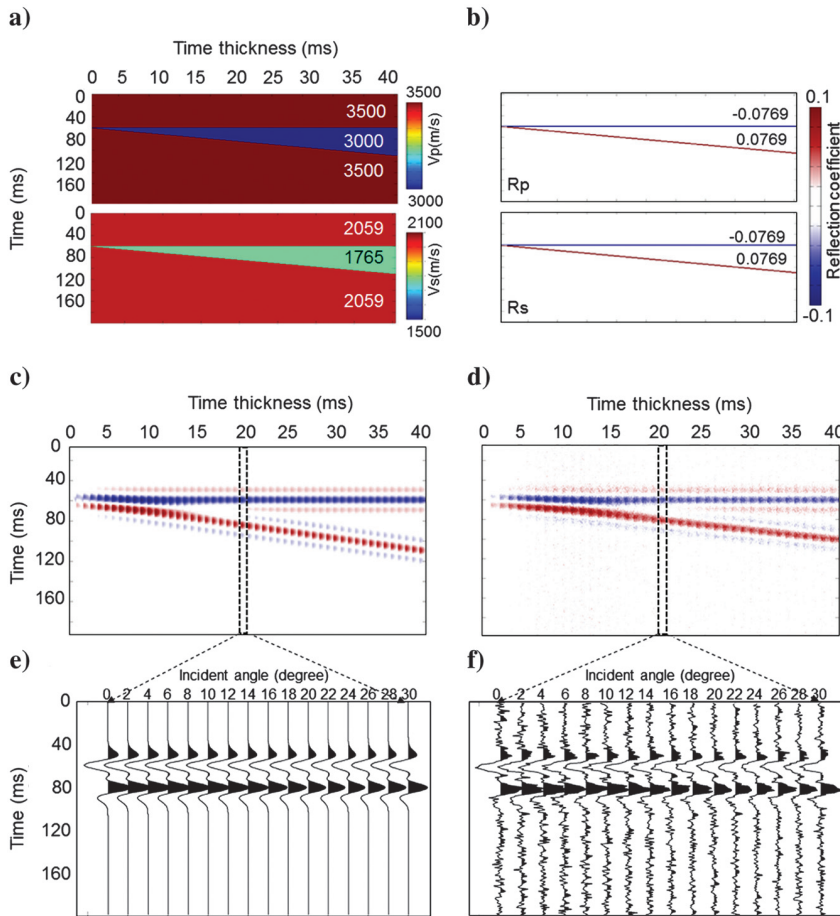
2275 ms (yellow zone), the initial model trends show an increase of V_P and V_S and a decrease of density, but inversion results, on the contrary, show the decrease of V_P and V_S, and the increase of density. This is mostly attributed to the contribution of the seismic data but not the initial model. Figure 3e and 3f shows the inversion results from the noise added data (10% random noise is added into the same synthetic angle gather in Figure 3b). As expected, the inversion results miss some events due to the noise effects. We also find from this test that the inverted R_ρ and density are more sensitive to the noise because the density term in the Aki and Richard equation has less weight than the other two terms.

Next, we show a 2D synthetic test on a single wedge model which is constructed (in Figure 4a) with a low-velocity wedge embedded between two high-velocity beds. The thickness of the wedge increases from 1 to 40 ms. The 2D synthetic data sets are generated for the incident angles ranging from 0° and 30°. Because the density information is mostly contained in the large incident angles, a constant density model is used here for simplicity. A 40-Hz Ricker wavelet is also used here. True P- and S-wave reflection coefficients (R_p and R_s) are shown in Figure 4b. Figure 4c and 4d shows the corresponding synthetic angle gathers with no noise and 20% random noise, respectively. The noise is generated by randomly drawing numbers from a Gaussian distribution, which is added to the noise-free synthetic seismogram. The examples of angle gathers with a bed thickness of 20 ms are shown in Figure 4e and 4f.

Figure 5a and 5b shows the inverted R_p and R_s from noise-free data. Figure 5g and 5j shows the

Figure 4. (a) Shows a single wedge velocity model of V_P and V_S; (b) shows the corresponding reflectivities of R_p and R_s from real model; (c and d) show the synthetic AVA gathers with no noise and 20% random noise added, respectively; (e and f) show the angle gathers with time thickness of 20 ms.
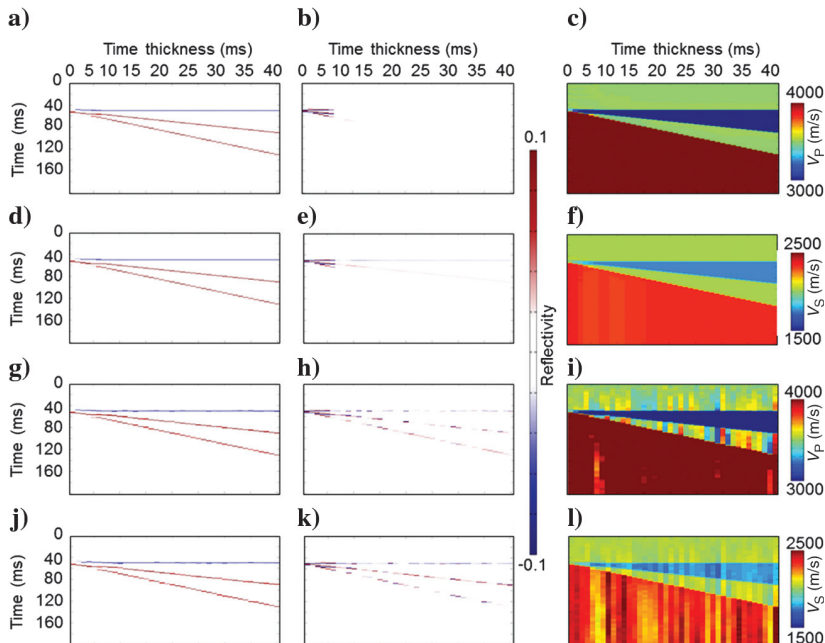
Figure 5. Two-dimensional synthetic tests are applied on the synthetic wedge model data in Figure 4. (a and d) show the inverted R_p and R_s with no noise; (g and j) show the inverted R_p and R_s with 20% random noise; (b, e, h, and k) show the residuals of inverted R_p and R_s with the true R_p and R_s in Figure 4; (b, c, f, i, and l) are corresponding V_P and V_S.
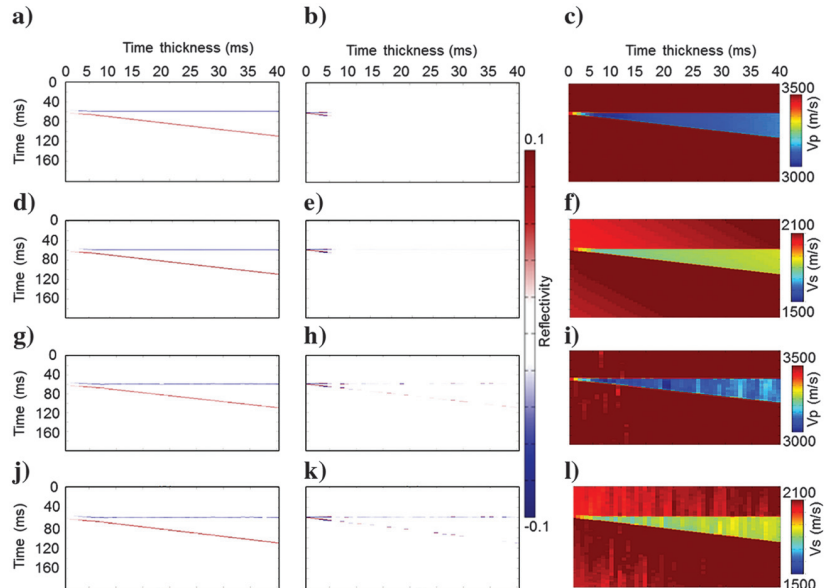
inverted R_p and R_s from the 20% noise-added angle gather data. Figure 5b, 5e, 5h, and 5k shows the residual of the inverted R_p and R_s with the true R_p and R_s. The noise-free inversion results show almost zero residual at the top and base of the wedge with the bed thickness larger than 4 ms (Figure 5b and 5e), whereas the noisy inversion results show nonzero residuals along the top and base of wedge of all thicknesses (Figure 5h and 5k). Based on these results, detectability for noise-free and noisy cases are approaching about 4 ms, whereas the noisy inversion results show nonzero residuals at the top and base of the whole wedge (Figure 5h and 5k). We note here that noise-free and noisy inversion results can show clear wedge shapes up to the thickness of 4 ms, but for noisy data, the inverted reflectivities are inaccurate at a few places. From these inverted reflectivities, interval velocities are derived using constant velocities of 3500 m/s for V_P and 2059 m/s for V_S as initial models. By comparing the inverted and the true velocities, we find that noise could reduce the accuracy of the inverted velocities, but the shape of the wedge is indeed recovered.

Another test on a double-wedge model is shown in Figures 6 and 7. The double wedge consists of four layers with one low-velocity wedge embedded and one high-velocity layer beneath (Figure 6a). The corresponding R_p and R_s are shown in Figure 6b. The generated angle gathers with no noise and 20% random noise added are shown in Figure 6c and 6d. The angle gathers with thickness of 20 ms are shown in Figure 6e and 6f. The noise-free inversion results
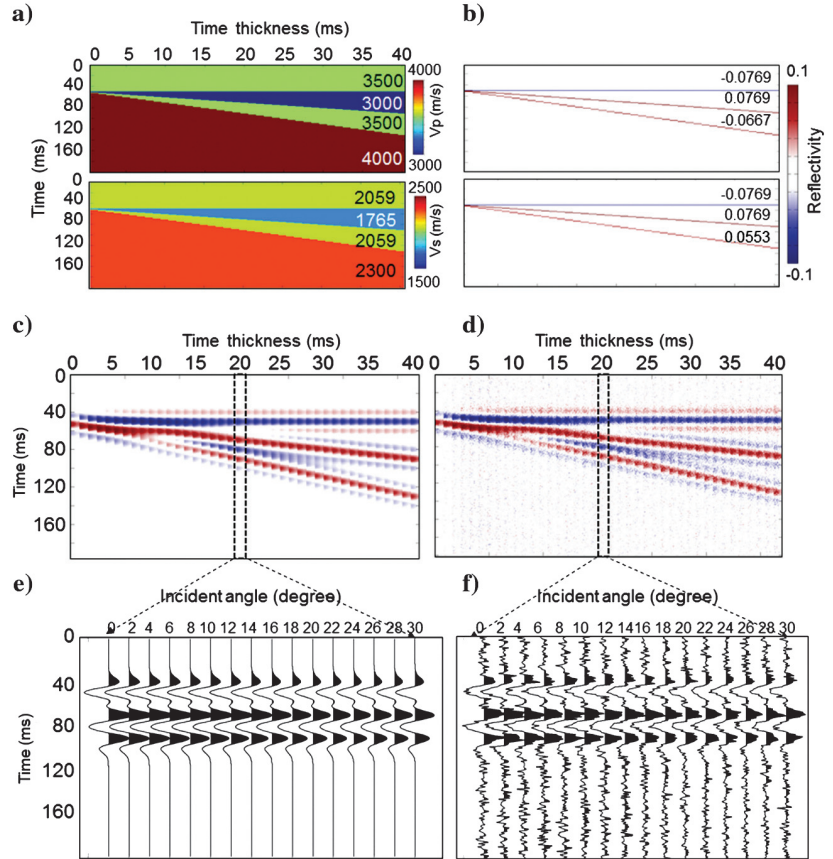
Figure 6. (a) Shows a double-wedge velocity model of V_P and V_S; (b) shows the corresponding R_p and R_s from real model; (c and d) show the corresponding synthetic AVA gathers with no noise and 20% random noise added; (e and f) show the angle gathers with time thickness of 20 ms correspondingly.

Figure 7. Two-dimensional synthetic tests are applied on the double wedge model in Figure 6; (a and d) show the inverted R_p and R_s with no noise; (g and j) show the inverted R_p and R_s with 20% random noise; (b, e, h, and k) show the residuals of inverted R_p and R_s, with the true R_p and R_s in Figure 6; (b, c, f, i, and l) are corresponding V_P and V_S.
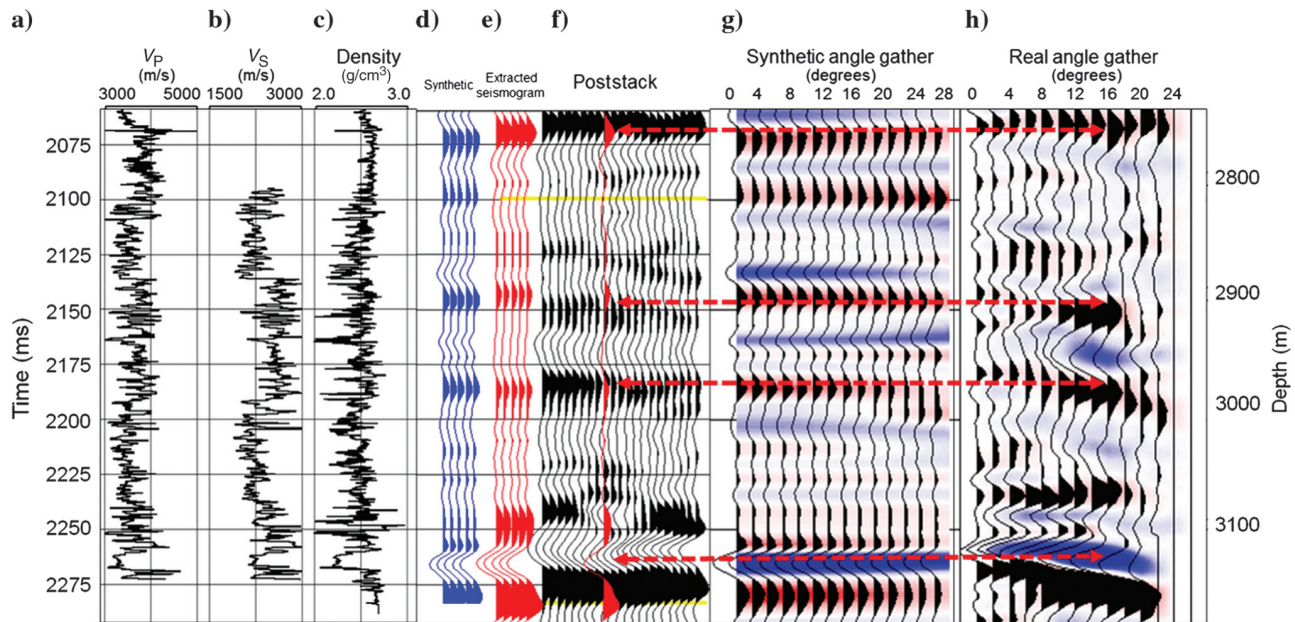
Figure 8. (a), (b), and (c) show well-log data of V_P, V_S, and density, respectively. (d) shows synthetic seismogram, (e) shows extracted seismogram, and (f) shows poststack seismic data, and prestack (g) and (h) show the synthetic and real angle gathers, respectively. Red dashed arrows highlight the correlated seismic events.
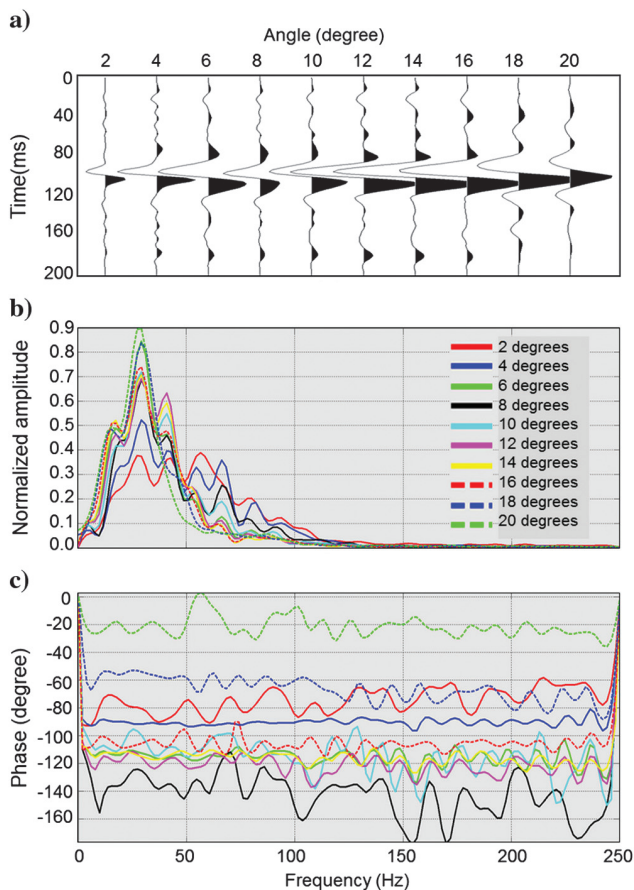

Figure 9. (a) Shows a set of angle dependent wavelets ranging from $2°$ to $20°$; (b and c) show their amplitude and phase spectra.

of R_p and R_s (Figure 7a and 7d) and their residual with true reflectivities (Figure 7b and 7e) show obvious differences at the bed boundaries with the thickness less than 6 ms. From these results and the previous single wedge test, we observe that the double wedges cause slightly poorer resolution than a single wedge. As expected, the noisy data inversion results (Figure 7g and 7j) and their residuals (Figure 7h and 7k) show obvious differences at all the boundaries. The constant velocities V_P of 3500 m/s and V_S of 2059 m/s are also used here as the initial models for inverted velocities. The noise-free inverted velocities (Figure 7c and 7f) reproduce the true model well, and the noisy data results show inaccurate velocities, but they can still retain similar profiles as the true models (Figure 7i and 7l). Based on the results from inversion of single- and double-wedge synthetic tests, we expect to obtain similar results for models with multiple thin layers. The inverted reflectivities predict accurate locations of the layer boundaries, but their amplitudes are dependent on the noise level of the data sets. Similar behavior is also observed in the inverted velocities, in that the inverted velocities can recover the correct shapes of the true models, but the derived velocity values are somewhat inaccurate because of the noise effect.

REAL DATA EXAMPLES

The prestack BPI is first tested on a real angle gather (sampling interval = 2 ms) at a well location with 2-ms sample rate from a clastic basin (Figure 8). Figure 8 shows the well-log data, including V_P, V_S, and density logs. The poststack seismic well tie is shown together with the corresponding synthetic and real angle gather. A fairly good crosscorrelation of 0.72 between synthetic (blue, convolution result of well-log reflectivity and wavelet) and extracted seismogram (red, a seismic trace at well-log location) demonstrates a reliable time-depth relationship. We have pretty good poststack seismic data tying with the well log well, but the synthetic

and prestack AVA gathers do not match very well. Although the real and synthetic AVA gathers do not match as well as the poststack seismic well tie, they still show correlated events between, as indicated by the red arrows. Nonstationarity observed in real angle gathers could be caused by many factors, including inaccurate migration velocity, NMO stretch, or other steps in seismic data processing. We do not have access to the raw data, and the main purpose of this work is to demonstrate the effectiveness of this methodology on prestack BPI. Given these, we decided to use the data as they are.

A set of angle-dependent wavelets are extracted by calibrating each angle datum with the well-log reflectivities. The extraction is done by inversion of the angle trace using the well-log reflectivity, as shown in Figure 9a. Their frequency and phase spectrum are shown in the right panel of Figure 9b and 9c. Wavelets, each of 200-ms length, are used to generate the wavelet kernel matrix for the corresponding angle data, as shown in equation 4. The angle-dependent wavelets are used in the calculation of the $W(t, \theta_i)$, which is the convolution of $C(t, \theta_i)$ and wavelet$_{\theta_i}$, where wavelet$_{\theta_i}$ is the angle-dependent wavelet instead of a constant wavelet. Because the maximum angle is about 20 degrees, which lacks the density information, we don't attempt to derive density.

Figure 10a and 10b shows the inverted V_P and V_S (in red) at the well-log location, aligning with the original well-log V_P and V_S velocities (in black). The initial model (in blue) used here is constructed by interpolating and extrapolating the well-log measured V_P and V_S following the picked horizons. The original well-log measurements, which were acquired at 0.5-ft-depth interval, are converted into time domain with 2-ms sample rate according to the previous time-depth curve. The spatial interpolation and extrapolation are done using the inverse distance weighting method (Li and Heap, 2008). A low-pass filter with high-cut frequency of 10–15 Hz is applied finally to build the low-frequency initial model. By comparing the inverted results with the real well-log data and the initial models, we notice that the BPI results clearly capture the events that are contained within the well-log data and do not show features from the initial model, as pointed out by red arrows. However, there are still some mismatches between them, as pointed out by black arrows.

After testing our BPI algorithm at one location, we applied it to a 2D seismic line shown in Figure 11. The 2D inverted reflectivities (R_p and R_s) are shown in Figure 11b and 11c, with well-log V_P and V_S inserted. Figure 11a shows the corresponding poststack seismic data. We note that the inverted R_p and R_s show structures similar to the poststack seismic and appear to have good fit with the well-log data at the layer boundaries. From these inverted reflectivities, we can derive the velocities, as shown in Figure 12. The well-log V_P and V_S, which are blocky filtered with 10 ms window, are inserted at the well-log location. The blocky filter replaces all the values within a 10-ms window with the mean value. Of course, any conventional band-pass filtered well-log curves, appearing smooth at all the boundaries, can be used to validate the conventional prestack inversion results. Black solid arrows point out regions of good fit between the BPI results and well-log velocities.

Figure 13 shows 1D comparisons between the well-log data (left), the conventional prestack inversion results (middle) and our BPI results (right) for V_P (top) and V_S (bottom). The original well-log data (black) and their blocky filtered data (red) are overlain in the left column of the Figure 13. Because the original well-log data contain very high-frequency components, they should not be

compared with the inversion results. The blocky filtered logging data can still keep the layer boundaries at the correct locations and can be meaningful for comparison with the well logs. The latter shows that the blocky results by BPI can highlight the layer
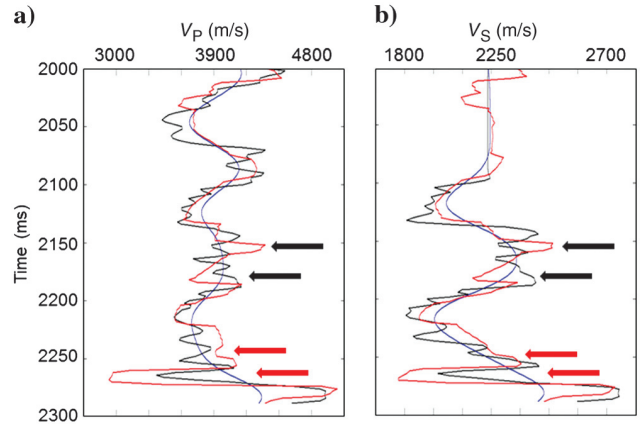

Figure 10. BPI-inverted V_P and V_S are in red lines; initial models for V_P and V_S are in blue lines; Well-log P- and S- wave velocity measurements are shown in black lines.
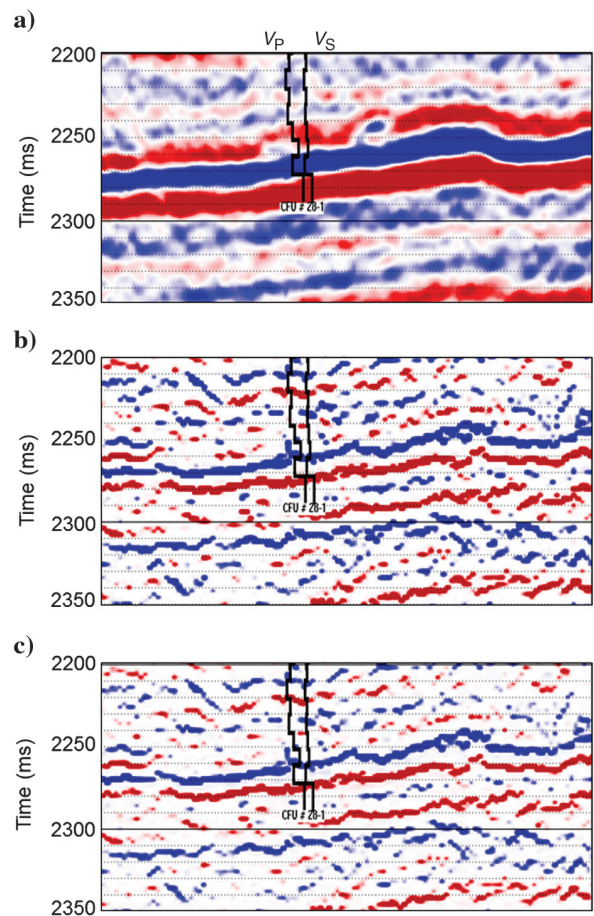

Figure 11. (a) Shows a 2D poststack cross section; (b and c) show the inverted R_p and R_s. Well-log V_P and V_S are inserted.

boundaries more clearly, for example in regions marked with red ellipses. However, some mismatches indicated by red arrows exist between the inversion results and the well log data. Also, as expected, blocky and smooth inversion results follow the same trend (black arrows) because they are derived from the same prestack data. The blocky results from BPI with improved resolution could

Figure 12. Inverted velocities of V_P (a) and V_S (b) with the well-log V_P and V_S inserted.

Figure 13. The V_P and V_S from (a) well-log data, red lines are blocky filtered; (b) conventional inversion; (c) basis pursuit inversion.

be considered as additional subsurface information available for elastic properties interpretation.

DISCUSSIONS

Prestack seismic inversion uses the amplitude variation with offset characteristics to capture the lithological change. Thus, amplitude preservation is important for the validity of the inversion results. However, seismic data processing, which is a multistep workflow, could distort the amplitude at any step of the procedure. A careful processing would be necessary for a successful prestack inversion. We assume that wave-mode conversions, interbed multiples, and all kinematic effects of anisotropy are handled beforehand during data processing. The data should be prestack migrated, such that dip-related effects and moveouts are removed. After prestack migration, we assume that each single bin gather can be regarded as the response of a local 1D earth model.

The L_1-norm objective function (equation 13) is the key to derive spiky reflectivities and blocky velocities. The trade-off factor λ plays an important role in controlling the characteristic of the solution. A large λ value can increase the sparsity of the solution, and a small λ can increase the smoothness. A set of synthetic tests of the effect of λ has been reported in Zhang and Castagna (2011). For real data applications, we choose an appropriate value after calibrating with well-log data.

For small values of incident angle θ, the coefficient of $\Delta\rho/\bar{\rho}$ is often nearly zero. The fact that this coefficient is generally small means that we can have large variations in our estimates of $\Delta\rho/\bar{\rho}$ without having a large effect on the values of $R(\theta)$. This means that it is often difficult to invert for values of fractional density contrast by using AVO values. This is also the reason why we did not derive density values in this paper.

Conventional inversion and BPI results, as shown in Figure 13, are smooth or blocky. The difference lies in the second term of equation 13: the conventional method uses L_2 and BPI uses L_1. Both methods are aimed for quantitative interpretation and reservoir characterization, which needs highly integrative information. The advantage of our BPI method is the delineation of the layers boundaries, which can be especially helpful for target-oriented interpretation.

CONCLUSIONS

Basis pursuit inversion was formulated with incorporation of a wedge dictionary for poststack seismic data. Here, we extend BPI to the prestack angle gather domain. The major contribution of this work is the extended formulation of basis pursuit inversion and incorporation of the wedge dictionary on prestack seismic data. The BPI method follows an L_1-norm optimization framework and incorporates a wedge dictionary. Thus, the inversion results become the summation of the sparse layers instead of sparse spikes. Unlike other existing AVA inversion methods, which produce smooth results, our method can generate spiky reflectivities (R_p, R_s) and blocky velocities (V_P and V_S). The synthetic tests demonstrate that the inverted results are in good agreement with the true models and that they resolve single and double thin beds very well. The real data applications also show good fit with well-log measurements and improved layers delineation, which provide additional constraints in subsequent interpretation.
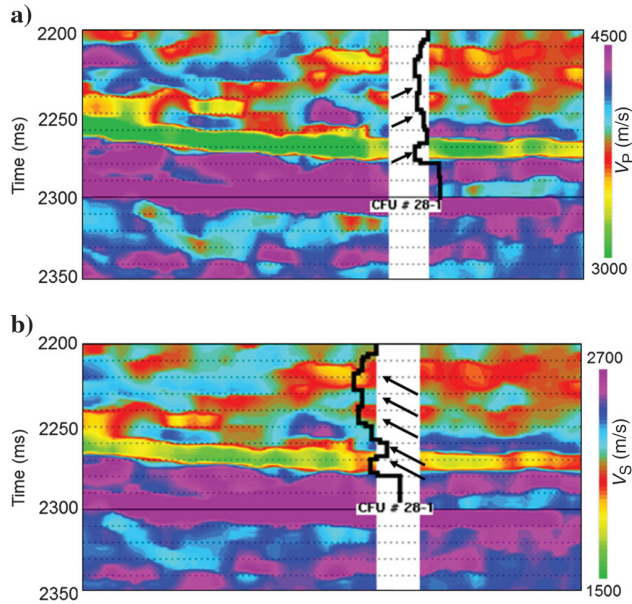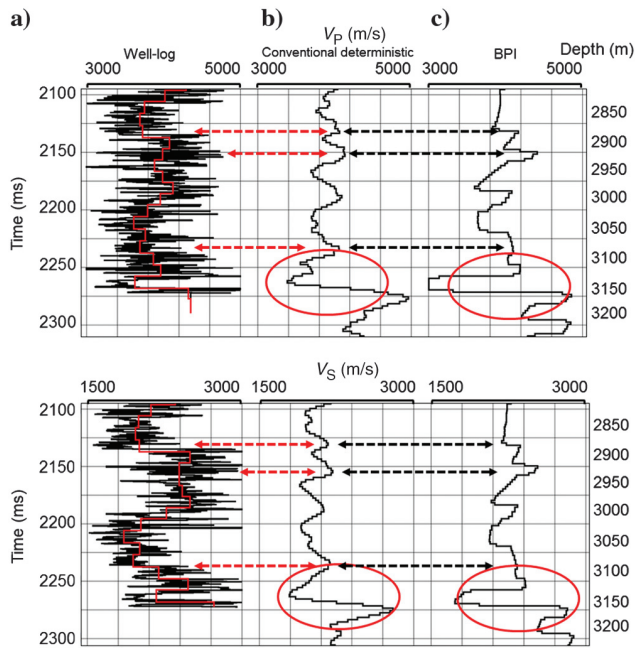
ACKNOWLEDGMENTS

REFERENCES

Aki, K., and P. G. Richards, 1980, Quantitative seismology: Theory and methods: W.H. Freeman.

Astfalk, G., I. Lustig, R. Marsten, and D. Shanno, 1992, The interior-point method for linear programming: IEEE Software, **9**, 61–68, doi: 10.1109/52.143109.

Bork, J., and L. Wood, 2001, Seismic interpretation of sonic logs: 71st Annual International Meeting, SEG, Expanded Abstracts, 510–513.

Bortfeld, R., 1961, Approximations to the reflection and transmission coefficients of plane longitudinal and transverse waves: Geophysical Prospecting, **9**, 485–502, doi: 10.1111/gpr.1961.9.issue-4.

Brossier, R., S. Operto, and J. Virieux, 2010, Which data residual norm for robust elastic frequency-domain full waveform inversion?: Geophysics, **75**, no. 3, R37–R46, doi: 10.1190/1.3379323.

Bube, K. P., and R. T. Langan, 1997, Hybrid l_1/l_2 minimization with applications to tomography: Geophysics, **62**, 1183–1195, doi: 10.1190/1.1444219.

Buland, A., and H. Omre, 2003, Bayesian linearized AVO inversion: Geophysics, **68**, 185–198, doi: 10.1190/1.1543206.

Castagna, J. P., M. L. Batzle, and R. L. Eastwood, 1985, Relationships between compressional-wave and shear-wave velocities in clastic silicate rocks: Geophysics, **50**, 571–581, doi: 10.1190/1.1441933.

Chen, S. S., D. L. Donoho, and M. A. Saunders, 2001, Atomic decomposition by basis pursuit: SIAM Review, 129–159, doi: 10.1137/S003614450037906X.

Gardner, G. H. F., L. W. Gardner, and A. R. Gregory, 1985, Formation velocity and density — The diagnostic basics for stratigraphic traps: Geophysics, **50**, 2085–2095, doi: 10.1190/1.1440465.

Gill, P. E., W. Murray, D. B. Poncele, and M. A. Saunders, 1991, Solving reduced KKT systems in barrier methods for linear and quadratic programming: Technical report, Stanford University.

Guitton, A., and W. Symes, 2003, Robust inversion of seismic data using the Huber norm: Geophysics, **68**, 1310–1319, doi: 10.1190/1.1598124.

Li, J., and A. Heap, 2008, A review of spatial interpolation methods for environmental scientists: Geoscience Australia.

Liu, Z., and N. Bleistein, 1995, Migration velocity analysis: Theory and an iterative algorithm: Geophysics, **60**, 142–153, doi: 10.1190/1.1443741.

Mallick, S., 2001, AVO and elastic impedance: The Leading Edge, **20**, 1094–1104, doi: 10.1190/1.1487239.

Nguyen, T., and J. Castagna, 2010, High resolution seismic reflectivity inversion: Journal of Seismic Exploration, 303–320.

Richards, P. G., and C. W. Frasier, 1976, Scattering of elastic waves from depth-dependent inhomogeneities: Geophysics, **41**, 441–458, doi: 10.1190/1.1440625.

Roos, T. T. V., and J.-P. Cornelis, 2006, Interior-point methods for linear optimization: Springer.

Scales, J., and L. Tenorio, 2001, Prior information and uncertainty in inverse problems: Geophysics, **66**, 389–397, doi: 10.1190/1.1444930.

Sen, M. K., and I. G. Roy, 2003, Computation of differential seismograms and iteration adaptive regularization in prestack waveform inversion: Geophysics, **68**, 2026–2039, doi: 10.1190/1.1635056.

Sen, M. K., and P. L. Stoffa, 1996, Bayesian inference, Gibbs' sampler and uncertainty estimation in geophysical inversion: Geophysical Prospecting, **44**, 313–350, doi: 10.1111/gpr.1996.44.issue-2.

Srivastava, R. P., and M. K. Sen, 2009, Fractal-based stochastic inversion of poststack seismic data using very fast simulated annealing: Journal of Geophysics and Engineering, **6**, 412–425, doi: 10.1088/1742-2132/6/4/009.

Srivastava, R. P., and M. K. Sen, 2010, Stochastic inversion of prestack seismic data using fractal-based initial models: Geophysics, **75**, no. 3, R47–R59, doi: 10.1190/1.3379322.

Theune, U., I. O. Jensas, and J. Eidsvik, 2010, Analysis of prior models for a blocky inversion of seismic AVA data: Geophysics, **75**, no. 3, C25–C35, doi: 10.1190/1.3427538.

Tikhonov, A., 1963, Solution of incorrectly formulated problems and the regularization method: Soviet Math Dokl 4 English translation of Dokl Akad Nauk SSSR, **151**, 1035–1038.

Varela, O. J., C. Torres-Verdn, and M. K. Sen, 2006, Enforcing smoothness and assessing uncertainty in non-linear one-dimensional prestack seismic inversion: Geophysical Prospecting, **54**, 239–259, doi: 10.1111/gpr.2006.54.issue-3.

Wright, M. H., 1992, Interior methods for constrained optimization: Acta Numerica, **1**, 341–407, doi: 10.1017/S0962492900002300.

Wright, S. J., 1997, Primal-dual interior-point methods: SIAM.

Zhang, R., 2010, Basis pursuit seismic inversion: Ph.D. thesis, University of Houston.

Zhang, R., and J. Castagna, 2011, Seismic sparse-layer reflectivity inversion using basis pursuit decomposition: Geophysics, **76**, no. 6, R147–R158, doi: 10.1190/geo2011-0103.1.

Zhang, R., M. K. Sen, S. Phan, and S. Srinivasan, 2012, Stochastic and deterministic seismic inversion methods for thin-bed resolution: Journal of Geophysics and Engineering, **9**, 611–618, doi: 10.1088/1742-2132/9/5/611.

Zoeppritz, K., 1919, Ber reflexion und durchgang seismischer wellen durch unstetigkeitsflchen: Nachrichten von der Kniglichen Gesellschaft der Wissenschaften zu Gttingen, **VII. VIIb**, 66–84.